Diffractive and Refractive Optical Microstructures: Theory, Design, and Applications

Andreas Schilling

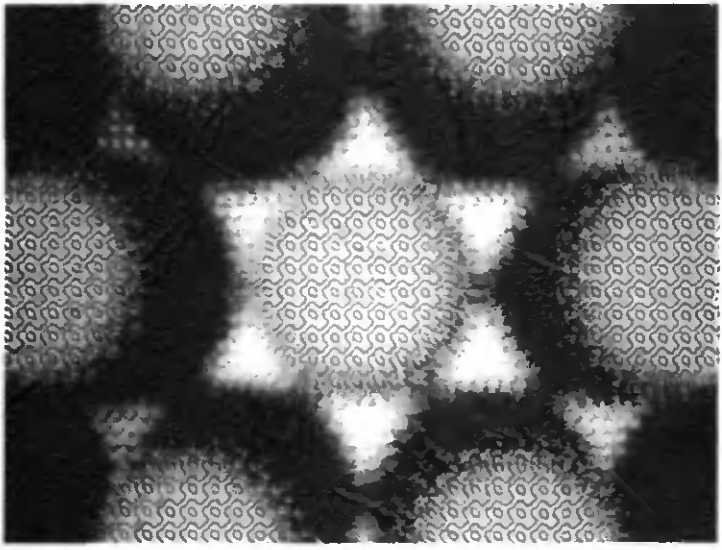

UFO Atelier für Gestaltung & Verlag

Université de Neuchâtel
Institut de Microtechnique

Diffractive and Refractive Optical Microstructures: Theory, Design, and Applications

Thèse

Présentée à la Faculté des sciences
pour obtenir le grade de docteur ès sciences
par

Andreas Schilling

Neuchâtel, septembre 2000

UFO Dissertation Band 392

Die Deutsche Bibliothek – CIP-Einheitsaufnahme

Ein Titelsatz für diese Publikation ist bei Der Deutschen Bibliothek erhältlich.

Dissertation der Universität Neuchâtel
Datum der mündlichen Prüfung: 19.09.2000
Referenten: Prof. Dr. R. Dändliker
Prof. Dr. H.P. Herzig
Prof. Dr. T. Tschudi
Dr. W. R. Tompkin

UFO Atelier für Gestaltung & Verlag GbR
Allensbach
Internet http://www.ufo-verlag.de
Maus Druck & Medien GmbH, Konstanz
Erste Auflage 2000

ISBN 3-930803-92-5

IMPRIMATUR POUR LA THESE

Diffractive and Refractive Optical Microstructures: Theory, Design and Applications

de M. Andreas Schilling

UNIVERSITE DE NEUCHATEL

FACULTE DES SCIENCES

La Faculté des sciences de l'Université de Neuchâtel sur le rapport des membres du jury,

MM. R. Dändliker (directeur de thèse), H.-P. Herzig, T. Tschudi (Darmstadt) et W.R. Tompkin (Zug)

autorise l'impression de la présente thèse.

Neuchâtel, le 21 septembre 2000

Le doyen:

J.-P. Derendinger

Abstract

Refractive and diffractive optical microstructures have been of increasing interest in recent years in the academic as well as in the industrial sector. This was mainly driven by potential applications, where diffractive and refractive optical microstructures are key elements. Some applications have already developed into commercial products. This thesis provides a summary of the author's work in the field of micro-optics. Theoretical and experimental results related to refractive and diffractive optical microstructures are presented.

We address the fundamental problem of how to translate an ideal designed phase function of a diffractive optical element (DOE) into a surface relief profile of a "real-world" element with given fabrication constraints. First, we treat the case, when for the fabrication of a DOE, the continuous profile is approximated by a multilevel profile. For this we analyzed the scalar-based method Direct Sampling (DS) for phase function encoding with exact electromagnetic diffraction theory. Second, we show how the influence of the finite width of the writing beam can be significantly reduced when continuous-relief DOEs are fabricated by direct laser writing.

We present results which are related to deep optical micro-structures. A method is introduced to calculate the 3-D surface profiles of refractive optical microstructures fabricated by the resist reflow technique. The border geometry of the structures can be arbitrary, and surface tension and gravity are fully taken into account. Micro-optical elements are presented which combine the fan-out and focusing function, resulting in compact monolithic elements. These miniaturized, focusing fan-out elements are useful for applications in parallel optical processing,[A.G. Kirk, D.F. Brosseau, F.K. Lacroix, E. Bernier, M.H. Ayliffe, B. Robertson, F.A.P. Tooley, D.V. Plant; Proc. SPIE **3490**, 48-51 (1999)] or miniaturized parallel detection systems. Theoretical and experimental results for periodic color separating gratings having small grating periods are shown. We introduce deep diffractive structures which can overcome the basic drawback of conventional DOEs that high diffraction efficiencies are only achieved for the design wavelength. The

DOEs show a nearly wavelength independent, high diffraction efficiency over a large spectral bandwidth in the visible region.

We designed, fabricated and characterized a new incoherent diode-laser collimator for application in rangefinder systems with extended measurement range. Additionally, three different technologies are compared for the fabrication of the diffractive and refractive elements which were employed. Finally, theoretical and experimental results are presented for diffractive structures with continuously varying profile form for visual security applications.

Contents

Chapter 1

Introduction

Refractive and diffractive optical microstructures have gained increasing interest in recent years. The research effort is mainly driven by real and potential commercial applications for such microstructures, like UV–beamshaping, Microlens Projection Lithography (MPL), and miniaturized analytical systems (μTAS).

This thesis provides a summary of the author's work in the field of micro-optics. The thesis is divided into six chapters. Chapter 1 introduces the work and gives an overview of the structure of the thesis. Chapter 2 presents a compact overview of the fabrication technologies which were used for the fabrication of refractive and diffractive optical microstructures. The theoretical background which is necessary for the understanding of the following chapters is provided in Chapter 3.

We treat in Chapter 4 the problem of translating a designed phase function of a diffractive optical element (DOE) into a surface relief profile of a "real–world" element with given fabrication constraints. In Section 4.1 the case is treated where the continuous profile of the DOE is approximated by a staircase–like multilevel profile. We applied exact electromagnetic theory to the scalar Direct Sampling (DS) method and found an extended application range which clearly exceeds the theoretically justified scalar regime. In Section 4.2 we address the case when the DOE is fabricated by direct laser beam writing and the finite width of the writing spot has to be taken into account.

The results which are related to deep optical micro-structures are contained in the four sections of Chapter 5. In Section 5.1 a new method is introduced to calculate the surface profiles of refractive optical microstructures fabricated by the resist reflow technique. The method takes fully into account surface tension and gravity. It is especially suited for resist reflow microstructures having arbitrary border geometries. We develop the model, compare

experimental and theoretical surface profiles, and show how this method can be applied to the design of "smart mask" microstructures. In Section 5.2 we present a new type of hybrid micro-optical elements which combine fan-out and focusing function, resulting in compact monolithic elements with miniaturized dimensions. These miniaturized, focusing fan-out elements are useful for applications in parallel optical processing, or miniaturized parallel detection systems. In Section 5.3 theoretical and experimental results for periodic, color separating gratings are presented. In Section 5.4 we propose and analyze an improved type of gratings with nearly wavelength-independent, high diffraction efficiency and show the advantages of the improved approach.

Two specific applications, where optical microstructures are employed, are presented in Chapter 6. In Section 6.1 a diode-laser collimator is presented which contains as key element a combined micro-optical element that achieves an extended measurement range for rangefinder applications. The micro-optical elements can be either refractive or diffractive. In Section 6.2 we show theoretical and experimental results for a new type of combination gratings with specially designed optical properties that can be exploited in visual security applications.

The author's publications

A large part of the work described in this thesis has already been published in peer-reviewed journals and has been presented at various international conferences.

Publications in peer-reviewed journals:

1 A. Schilling, P. Blattner, and H.P. Herzig; Direct Sampling for Diffractive Microlens Encoding from a Rigorous Point of View; Pure Appl. Opt. **7**, 565–574 (1998).

2 A. Schilling, Ph. Nussbaum, Ch. Ossmann, S. Traut, M. Rossi, H. Schift, H.P. Herzig; Miniaturized, Focusing Fan-out Elements: Design, Fabrication, and Characterization; J. Opt. A, Pure Appl. Opt. **1**, 244–248 (1999).

3 R. Staub, W.R. Tompkin, A. Schilling; Gratings of constantly varying depth for visual security devices; Opt. Eng. **38**, 89–98 (1999).

4 W.R. Tompkin, R. Staub, A. Schilling, H.P. Herzig; Diffraction from metallic gratings with locally varying profile forms; Opt. Lett. **24**, 71–73 (1999).

5 A. Schilling, R. Merz, Ch. Ossmann, H.P. Herzig; Surface profiles of reflow microlenses under the influence of surface tension and gravity; Opt. Eng. **39** 2171–2176 (2000).

6 A. Schilling, H.P. Herzig; Phase function encoding of diffractive structures; Appl. Opt. **39**, 5273-5279 (2000).

7 A. Schilling, H.P. Herzig, L. Stauffer, U. Vokinger, M. Rossi; Efficient beamshaping of linear, high-power diode-lasers using micro-optics; submitted for publication to Appl. Opt.

Contributions presented at international conferences:

1 A. Schilling, P. Blattner, and H.P. Herzig; Kodierung von diffraktiven Mikrolinsen: Eine Analyse mit rigoroser Beugungstheorie; DGaO Jahrestagung 1998, June 2–6, 1998, Hannover, Germany.

2 A. Schilling, Ph. Nussbaum, I. Philipoussis, Ch. Ossmann, S. Traut, M. Rossi, H. Schift, H.P. Herzig; Miniaturisierte, fokussierende fan-out Elemente: Design, Fabrikation und Charakterisation; DGaO Jahrestagung 1998, June 2–6, 1998, Hannover, Germany.

3 A. Schilling, Ph. Nussbaum, Ch. Ossmann, S. Traut, M. Rossi, H. Schift, H.P. Herzig; Miniaturized, Focusing Fan-out Elements: Design, Fabrication, and Characterization; Proc. SPIE **3490**, 386-388 (1998); Optics in Computing 98, June 16–20, 1998, Brugge, Belgium.

4 H.P. Herzig, Ph. Nussbaum, A. Schilling, S. Traut, I. Philipoussis, Ch. Ossmann, R. Völkel, M. Rossi, H. Schift; Different concepts for the fabrication of hybrid (refractive/diffractive) elements; Technical Digest Series **10**, 279–281 (1998), OSA Topical Meeting on Diffractive Optics and Micro-Optics 1998, June 8–11, 1998, Hawaii, USA.

5 K.J. Weible, A. Schilling, H.P. Herzig, D. Lobb; Achromitization of the diffraction efficiency of diffractive optical elements; Proc. SPIE **3749**, 378–379 (1999), 18th Congress of the ICO, 2–6 August, 1999, San Francisco, USA.

6 A. Schilling, W. Tompkin, R. Staub, H.P. Herzig; Metallische Beugungsgitter mit räumlich variierender Profilform und -tiefe für Anwendungen in der

Dokumentensicherheit; DGaO Jahrestagung 1999, May 25-29, 1999, Berlin, Germany.

7 A. Schilling, R. Merz, Ch. Ossmann, and H.P. Herzig; Surface profiles of reflow microlenses under the influence of surface tension and gravity; Tech. Digest of the 7th Microoptics Conference (MOC99), 132-135 (1999), July 14-16, 1999, Tokyo, Japan.

8 A. Schilling, K.J. Weible, H.P. Herzig; Diffractive structures with high, wavelength independent efficiency; EOS Topical Meetings Digest Series **22**, 16-17 (1999), Diffractive Optics 99, August 23-25, 1999, Jena, Germany.

9 W. Tompkin, R. Staub, A. Schilling, H.P. Herzig; Metallic gratings with locally varying profile; EOS Topical Meetings Digest Series **22**, 72-73 (1999), Diffractive Optics 99, August 23-25, 1999, Jena, Germany.

10 W. Tompkin, R. Staub, Ch. Weiteneder, A. Schilling, H.P. Herzig; High-frequency gratings with locally varying profile depth for visual security applications; EOS Topical Meetings Digest Series **25**, 72-73 (2000), Engelberg 2000 - Nanoscale Optics, 25th EOSTM, April 16-19, 2000, Engelberg, Switzerland.

11 A. Schilling, M. Lo, M. Rossi, Ph. Nussbaum, I. Philipoussis, H.P. Herzig; Periodische und nicht-periodische Farb-Fanout Elemente: Ein Vergleich von Konzepten und Technologien; DGaO Jahrestagung 2000, June 13-17, 2000, Jena, Germany.

12 A. Schilling, R. Merz, Ch. Ossmann, H.P. Herzig; Optimale Oberflächenprofile von Schmelzlack-Mikrolinsen unter dem Einfluss von Oberflächenspannung und Gravitation; DGaO Jahrestagung 2000, June 13-17, 2000, Jena, Germany.

13 A. Schilling, Ph. Nussbaum, I. Philipoussis, H.P. Herzig, L. Stauffer, M. Rossi, E.-B. Kley; Micro-optical elements with arbitrary surfaces; Technical Digest of Diffractive Optics and Micro-Optics 2000, 234-236 (2000), June 18-22, 2000, Quebec, Canada.

14 A. Schilling, Ph. Nussbaum, I. Philipoussis, H.P. Herzig, L. Stauffer, M. Rossi, E.-B. Kley; Fabrication technologies for micro-optical elements with arbitrary surfaces; Proc. SPIE **4179** 65-72 (2000), Micromachining and Microfabrication 2000, September 18-21, 2000, Santa Clara, USA.

The author contributed to the following patent applications:

1 European patent application P99003; "Binary Blazed Gratings for Contrast Reversal"; W. Tompkin (OVD), R. Staub (OVD) and A. Schilling (IMT). In collaboration with OVD Kinegram Corporation, Zug, Switzerland; patent pending.

2 European patent application 00108836.8; "Optischer Entfernungsmesser"; B. Gächter (Leica), A. Schilling (IMT), L. Stauffer (Leica), U. Vokinger (Leica). In collaboration with Leica Geosystems AG, Heerbrugg, Switzerland; patent pending.

Chapter 2

Fabrication of optical microstructures

This chapter gives a compact overview of the technologies which were used for the fabrication of the refractive and diffractive optical microstructures presented in this thesis. Hereby we distinguish origination and transfer techniques. We describe four origination technologies, photolithography, direct laser writing, holographic recording, and the melting resist technology. Reactive ion etching (RIE), described in the last Section of this Chapter, is a method to transfer a given microstructure, in photoresist for example, into another material with better optical properties. During the transfer, the profile shape can be modified.[66] We used RIE to transfer photoresist structures into fused silica. Photolithography is the most important fabrication technology, since it was used for the binary mask photolithography, the gray-tone technology, and for the fabrication of microlenses by the melting resist technology.

2.1 Photolithographic techniques

Photolithography is a well established technology to structure photoresist. It has its origin in the semiconductor manufacturing world for the fabrication of Very-Large-Scale-Integration (VLSI) circuits where computer-aided design (CAD) tools are used to generate mask data.[97, 89] Micro-optics and diffractive optics have adapted this mature technology for the fabrication of optical microstructures. This was suggested by the fact that the typical dimensions of the smallest features are on the same order of magnitude for both, state of the art semiconductor structures and optical microstructures. The basic principle of all lithographic techniques is to expose a radiation-

sensitive polymeric material like photoresist, which has been deposited on a substrate, with UV light through a binary or a graytone mask.[88] The radiation causes the film composition to alter through either a photochemical reaction or crosslinking of the polymer chains. The excess material is then removed by dissolution in a developer solution. There are positive and negative photoresists, depending on whether the exposed or the unexposed resist is removed by the developer solution. After the developing process the surface relief profile in photoresist is obtained. The mask, through which the photoresist is exposed, can have either a binary or a continuously varying transmittance function. The use of a chromium mask with binary transmittance for UV light results in binary resist surface profiles. Using a graytone mask with a continuously varying transmittance function results in a continuos surface relief profile. We will describe these two different cases briefly in the following Subsections 2.1.1 and 2.1.2.

2.1.1 Binary mask photolithography

For the fabrication of diffractive optical elements (DOE) the multilevel approach [88] is probably the most widespread, since it is a mature and reliable technology. In this section we give a short description of binary photolithography. In combination with the transfer technology RIE (see Section 2.5) multilevel profiles can be fabricated. The number of discrete phase levels N is given by 2^p, where p is the number of binary masks. The approximation of the desired surface profile by the multilevel profile is better if more phase levels are available. Since the first-order scalar diffraction efficiency depends on the number of phase levels as [15]

$$\eta_1(N) = |sinc(1/N)|^2, \tag{2.1}$$

at least 8 phase levels or three lithographic steps are necessary for highly efficient elements (> 90%). In Section 4.1 a detailed analysis of the encoding problem is given, i.e. the approximation of a continuous surface profile by a multilevel profile. The basic principle of binary mask photolithography combined with subsequent RIE steps is shown in Fig. 2.1. The substrate, which is coated with a thin photoresist layer, is exposed through a binary chromium mask with a UV lamp. The chromium mask is normally fabricated by laser beam or electron beam writing, depending on the required resolution of the pattern. After the development step, a resist pattern remains, which is then transferred into the substrate by the subsequent etch step. The second photolithographic step, aligned with respect to the first through alignment marks, creates a refined resist pattern which is then again transferred into

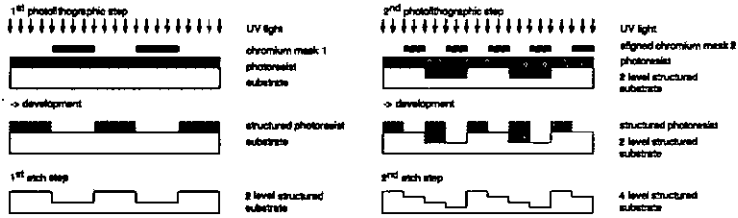

Figure 2.1: Fabrication of multilevel profiles by binary mask photolithography and reactive ion etching (RIE).

the substrate resulting in a 4-level surface profile. For 8- or 16-level surface profiles correspondingly more aligned lithography and etch steps are necessary. The standard way is to use the mask with the smallest features first and the mask with the largest features last.

2.1.2 Graytone technology

In the standard case the phase function of a refractive or diffractive micro-optical element is continuous. Therefore the fabrication method described in Section 2.1 has the drawback that the fabricated structure is only a multilevel approximation of the desired continuous profile. Graytone technology can overcome this basic drawback by using a mask which has a continuous variation of transmission (graylevels). This is achieved with high energy beam sensitive (HEBS) glass,[104, 48] which is fabricated using a silver ion exchange process.[16, 33] When exposed to a high energy electron beam, reduction of the silver ions occurs in the HEBS-glass mask, and the optical density of the material changes. The optical density increases with the electron dosage. Typical values are 0–2.6 for a wavelength of $\lambda = 365\,nm$. A major difficulty compared to binary mask photolithography is the accurate control of the nonlinear photoresist response. For the graytone technology one needs to establish a calibration curve, resist height as a function of graylevels or electron dosage, using a set of calibration structures for the specific lithographic process. This calibration curve is afterwards used to encode the surface profile of the designed structure into electron dose per pixel for the e-beam writing procedure. Once the HEBS glass mask is written by e-beam technology, the continuous surface relief profiles are fabricated by a single photolithographic step, which classifies the method as a parallel fabrication technology. The

fabrication process of continuous surface profiles with a one-step lithography is shown schematically in Fig. 2.2.

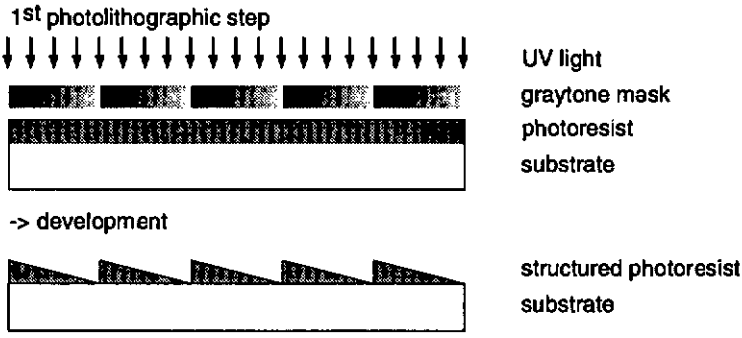

Figure 2.2: One-step lithography with a graylevel HEBS glass mask to obtain continuous surface profiles.

2.2 Direct laser beam writing

Another approach to obtain continuous surface relief profiles for diffractive or refractive optical elements in photoresist is laser direct writing. We used the laser writer III at the CSEM in Zurich, which utilizes a focused He-Cd laser beam ($\lambda = 442nm$) to expose a photoresist coated substrate in a raster scan. A detailed decription of the laser writer can be found in the dissertation of Hessler.[39] After exposure, the photoresist is developed and the surface relief structure is obtained. A schematic setup of the laser writer III is shown in Fig. 2.3. The direct laser writing technique is a very flexible and fast method to obtain prototypes without the need to generate masks like in photolithographic methods. A drawback is the long writing time for large and high resolution structures. This disadvantage can be partially compensated by combining the direct writing technique with an appropriate replication technology.[29, 30] From the photoresist original a master is fabricated through galvanic electroforming. Using this master, copies of the original structure can be made.

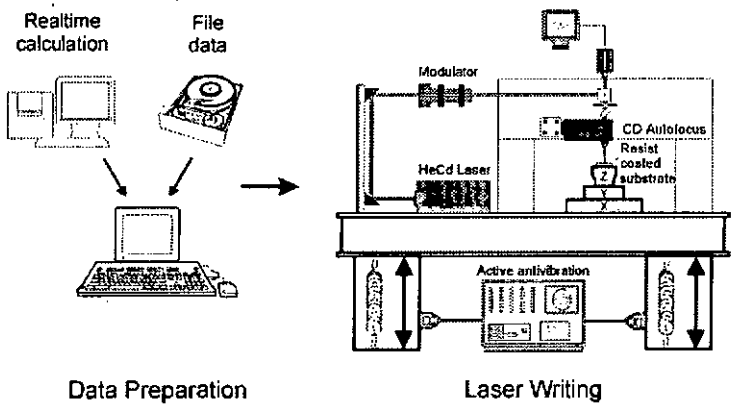

Figure 2.3: Setup of the laser writer III at the CSEM in Zurich, Switzerland (courtesy of M. Rossi, CSEM in Zurich).

2.3 Holographic recording technique

Holographic recording is a well known technique for the fabrication of grating structures and a large variety of experimental setups and fabrication procedures have been developed.[84, 3, 94, 19] Two coherent beams of a laser are generated using a beamsplitter and brought to interference on a photosensitive material like photoresist. After a development step, this interference pattern results in a surface relief profile, which corresponds to the recorded intensity pattern. The grating period Λ of the resulting grating is given through

$$\Lambda = \frac{\lambda}{2n\sin(\theta)}, \tag{2.2}$$

where λ is the wavelength of the laser, θ the angle between the two interfering beams, and n the refractive index of the photosensitive material. With a moderate effort, submicron structures down to $100\,nm$ can be fabricated.[82] Also large area elements can be produced by this parallel fabrication method. A drawback is the lack of flexibility and spatial variability. A schematic setup for holographic recording of gratings is shown in Fig. 2.4.

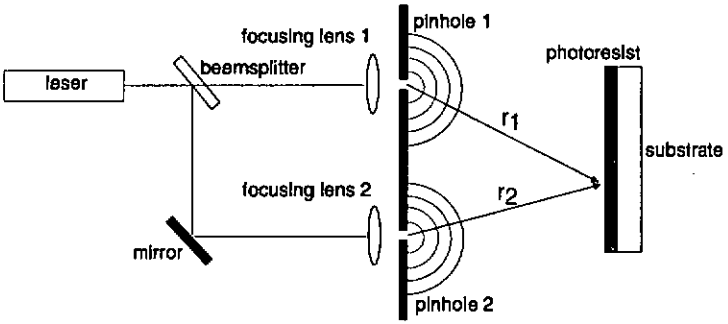

Figure 2.4: Schematic setup for the holographic recording of grating structures.

2.4 Melting resist technology

A well known method to fabricate refractive microlenses is the melting resist technology (reflow technique).[42, 13, 65] It is based on a photolithographic process as described in Subsection 2.1.1 Photoresist is deposited onto a substrate, typically a wafer, which is coated with a resist base layer and afterwards structured using standard photolithographic techniques. Since during the subsequent melting process the resist borders remain fixed, the photoresist pattern determines the geometry of the microlenses. With this approach nearly arbitrary border geometries of the microlenses can be obtained. Subsequently, the resist is melted in an oven and the microlenses are formed due to the surface tension of the liquid resist. The fabrication process is illustrated in Fig. 2.5. This process is well developed and spherical microlenses, for example, can be fabricated with diffraction limited optical quality.[64]

2.5 Reactive ion etching (RIE)

The methods described so far are suited to obtain microstructures in photoresist. Often it is desired to have the corresponding surface profile in a more rigid material, like fused silica, with better optical properties and more adequate spectral transmission. Reactive ion etching (RIE) is a technology that can be used to transfer a surface profile in photoresist into fused silica. In contrast to wet etching technologies, RIE is a highly anisotropic etching process, which is very advantageous for the transfer of diffractive and refractive microstructures. A comprehensive description of the transfer of

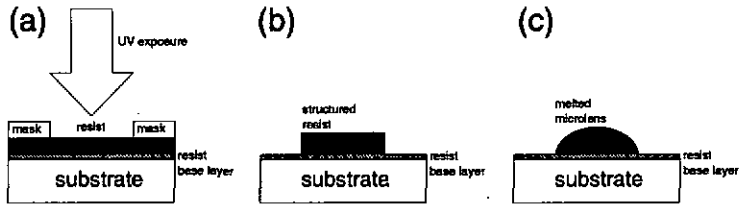

Figure 2.5: Fabrication of melting resist microlenses. (a) The photoresist is deposited onto a substrate with a resist base layer and exposed to UV light through a chromium mask. (b) The exposed resist is processed and free standing resist structures are created. (c) The microlenses are formed during melting in an oven.

photoresist structures into fused silica by RIE can be found in the dissertation of Eisner.[21] Different materials behave quite differently during the transfer by RIE. Fused silica is a well suited material. RIE transfer steps are also applied during the fabrication of multilevel surface relief profiles by binary mask technology, as described in Subsection 2.1.1. Here, after each photolithographic step, a RIE transfer step is applied to obtain the desired multilevel profile. RIE is a parallel technology, where all structures on a wafer are processed in one step.

Chapter 3

Theoretical background

In this chapter we introduce the theoretical background which is necessary for the understanding of the work presented in this thesis. We begin with the introduction of Maxwell's equations, the constitutive relations, and the boundary conditions, which provide the fundamental theoretical base of exact electromagnetic theory and therefore of optics. Afterwards, exact and approximate methods are introduced to solve the diffraction problem. Section 3.3 gives a short overview of how to propagate a given electromagnetic field in free space. The last section of this chapter introduces two iterative methods to calculate phase functions of diffractive optical elements.

3.1 Maxwell's equations, constitutive relations, and boundary conditions

Electromagnetic fields are described by the four Maxwell equations, which read in SI-units

$$\nabla \times \mathbf{E} + \dot{\mathbf{B}} = 0 \tag{3.1}$$

$$\nabla \times \mathbf{H} = \mathbf{J} + \dot{\mathbf{D}} \tag{3.2}$$

$$\nabla \cdot \mathbf{D} = \rho \tag{3.3}$$

$$\nabla \cdot \mathbf{B} = 0. \tag{3.4}$$

E, **B**, **D** and **H** are the electric field, the magnetic induction, the electric displacement, and the magnetic field, respectively. **J** and ρ are the electric current density and the electric charge density, respectively. The partial time derivative is denoted by a point above the corresponding vector. We only consider time-harmonic electromagnetic fields of angular frequency ω. Any time varying field can be decomposed into a spectrum of time-harmonic

fields via a Fourier analysis.[7, 34] The physical time-varying, electric and magnetic fields $\mathbf{E}(\mathbf{r},t)$ and $\mathbf{H}(\mathbf{r},t)$ can be expressed as

$$\mathbf{E}(\mathbf{r},t) = Re\{\mathbf{E}(\mathbf{r})\exp(-i\omega t)\} \quad (3.5)$$
$$\mathbf{H}(\mathbf{r},t) = Re\{\mathbf{H}(\mathbf{r})\exp(-i\omega t)\}, \quad (3.6)$$

where $Re\{\}$ stands for the real part of a complex number, t denotes time, and $\mathbf{r}$ is a vector containing the spatial coordinates. For the imaginary unit the symbol i is used. $\mathbf{E}(\mathbf{r})$ and $\mathbf{H}(\mathbf{r})$ on the right side of the equation are the complex representations of the physical fields and will be used in the following. Maxwell's equations for the time-harmonic case are then

$$\nabla \times \mathbf{E}(\mathbf{r}) = i\omega\mathbf{B}(\mathbf{r}) \quad (3.7)$$
$$\nabla \times \mathbf{H}(\mathbf{r}) = \mathbf{J}(\mathbf{r}) - i\omega\mathbf{D}(\mathbf{r}) \quad (3.8)$$
$$\nabla \cdot \mathbf{D}(\mathbf{r}) = \rho(\mathbf{r}) \quad (3.9)$$
$$\nabla \cdot \mathbf{B}(\mathbf{r}) = 0. \quad (3.10)$$

The material parameters enter via the consitutive relations which for linear isotropic media are

$$\mathbf{D}(\mathbf{r}) = \epsilon_0\epsilon(\mathbf{r})\mathbf{E}(\mathbf{r}) \quad (3.11)$$
$$\mathbf{B}(\mathbf{r}) = \mu_0\mu(\mathbf{r})\mathbf{H}(\mathbf{r}) \quad (3.12)$$
$$\mathbf{J}(\mathbf{r}) = \sigma(\mathbf{r})\mathbf{E}(\mathbf{r}). \quad (3.13)$$

$\epsilon(\mathbf{r})$ and $\mu(\mathbf{r})$ are the dielectric permittivity and the magnetic permeability of the medium, and $\sigma(\mathbf{r})$ is the specific conductivity. The constants ϵ_0 and μ_0, the permittivity and permeability of the vacuum, are given as

$$\epsilon_0 = 8.854 \cdot 10^{-12} AsV^{-1}m^{-1} \quad (3.14)$$
$$\mu_0 = 4\pi \cdot 10^{-7} VsA^{-1}m^{-1}. \quad (3.15)$$

The velocity of propagation in vacuum is defined by

$$c = \frac{1}{\sqrt{\epsilon_0\mu_0}} = 2.99792458 \cdot 10^8 \frac{m}{s}. \quad (3.16)$$

The refractive index $n(\mathbf{r})$ for the phase velocity in the material is then obtained via Maxwell's relation as

$$n(\mathbf{r}) = \sqrt{\epsilon(\mathbf{r})\mu(\mathbf{r})}. \quad (3.17)$$

Later, we will use a complex permittivity $\hat{\epsilon}$, and a correspondingly complex refractive index $\hat{n}$, defined by

$$(\hat{n}(\mathbf{r}))^2 = (n(\mathbf{r}) + i\kappa(\mathbf{r}))^2 = \hat{\epsilon}(\mathbf{r}) = \epsilon(\mathbf{r}) + i\frac{\sigma(\mathbf{r})}{\omega}, \quad (3.18)$$

where $\kappa(\mathbf{r})$ stands for the imaginary part of the complex refractive index. The sign of the imaginary part of the complex refractive index is determined by the geometry of the problem depending on whether the propagation of a wave field is in the positive or negative direction of the coordinate system.

The flow of electromagnetic energy is described by the Poynting vector

$$\mathbf{S} = \mathbf{E} \times \mathbf{H}. \tag{3.19}$$

The boundary conditions for the $\mathbf{D}$ and $\mathbf{E}$ fields at an interface between two different media, referenced by indices 1 and 2, are

$$\mathbf{n}_{12} \cdot (\mathbf{B}_2 - \mathbf{B}_1) = 0 \tag{3.20}$$

$$\mathbf{n}_{12} \cdot (\mathbf{D}_2 - \mathbf{D}_1) = \rho_s \tag{3.21}$$

$$\mathbf{n}_{12} \times (\mathbf{E}_2 - \mathbf{E}_1) = 0 \tag{3.22}$$

$$\mathbf{n}_{12} \times (\mathbf{H}_2 - \mathbf{H}_1) = \mathbf{J}_s, \tag{3.23}$$

where $\mathbf{n}_{12}$ is a unit vector pointing from media 1 to media 2. ρ_s and $\mathbf{J}_s$ stand for the surface charge density and the surface current density, respectively. Maxwell's equations (3.1)–(3.4) together with the constitutive relations (3.11)–(3.13) and the boundary conditions, (3.20)–(3.23), completely determine the solution for the linear isotropic case in the framework of classical electrodynamics.

3.2 Diffraction theory

In this section we introduce different methods to solve the diffraction problem. The exact electromagnetic solution, satisfying Maxwell's equations, is outlined, as well as approximative scalar methods. The exact solution takes fully into acount polarization effects, while within the approximative methods the polarization of the fields are only considered partially or not at all. In general, exact electromagnetic theory has to be used when the period of the grating structure is comparable to the wavelength of the incident wave. For grating periods much smaller or much larger than the wavelength approximative theories can be applied. For grating periods small compared to the wavelength, effective medium theories treat the diffraction grating as a homogenous birefringent layer,[107] while for large grating periods scalar diffraction theories are applicable. Scalar diffraction theory is treated in Subsection 3.2.2.

3.2.1 Exact electromagnetic diffraction theory

In Section 3.1 we introduced the base of electromagnetics in the form of Maxwell's equations, the constitutive relations, and the boundary conditions. Now, we present the application to the diffraction problem. We follow an approach formulated by Turunen,[95] where the details can be found. The most widespread name for this method is Fourier modal method (FMM), because of the Fourier expansion of the fields and the dielectric function. The method is especially suited for staircase like multilevel profiles as fabricated by binary photolithography, whereas continuous relief surface profiles need to be approximated by a sufficiently large number of grating layers. There exist other theories which can handle continuous surface profiles directly by employing a coordinate transform.[12]

The periodicity of a grating structure simplifies the problem considerably and allows an exact solution of Maxwell's equations. Approximations enter only via the finite number of terms retained in the expansions, and, in the case of a continuous surface profile, through the approximation by a multilevel profile. The validity of these approximations will be verified for concrete calculations by carefully checking the convergence properties of the solutions. An exact solution to the diffraction problem is found when the solution satisfies everywhere Maxwell's equations, together with the boundary conditions plus physically reasonable radiation conditions. Since analytical solutions can in general not be found, numerical solutions have to be applied.

The standard geometry of the diffraction problem, which is typically encountered when dealing with diffractive surface relief structures, is shown in Fig. 3.1. We restrict ourselves to the case where the problem is y-invariant and the incident plane wave is propagating in the x–z-plane. The general case, when the incident wave vector is not orthogonal to the grating grooves, is called conic diffraction, because the diffracted orders then appear on a cone rather than on a straight line. The conical diffraction problem can be decomposed into two problems with TE- and TM-polarization for perfectly conducting gratings.[68] In our case (Fig. 3.1), we assume a plane wave with TE- or TM-polarization incident on a structure with a periodically modulated refractive index. This generates a discrete spectrum of reflected and transmitted plane waves. The grating diffraction problem consists now of finding the complex amplitudes of these plane waves. The complex refractive indices, as defined in Eq. (3.18), are $\hat{n}_0$ and $\hat{n}_3$ for the two homogeneous regions $z < h$ and $z > h$, respectively. The region with the periodically modulated refractive index distribution has the height h, as shown in Fig. 3.1 for the case of two different refractive indices $\hat{n}_1$ and $\hat{n}_2$. In the general case, the modulated region can also contain more than two different refractive indices.

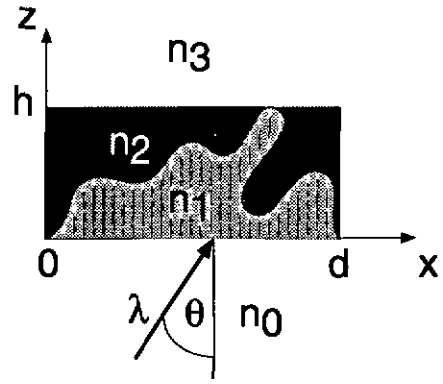

Figure 3.1: General geometry of a two dimensional diffraction grating (shown is one grating period).

The only restriction concerning the refractive indices is that the medium on the incident side is non–absorbing, therefore $\hat{n}_0$ must be real. All other refractive indices can be complex.

Maxwell's equations, (3.7)–(3.10), yield for the y–invariant case together with the constitutive relations, (3.11)– (3.13), the Helmholtz equations

$$\frac{\partial}{\partial x^2}E_y(x,z)+\frac{\partial}{\partial z^2}E_y(x,z)+k^2\hat{\epsilon}_r(x,z)E_y(x,z)=0 \qquad (3.24)$$

for TE–polarization, and

$$\frac{\partial}{\partial x}[\frac{1}{\hat{\epsilon}_r(x,z)}\frac{\partial}{\partial x}H_y(x,z)]+\frac{\partial}{\partial z}[\frac{1}{\hat{\epsilon}_r(x,z)}\frac{\partial}{\partial z}H_y(x,z)]+k^2H_y(x,z)=0, \quad (3.25)$$

for TM–polarization, where k is the wavenumber defined by $k=\omega/c$, and c is the speed of light in vacuum as defined in (3.16). Once $E_y(x,z)$ (TE) or $H_y(x,z)$ (TM) is found, the complementary components can be obtained by application of the appropriate Maxwell equation. Therefore, the $E_y(x,z)$ or the $H_y(x,z)$ component completely determines the solution of the diffraction problem. In the following, the scalar field U represents the component E_y or H_y which appears in the relevant Helmholtz equation.

As a consequence of the periodic refractive index distribution, with the help of the *Floquet–Bloch theorem, one can obtain a Fourier representation* of the diffracted part U_d of the total field U (incident and diffracted). It

takes the form

$$U_d(x,z) = \sum_{m=-\infty}^{\infty} G_m(z)\exp(i\alpha_m x), \tag{3.26}$$

where the α_m are given by

$$\alpha_m = \alpha_0 + \frac{2\pi m}{\Lambda}, \quad \alpha_0 = kn_0 sin\theta. \tag{3.27}$$

In the two homogeneous regions, the Helmholtz equations (3.24) and (3.25) reduce to Helmholtz equations with constant coefficients. Using the representation of U_d, as in Eq. (3.26), one obtains after insertion into Eqs. (3.24) or (3.25) for the coefficients

$$G_m = T_m \exp[it_m(z-h)] + R_m \exp[-it_m(z-h)]. \tag{3.28}$$

T_m and R_m correspond to the complex amplitudes of the transmitted and reflected orders of the electromagnetic field. The values t_m are given by

$$t_m = \sqrt{(k\hat{n}_3)^2 - \alpha_m^2}, \quad |\alpha_m| \leq kn_3 \tag{3.29}$$

$$t_m = i\sqrt{\alpha_m^2 - (k\hat{n}_3)^2}, \quad |\alpha_m| > kn_3. \tag{3.30}$$

By inserting the solution for G_m into Eq. (3.26), one finds for the transmitted part of the total field

$$U_t(x,z) = \sum_{m=-\infty}^{\infty} T_m \exp(i[\alpha_m x + t_m(z-h)]), \tag{3.31}$$

and for the reflected part

$$U_r(x,z) = \sum_{m=-\infty}^{\infty} R_m \exp(i[\alpha_m x - r_m z]), \tag{3.32}$$

where the r_m are given by

$$r_m = \sqrt{(kn_0)^2 - \alpha_m^2}, \quad |\alpha_m| \leq kn_0 \tag{3.33}$$

$$r_m = i\sqrt{\alpha_m^2 - (kn_0)^2}, \quad |\alpha_m| > kn_0. \tag{3.34}$$

Equation (3.27) corresponds to the commonly known grating equation which describes the directions of the transmitted and the reflected plane waves of order m as

$$n_3 sin(\theta_{m,t}) = n_0 sin(\theta_i) + m\frac{\lambda}{\Lambda}, \tag{3.35}$$

$$n_0 sin(\theta_{m,r}) = n_0 sin(\theta_i) + m\frac{\lambda}{\Lambda}, \tag{3.36}$$

where $\theta_{m,t}$ and $\theta_{m,r}$ correspond to the diffraction angles of the transmitted and reflected diffraction orders, respectively, and θ_i is the incident angle. The diffraction efficiencies are finally given by

$$\eta_{r,m} = Re\{r_m/r_0\}|R_m|^2 \quad \text{(TE)} \tag{3.37}$$

$$\eta_{r,m} = (\frac{n_0}{n_3})^2 Re\{r_m/r_0\}|R_m|^2 \quad \text{(TM)} \tag{3.38}$$

$$\eta_{t,m} = Re\{t_m/r_0\}|T_m|^2 \quad \text{(TE)} \tag{3.39}$$

$$\eta_{t,m} = (\frac{n_0}{n_3})^2 Re\{t_m/r_0\}|T_m|^2 \quad \text{(TM)}, \tag{3.40}$$

The complex amplitudes T_m and R_m of the diffracted transmitted and reflected plane waves are still unknown and have to be determined by the boundary conditions.

In order to find solutions for the fields inside the modulated region, we use an eigenmode method for the z-invariant case.[11, 43, 67, 49] A general profile, as shown in Fig. 3.1, can then be treated by slicing the continuous profile into a sufficiently large number of slabs S_i which are then piecewise approximately constant. We start with the Helmholtz equation for TE-polarization, as given in Eq. (3.24). After separation of variables, $E_y(x,z) = X(x)Z(z)$, we find

$$Z(z) = a\exp(i\gamma z) + b\exp(-i\gamma(z-h)), \tag{3.41}$$

where γ is the separation constant, and the coefficients a and b will be determined by the boundary conditions. With the pseudo-periodic ansatz

$$P = \sum_{m=-\infty}^{\infty} P_m \exp(i\alpha_m x) \tag{3.42}$$

and the Fourier series representation

$$\hat{\epsilon} = \sum_{m=-\infty}^{\infty} \hat{\epsilon}_m \exp(i2\pi m x/\Lambda), \tag{3.43}$$

of the dielectric function, we obtain as the result a linear system of equations written in matrix form

$$\mathbf{MP} = \gamma^2 \mathbf{P}. \tag{3.44}$$

$\mathbf{M}$ stands for the matrix

$$M_{lm} = k^2 \hat{\epsilon}_{l-m} - \alpha_m^2 \delta_{lm}, \tag{3.45}$$

δ_{lm} for the Kronecker symbol, and $\mathbf{P}$ for the vector P_l. This standard eigenvalue problem can then be solved for the eigenvalues γ_n^2, and the corresponding eigenvector elements P_{ln}. The complete solution can therefore be written as

$$E_y(x,z) = \sum_{l=-\infty}^{\infty} \sum_{n=1}^{\infty} P_{ln} \exp(i\alpha_l x)(a_n \exp(i\gamma_n z) + b_n \exp(-i\gamma_n(z-h))) \quad (3.46)$$

with the coefficients a_n and b_n, which have to be determined by the boundary conditions. The sign convention is $Re\{\gamma_n\} + Im\{\gamma_n\} > 0$ in order to extract the independent solutions.

For TM-polarization, similar as for TE-polarization, a pseudo-periodic ansatz

$$H_y(x,z) = (a\exp(i\gamma z) + b\exp(-i\gamma(z-h))) \sum_{m=-\infty}^{\infty} P_m \exp(i\alpha_m x) \quad (3.47)$$

is made for the relevant field component H_y. With the definition of the function

$$Q(x,z) = \frac{1}{\epsilon_r} \frac{\partial}{\partial z} H_y(x,z) \quad (3.48)$$

and its pseudoperiodic expansion

$$Q(x,z) = i\gamma(a\exp(i\gamma z) - b(-i\gamma(z-h))) \sum_{m=-\infty}^{\infty} Q_m \exp(i\alpha_m x) \quad (3.49)$$

one obtains

$$P_l = \sum_{m=-\infty}^{\infty} \epsilon_{l-m} Q_m. \quad (3.50)$$

Using the expansion of the inverse dielectric function

$$\frac{1}{\epsilon_r(x)} = \sum_{m=-\infty}^{\infty} \xi_m \exp(i2\pi x/\Lambda), \quad (3.51)$$

one finally gets a linear system of equations, written in matrix form as

$$\mathbf{MNQ} = \gamma^2 \mathbf{Q}. \quad (3.52)$$

The elements of the matrices $\mathbf{N}$ and $\mathbf{M}$ are given through

$$N_{lm} = \epsilon_{l-m} \quad (3.53)$$

$$M_{lm} = k^2 \delta_{lm} - \alpha_l \xi_{l-m} \alpha_m. \quad (3.54)$$

After solving the linear system of equations for the eigenvectors Q_l and the eigenvalues γ_n, one obtains P_l from Eq. (3.50) and finally the complete solution

$$H_y(x,z) = \sum_{l=-\infty}^{\infty}\sum_{n=1}^{\infty} P_{ln}\exp(i\alpha_l x)(a_n\exp(i\gamma_n z) + b_n\exp(-i\gamma_n(z-h))). \quad (3.55)$$

For the general multilevel case with S surface levels and therefore $S-1$ slabs, the Eigenvalue problem is solved in each slab separately with no additional complication. The final solutions for E_y in Eq. (3.46) and H_y in Eq. (3.55) get an additional index s for the corresponding layer, and the P_{ln}, a_n, and b_n are replaced by $P_{ln,s}$, $a_{n,s}$, and $b_{n,s}$, respectively, where s counts the slabs.

The complex amplitudes R_m and T_m in Eqs. (3.37), (3.39), (3.38), and (3.40), and the coefficients $a_{n,s}$ and $b_{n,s}$ in Eqs. (3.46) and (3.55) have to be determined from the boundary conditions. For TE–polarization the continuity of E_y and H_x, Eqs. (3.22) and (3.23), and therefore also $\partial E_y/\partial z$, Eq. (3.7), is used. For TM–polarization the continuity of H_y and E_x, Eqs. (3.23) and (3.22), and therefore also of $\partial H_y/\partial z$ and the function Q, Eq. (3.48), using Eq. (3.7), is exploited. For a single slab grating the boundaries at $z = 0$ and $z = h$ are used, while for multilayer gratings the additional $S-1$ internal boundaries are used as well. At these boundaries the surface normal is parallel to the z–direction. Therefore the E_y component for TE–polarization or the H_y component for TM–polarization component has to be continuous across all these boundaries. In the general multilayer case the said conditions result in two systems of equations which for TE–polarization reads

$$\sum_{m=-\infty}^{\infty}(a_{m,s}\exp(i\gamma_{m,s}(z_s - z_{s-1})) + b_{m,s})P_{lm,s} =$$
$$\sum_{m=-\infty}^{\infty}(a_{m,s+1} + b_{m,s+1}\exp(i\gamma_{m,s+1}(z_{s+1} - z_s)))P_{lm,s+1} \quad (3.56)$$
$$\sum_{m=-\infty}^{\infty}(a_{m,s}\exp(i\gamma_{m,s}(z_s - z_{s-1}) - b_{m,s})\gamma_{m,s}P_{lm,s} =$$
$$\sum_{m=-\infty}^{\infty}(a_{m,s+1} - b_{m,s+1}\exp(i\gamma_{m,s+1}(z_{s+1} - z_s)))\gamma_{m,s+1}P_{lm,s+1} \quad (3.57)$$

and for TM–polarization

$$\sum_{m=-\infty}^{\infty}(a_{m,s}\exp(i\gamma_{m,s}(z_s - z_{s-1})) + b_{m,s})P_{lm,s} =$$

$$\sum_{m=-\infty}^{\infty} (a_{m,s+1} + b_{m,s+1} \exp(i\gamma_{m,s+1}(z_{s+1} - z_s)))P_{lm,s+1}, \qquad (3.58)$$

$$\sum_{m=-\infty}^{\infty} (a_{m,s} \exp(i\gamma_{m,s}(z_s - z_{s-1}) - b_{m,s})\gamma_{m,s}Q_{lm,s} =$$

$$\sum_{m=-\infty}^{\infty} (a_{m,s+1} - b_{m,s+1} \exp(i\gamma_{m,s+1}(z_{s+1} - z_s)))\gamma_{m,s+1}Q_{lm,s+1}. \qquad (3.59)$$

The Eqs. (3.46) and (3.55) together with Eqs. (3.56)–(3.59) represent the complete solution of the diffraction problem. The diffraction efficiencies are given by Eqs. (3.37)–(3.40) and the fields in the homogeneous regions by Eqs. (3.31) and (3.32).

For the numerical implementation of the solution of the boundary value problem, we followed the solution as published by Moharam et al.[62] with improvements for the TM–case as published by Lalanne and Morris.[52] The explanation for the nature of this improvement can be found in the publication of Li.[56] For the numerical calculations all matrices have to be truncated. For accurate results all propagating orders and a sufficient number of evanescent orders have to be taken into account. The "sufficient" number of orders N, which is proportional to Λ/λ, can be determined by controlling the proper convergence of the solutions as a function of orders retained in the calculations. For dielectric gratings this is not critical. Care has to be taken for metallic gratings with high conductivity, especially for TM–polarization. The dimension of the eigenvalue matrix is NxN, the size of the boundary–value matrix is $2NS$x$2NS$, where the number of slabs is $S - 1$. The computation time is proportional to N^3, memory requirements are proportional to N^2.

There are many other approaches to solve the diffraction problem in a rigorous way. The rigorous coupled wave method (RCWA) [61] is very similar to the method shown here. The main difference is the representation of the fields inside the grating structure. Exact modal methods use a superposition of exact modal functions of the periodic grating structure which are known for specific grating geometries.[60] Other approaches to find exact solutions of Maxwell's equations are the differential method,[68] where the propagation equations are directly integrated, or the integral method which necessitates a tensor formalism for the handling of coordinate transformations.[68] While for the dielectric gratings practically all methods show identical results, the performance of the methods can differ significantly for highly conductive, metallic gratings, especially for TM–polarization.

3.2.2 Scalar diffraction theory

The diffraction theory introduced so far is exact in the sense that an exact solution of Maxwell's equations is obtained for a given diffraction problem. For large grating periods compared to the wavelength of the incident light approximative solutions of the grating problem are possible. In the following two paragraphs we introduce two appproximative methods to obtain the complex amplitude behind a diffractive structure: the thin element approximation and the optical path model.

The thin element approximation

For diffraction gratings with $\Lambda >> \lambda$, the solution of the diffraction problem with exact electromagnetic theory becomes computationally heavy because of the large matrices involved in the eigenvalue and boundary value problems. On the other hand, if $\Lambda >> \lambda$, then the angular spectrum of the diffracted plane waves concentrate around the z-axis and the use of scalar theory is justified. As a rule of thumb, the scalar theory gives reliable results when the grating period is at least one order of magnitude larger than the wavelength. Because of the simplicity compared to exact electromagnetic theory, scalar theories are applied whenever justified. It should be mentioned that scalar theory can produce accurate results for grating structures, even when it is not theoretically justified (see Paragraph 4.1.3).

In the so-called thin element approximation (TEA) the effect of a transmission grating with height h is described by a complex transmission function $t(x,y)$, which relates pointwise the incident field $u_{in}(x,y,0)$ and the transmitted field $u_t(x,y,h)$ by

$$u_t(x,y,h) = t(x,y)u_{in}(x,y,0) \tag{3.60}$$

in three-dimensional notation. When assuming that, in the simplest approximation, the light passes the grating structure without deflection, the complex transmission function $t(x,y)$ of a grating with a refractive index distribution $n(x,y,z)$ is given for a normally incident light field by

$$t(x,y) = \exp\left(ik\int_0^h n(x,y,z)dz\right). \tag{3.61}$$

The increased path length for non-normal incidence can be taken into acount by an additional cosine-factor in the integral. The complex amplitudes of the diffracted waves are then

$$T_{mn} = \frac{1}{\Lambda_x\Lambda_y}\int_0^{\Lambda_x}\int_0^{\Lambda_y} u_t(x,y,h)\exp(-i2\pi(\frac{mx}{\Lambda_x}+\frac{ny}{\Lambda_y}))dxdy, \tag{3.62}$$

where Λ_x and Λ_y are the grating periods in x- and y-direction, respectively. The diffraction efficiencies of the order mn are finally $\eta_{mn} = |T_{mn}|^2$, independent of polarization.

The optical path model

The optical path model allows to calculate diffraction efficiencies of gratings more accurately than the thin element approximation. At the same time the optical path model is computationally much more efficient than exact electromagnetic theory. This method is sometimes also called phase sensitive raytracing.[39, 71, 10] In order to obtain the complex amplitude of the wavefield at $z = h$ behind the grating, a number of rays which are evenly distributed over the grating period are traced through the grating structure. For each ray the optical path length is calculated. At interfaces with different refractive indices n_1 and n_2 Snell's law of refraction

$$n_1 \sin(\theta_1) = n_2 \sin(\theta_2), \tag{3.63}$$

is applied, where θ_1 and θ_2 are the angle of incidence and the angle of the transmitted rays with respect to the surface normal, respectively. The new directions of the rays are determined and the polarization dependent Fresnel losses are calculated. The reflection and transmission coefficients ρ and τ, for the amplitudes at an interface between two different refractive indices are given by

$$\rho_{\mathrm{TE}} = -\frac{\sin(\theta_1 - \theta_2)}{\sin(\theta_1 + \theta_2)} \tag{3.64}$$

$$\rho_{\mathrm{TM}} = \frac{\tan(\theta_1 - \theta_2)}{\tan(\theta_1 + \theta_2)} \tag{3.65}$$

$$\tau_{\mathrm{TE}} = \frac{2\sin(\theta_1)\cos(\theta_2)}{\sin(\theta_1 + \theta_2)} \tag{3.66}$$

$$\tau_{\mathrm{TM}} = \frac{2\sin(\theta_1)\cos(\theta_2)}{\sin(\theta_1 + \theta_2)\cos(\theta_1 - \theta_2)}. \tag{3.67}$$

The subscripts indicate the two orthogonal polarizations TE and TM. The reflectivity R and the transmittivity T are then given by

$$R = |\rho|^2 \tag{3.68}$$

$$T = |\tau|^2 \frac{n_2 \cos(\theta_2)}{n_1 \cos(\theta_1)}. \tag{3.69}$$

Once the complex amplitude behind the grating has been determined, the diffraction efficiencies of the different orders are calculated by a Fourier transform as in Eq. (3.62).

The optical path model is a scalar method, whereas the polarization of the incident wavefront enters via the polarization dependent Fresnel losses at the interfaces. This method will be used in Section 5.4 for the analysis of deep structures with large grating periods. Because of the depth of these grating structures, large differences between simple scalar theory and exact electromagnetic theory are observed. The optical path model provides an efficient tool to analyze such structures, because exact calculations are very time and memory intensive due to the large grating periods.

3.3 Propagation of light fields

In the previous sections we introduced exact and approximative methods to calculate the change of the complex amplitude of an incident wave caused by a diffractive structure. In Subsections 3.3.1 and 3.3.2 we shall treat the propagation of light fields in free space.

3.3.1 Wave optics

As shown in Subsection 3.2.1, Helmholtz equations (3.24) and (3.25) for the electromagnetic fields can be deduced directly from Maxwell's equations. The general solution of the Helmholtz equation in a homogeneous and isotropic medium can be expressed with the help of Green's theorem [34] as

$$U(P) = \frac{1}{4\pi} \int\int_S \left\{ \frac{\partial U}{\partial n} G - U \frac{\partial G}{\partial n} \right\} ds, \tag{3.70}$$

which is known as integral theorem of Helmoltz and Kirchhoff. G is a Green function of the Helmholtz equation. The formula expresses the scalar field U at a point P in terms of the values of this field on any closed surface S surrounding this point P. The expression $\partial/\partial n$ stands for the partial derivative in the outward direction at each point on the surface S. This formula plays a crucial role in the development of scalar diffraction theory for the propagation of light fields.

The integral theorem of Helmholtz and Kirchhoff can be applied to a plane screen, as schematically shown in Fig. 3.2(a). The points P and $\tilde{P}$ indicate two point sources in mirror position to each other with respect to the screen. $\vec{r}_{12}$ and $\vec{\tilde{r}}_{12}$ are the corresponding vectors pointing from the point sources to the screen. Using the corresponding Green function

$$G_-(r_{12}) = \frac{\exp(ikr_{12})}{r_{12}} - \frac{\exp(ik\tilde{r}_{12})}{\tilde{r}_{12}} \tag{3.71}$$

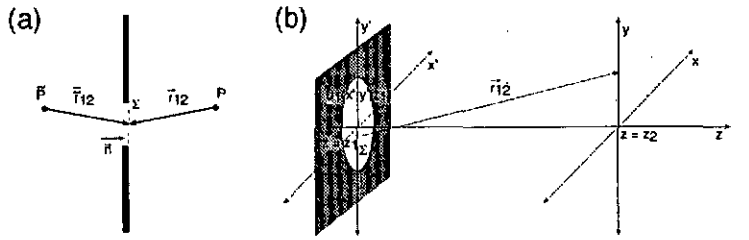

Figure 3.2: Geometry for the application of the integral theorem of Helmoltz and Kirchhoff to the case of a plane screen (a), and (b) for the first Rayleigh–Sommerfeld diffraction integral as in Eq. (3.72).

with Kirchhoff boundary conditions,[44] results in the first Rayleigh–Sommerfeld diffraction integral [31]

$$u_2(x,y,z_2)_I = -\frac{1}{2\pi}\int\int_\Sigma u_1(x',y',z_1)(ik-\frac{1}{r_{12}})\frac{z_{12}}{r_{12}}\frac{\exp(ikr_{12})}{r_{12}}dx'dy', \quad (3.72)$$

which describes the field u_2 in the plane $z = z_2$. The geometry is illustrated in Fig. 3.2(b). Hereby is $u_1(x',y',z_1)$ the incident wave field within the free aperture Σ of the screen, $k = 2\pi/\lambda$, z_{12} the distance between the screen and the plane at $z = z_2$, $r_{12} = \sqrt{z_{12}^2 + (x-x')^2 + (y-y')^2}$, and λ the wavelength. Hereby the Sommerfeld radiation condition is used, which means that the radiating fields vanish at least as fast as a diverging spherical wave.[86]

For $r_{12} >> \lambda$ the first Rayleigh–Sommerfeld integral Eq. (3.72) can be simplified to

$$u_2(x,y,z_2)_I = \frac{1}{i\lambda}\int\int_\Sigma u_1(x',y',z_1)\frac{\exp(ikr_{12})}{r_{12}}\frac{z_{12}}{r_{12}}dx'dy'. \quad (3.73)$$

Using in the Green function of Eq. (3.71), a plus sign instead of the minus sign, and again assuming $r_{12} >> \lambda$, leads to the second Rayleigh–Sommerfeld diffraction integral [31]

$$u_2(x,y,z_2)_{II} = \frac{1}{2\pi}\int\int_\Sigma \frac{\partial u_1(x',y',z_1)}{\partial n}\frac{\exp(ikr_{12})}{r_{12}}dx'dy'. \quad (3.74)$$

The second Rayleigh–Sommerfeld diffraction integral (3.74) with the derivative of the field is rarely used, because in most cases rather the field itself than the derivative of the field on the plane screen is known. In the following

we will therefore use the Rayleigh–Sommerfeld diffraction integral given in Eq. (3.72).

In summary, the Rayleigh–Sommerfeld diffraction integral, Eq. (3.72), allows to propagate a given scalar wave field in free space in a rigorous way. The only asumptions are the validity of the Sommerfeld radiation condition and the Kirchhoff boundary conditions. For Eqs. (3.73) and (3.74) additionally the propagation distance has to be larger than the wavelength, i.e. $r_{12} >> \lambda$.

Equivalent to the Rayleigh–Sommerfeld diffraction integral, but based on a different concept, the transfer function concept, is the angular spectrum approach.[34] An optical system is described as a linear system characterized by a transfer function $H(p_x, p_y)$, where p_x and p_y are the spatial frequencies in the x– and y–directions. The propagated wave field u_2 is then given by

$$u_2(x, y, z_2) = \int\int u_1(x', y', z_1) h(x - x', y - y') dx' dy', \qquad (3.75)$$

where h is the impulse response of the system and linked to $H(p_x, p_y)$ via a Fourier transform. For free space propagation the transfer function is

$$H(p_x, p_y) = \exp\left(i2\pi z_{12}\sqrt{(\frac{1}{\lambda})^2 - p_x^2 - p_y^2}\right). \qquad (3.76)$$

This leads to a different, but mathmatically equivalent form of the Rayleigh–Sommerfeld diffraction integral

$$u_2(x, y, z_2)_I = FT^{-1}\left\{FT\{u_1(x', y', z_1)\} \exp\left(i2\pi z_{12}\sqrt{(\frac{1}{\lambda})^2 - p_x^2 - p_y^2}\right)\right\}, \qquad (3.77)$$

which is significantly more efficient for the numerical implementation. Hereby the convolution theorem of the Fourier transform was used. The operators FT and FT^{-1} stand for the Fourier and the inverse Fourier transform, respectively. The convolution formulation can speed up the execution on a computer by orders of magnitude compared to the direct evaluation of the Rayleigh–Sommerfeld integral, especially for the 2–dimensional case, because of the available very efficient fast Fourier transform (FFT) algorithms. The angular spectrum representation (3.77) and the Rayleigh–Sommerfeld integral (3.72) can be transformed into each other via the Weyl representation of a spherical wave.[59]

The first Rayleigh-Sommerfeld diffraction integral, approximated to the second order, results in

$$u_2(x,y,z_2) = \frac{\exp(ikz_{12})}{i\lambda z_{12}} \cdot \int\int u_1(x',y',z_1)\exp\left(i\frac{k}{2z_{12}}\left[(x-x')^2+(y-y')^2\right]\right)dx'dy', \quad (3.78)$$

which is the well known Fresnel integral. It can be cast into the form

$$u_2(x,y,z_2) = \frac{\exp(ik(z_{12}+\frac{x^2+y^2}{2z_{12}}))}{i\lambda z_{12}} FT\left\{u_1(x',y',z_1)\exp(ik\frac{x'^2+y'^2}{2z_{12}})\right\}, \quad (3.79)$$

which is more convenient for a numerical implementation. For large propagation distances, the Fresnel integral (3.78), can further be approximated to the first order as

$$u_2(x,y,z_2) = \frac{\exp(ik(z_{12}+\frac{x^2+y^2}{2z_{12}}))}{i\lambda z_{12}} FT\{u_1(x',y',z_1)\}, \quad (3.80)$$

which is the Fraunhofer or far field approximation. In contrast to the Rayleigh–Sommerfeld integral, which is valid in general, the accuracy of the Fresnel or Fraunhofer integrals depend on the length of the propagation distance compared to the lateral extension of the field. A detailed description for the optimum numerical evaluation of the Fresnel and Fraunhofer integrals can be found in the dissertation of Vokinger.[98]

3.3.2 Geometrical optics

In geometrical optics the light field is described by rays. The rays in turn are defined by the condition that the they are normal to the phase front of the wave field. Geometrical optics is a valid description for light fields when transverse phase and amplitude variations on the scale of the optical wavelength are small, and therefore diffraction effects can be neglected. The path of the light rays in an optical system is described by repeated application of the law of refraction and reflection at a sequence of homogeneous media separated by discrete interfaces. In Subsection 3.2.2 an optical path model, based on geometrical optics, was described to calculate the complex amplitude change behind a diffractive structure. The fundamental law, which governs ray optics, is Snell's law of refraction

$$n_1\sin(\theta_1) = n_2\sin(\theta_2). \quad (3.81)$$

It describes the refraction of light at an interface between two different refractive indices n_1 and n_2. θ_1 and θ_2 are the angle of incidence and the angle of the transmitted rays with respect to the surface normal. For diffractive elements the grating Eqs. (3.35) and (3.36) are used to determine the directions of the various diffraction orders. It is possible to transform a ray distribution back into a wavefront by using the condition that the rays are normal to the phase front of the wave field. Therefore it is possible to combine wave optics and geometrical optics to describe an optical system. There are many commercial raytracing programs available, for example TracePro™, Raytrace™, Zemax™, and Code V™. The main advantage of these programs is their ability to analyze and optimize optical systems.

3.4 Iterative calculation of phase functions

Diffractive optical elements (DOEs) are often applied to solve beamshaping problems, where a certain input wave has to be converted into a specific intensity pattern. The spatial location of the desired intensity pattern is often the Fourier plane, but any other plane is possible. Typical beamshaping applications are the conversion of a Gaussian beam into a flat-top, or fan-out elements for spot array generation. The basic problem is now to find for a given beamshaping problem the optimum design of the diffractive element. Usually only DOEs are considered that influence the phase of the incident wave, because then no absorption occurs and 100% diffraction efficiency is possible.

In the following we introduce two different design methods for the iterative calculation of phase functions. The first algorithm is the so-called iterative Fourier transform algorithm (IFTA) which is well suited for continuous phase elements or multilevel phase elements with at least 8 phase levels per 2π phase difference. The second method, the simulated annealing (SA) optimization algorithm, is a non-linear optimization method that works well for any kind of multilevel elements, while a drawback can be the long computation time for larger design problems.

3.4.1 The iterative Fourier trausform algorithm

The iterative Fourier transform algorithm (IFTA) has been developed by Gerchberg and Saxton in 1972.[32] Since then, many authors have contributed to generalize and improve the algorithm.[26, 35, 106, 105, 20] It is an algorithm that can be used for the far-field optimization of a DOE. Here we address the special case of a fan-out optimization, but the algorithm is also capable of

optimizing more general optical functions. The IFTA is schematically shown in Fig. 3.3. The amplitudes of the various diffraction orders with indices ij

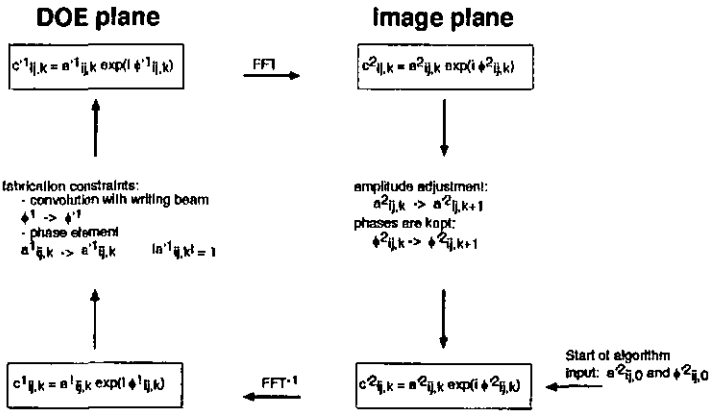

Figure 3.3: Flow-chart of the iterative Fourier transform algorithm (IFTA) for far-field fan-out optimization.

are the $a_{ij,k}$ and the phasese are the $\phi_{ij,k}$. The subscript k counts the number of iterations and the superscripts 1 and 2 refer to the DOE and the image plane, respectively. The starting point for the optimization is generally the desired amplitude or intensity distribution for the various orders in the image plane. Random values are chosen for the phases. Then, an inverse Fourier transform is executed and the amplitudes $a^1_{ij,k}$ are set to unity, since pure phase elements are desired. The inverse Fourier transform is used because the wave field in the plane of the DOE and the far field amplitudes are related via a Fourier relationship as shown in Eq. (3.80). In the standard algorithm the corresponding phases $\phi^1_{ij,k}$ are maintained. Fabrication effects, like the convolution of the diffractive phase element with the Gaussian writing beam in direct laser writing, can be taken into account and compensated for. This will be shown in more detail in Section 4.2. Now a Fourier transform is executed. The obtained amplitudes $a^2_{ij,k}$ are then adjusted with respect to the desired values, while the phases $\phi^1_{ij,k}$ are maintained. The quality of the solution, especially the uniformity error, can be improved considerably by balancing the amplitudes according to

$$a^{r2}_{ij,k+1} = a^{r2}_{ij,k} \frac{< a^2_{ij,k} >}{a^2_{ij,k}}, \tag{3.82}$$

where $< a_{ij,k}^2 >$ is the average over all diffracted fan–out amplitudes.[38, 70] This terminates the first iteration step. Iterations are executed till a predefined termination criteria is reached, typically the efficiency and uniformity, or the number of iteration steps. The algorithm allows to optimize continuous phase elements. There are modified algorithms which can directly optimize multilevel diffractive phase elements.[25]

3.4.2 Non–linear optimization by simulated annealing (SA)

The phase profiles of the diffractive elements which are designed with the standard IFT algorithmus are continuous. When multilevel elements are designed with the IFTA, the phase values are usually clipped to the allowed multilevel niveaus after the optimization is finished. The clipping causes binarization noise, which is in most cases tolerable for 16 or 8 phase levels, but causes a strong degradation of performance for 4–level or binary elements. In contrast, the SA method for the optimization of multilevel diffractive phase elements does not have this drawback and allows a direct global optimization of the phase profiles.[45] The basic principle of the SA method was introduced by Kirkpatrick in 1983 [47, 46] with a physical analogy. The optimization process is compared to an annealing process where a solid is coerced into a low energy state.

A multilevel diffractive phase element is described by a matrix with $N \times N$ pixel, where each pixel has a discrete value. During the SA optimization procedure all the pixel are visited in turn and their values changed to another discrete value. Then, the merit function is evaluated and compared to the merit function value before the pixel change. If the merit function value decreases, the pixel change is accepted. If the merit function has an increased value, the change is only accepted with a probability $p = \exp(-\Delta E/k_B T)$, which is commonly known as Boltzmann factor, where ΔE is the difference of the merit function value before and after the pixel change. This difference can be interpreted as energy difference and therefore the denominator be considered as thermal energy $k_B T$ because of the analogy to the annealing process, with k_B the Boltzmann constant and T the temperature. For the optimization process the numerator and denominator are pure numbers of course. This procedure allows the algorithm to escape from local minima because pixel changes which increase the merit function value are also accepted with an exponential probability. If the temperature T is reduced slowly enough and the optimization parameters are properly chosen so that the system is always nearly in equilibrium, the algorithm tends to the global

minimum of the merit function. The main drawback of this method is the computational effort, because a large number of merit function evaluations have to be executed. Whether this method is appropriate for a given problem depends mainly on the size of the matrix that has to be optimized and on the complexity of the merit function that has to be evaluated.

Chapter 4

Realization of phase functions: ideal and real

The designed ideal phase function of a DOE is in general continuous. This translates for surface relief DOEs into continuous surface relief profiles where normally the thin element approximation, as described in Subsection 3.2.2, is used to relate the surface relief profile to the phase function. The real fabrication of such continuous relief surface profiles is non-ideal in the sense that *the ideal profile cannot be fabricated, but only a best approximation to* the ideal profile. The common point of the two sections in this chapter is the fundamental problem of how to implement best a given phase function as surface relief profile by taking into account the inevitable constraints of the corresponding fabrication method. In Section 4.1 we address the encoding problem for multilevel surface relief structures, as fabricated by binary mask photolithography in combination with RIE. Section 4.2 introduces a method to compensate the influence of the finite width of the writing beam for the fabrication of continuous surface relief DOEs by direct laser beam writing.

4.1 Encoding of diffractive phase functions

4.1.1 Introduction

In modern optics, diffractive microlenses are appreciated because of the additional degrees of freedom they bring to the design compared with conventional refractive optics. They can be found for example in collimating and focusing optics, in optical diffusers, chromatic-aberration correction optics or in athermalized hybrid elements.[6, 4, 85] When designing optical systems, raytracing programs offer the possibility to include arbitrary phase functions,

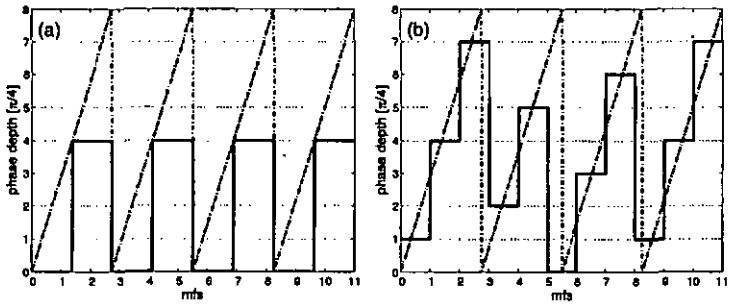

Figure 4.1: Illustration of the two encoding methods AQ (a) and DS (b) for a linear blazed grating with $\Lambda_b/mfs = 2.75$. The ideal phase function of the linear blazed grating is the dash-dotted line, the solid line is the multilevel profile obtained with DS and AQ. The horizontal grid lines are the 8 available phase levels.

which can be realized by DOEs, in order to take advantage of this additional freedom. The designed phase functions are in the general case continuous and have to be quantized into a multilevel staircase like profile for a fabrication by the multilevel approach.[88] The number of discrete phase levels per 2π phase steps depends on the minimum feature size, mfs, which can be fabricated. For the coding of the continuous lens function into the multilevel profile, different approaches are possible and several papers have appeared in recent years,[103, 51, 41, 55] which have adressed the problem of finding the optimum encoding procedure for a given phase function and given fabrication constraints. A simple, standard way of coding is analytical quantization (AQ).[89, 54] In AQ [89] (Fig. 4.1(a)) the phase function is clipped to values between 0 and 2π, then the transition points for 2π phase jumps are determined and regions between these transitions are encoded. The number of phase values between two transitions is determined by dividing the distance between the transitions by the mfs and rounding this value to the integer closest to zero. However, this procedure gives only satisfying results as long as 4 or more discrete phase levels are possible per 2π phase difference of the lens function. For high aperture lenses or short wavelengths, AQ gives an efficiency of the lens which is significantly smaller than the optimum value.[103] The AQ method is illustrated in Fig. 4.1(a) for a blazed grating with $\Lambda_b/mfs = 2.75$. Since the grating period is smaller than $3\,mfs$, AQ encoding results in a simple binary grating, using only two of the available 8 phase levels.

A more advanced method is the radially symmetric iterative discrete on-axis (RSIDO) coding, developed by Welch et al.[103, 41] The quantized phase function is obtained by optimizing the energy in a signal window for a given optical setup. This method produces also at the edge of the lens, where only 2 to 3 phase levels are possible per grating period Λ_b, nearly optimum results. The major drawback of this method is the fact that it utilizes nonlinear techniques, like simulated annealing, for the optimization of the widths and locations of the quantized phase levels. It therefore consumes considerable computing power, especially for lenses with large diameters and small *mfs*.

Knittinen and Herzig [51] described a different, more straightforward way to solve the coding problem, which they called Direct Sampling (DS). Direct Sampling is a straightforward method to obtain directly the encoded phase profile from a continuous phase function. This method gives automatically the optimum efficiency of a diffractive lens whereas the coding scheme convinces with its simplicity. With DS coding the complete lens function is sampled with the *mfs* and phase values are clipped between 0 and 2π. These phase values are then rounded to the closest available phase level. The DS method is illustrated in Fig. 4.1(b) for a blazed grating with $\Lambda_b/mfs = 2.75$. In the outermost part of a diffractive high aperture lens, only 2 or 3 phase levels are possible per 2π phase difference, because of the limitations by the *mfs*. We will call this part of the profile the binary region. Fig. 4.1 shows a part of the binary region, where 2.75 *mfs* fit into one grating period. While the performance of the different coding schemes is most critical in the binary region, this area can account for a large fraction of a high aperture lens and therefore has a great impact on the total performance. For example, a spherical lens with $NA = 0.32$ operating at $\lambda = 632.8\,nm$ has a binary area of 59 % when a *mfs* of $1\,\mu m$ is assumed.

In the binary region, assuming a *mfs* of $1\,\mu$m and the wavelength range of the visible spectrum, one is clearly outside the range of validity of scalar diffraction theory.[69] The DS method for encoding is based on simple scalar theory and so far has not been rigorously investigated. Here, we investigate the DS method with exact electromagnetic grating theory and compare the two polarization cases.[73, 74] We fabricated and characterized test structures which were encoded using the DS method and compare the measured diffraction efficiencies with the values obtained by exact electromagnetic diffraction theory. The work on the encoding problem has been focused so far mainly on the diffraction efficiencies of the encoded phase functions. The influence of the encoding method on the quality of the wavefront and therefore on the focal spot size or the Strehl ratio has not yet been investigated. We analyzed quantitatively the influence of the encoding scheme on the quality of the wavefront for an incident plane wave which is focused by a cylindrical lens

encoded by DS and AQ. For this we compared the FWHM of the focal spot and the Strehl ratio of the DS and AQ encoded cylindrical lenses with the ideal case. While for AQ the periodicity of the phase function to be encoded is maintained, DS shows a principally different behaviour. In the general case DS enlarges the periodicity of the underlying phase function thus generating additional diffraction orders in between the main orders. We discuss the consequences of this difference between the two encoding schemes.

4.1.2 Theoretical background and numerical methods

For the rigorous calculations we used the eigenmode method as described in Subsection 3.2.1. For the entire analysis, the diffraction efficiencies were calculated for a linearly polarized plane wave under normal incidence. The standard propagation direction was substrate to air and the refractive index of the substrate was 1.5, if not otherwise indicated.

In order to determine whether the quantized phase profiles obtained with DS are still the optimum solutions with the highest diffraction efficiencies when analyzed rigorously, we introduced a "rigorous steepest gradient optimization" (RSGO) method. The sampling of the lens function was hereby kept constant, 1 *mfs*. The starting point for the optimization procedure was the phase level distribution obtained with DS, as for example illustrated in Fig. 4.1(b) by the solid line. Using this distribution, the first phase level was changed one level up ($\pi/4$ for 8 level coding), or down, while all the others were kept constant, and rigorous diffraction efficiencies were calculated for the new distribution. The same was then done with every other phase level until all levels had been changed once and corresponding efficiencies were calculated. The new phase level distribution was then chosen as the one with the highest diffraction efficiency in the corresponding order. This new phase level distribution was the starting point for the next iteration step. Iterations were executed until no further improvement of diffraction efficiency could be achieved. Since non-uniformly distributed phase levels are only of advantage for very weak lenses,[55] we used equally separated phase levels for the encoding. Since the RSGO is a steepest gradient optimization, it cannot be excluded that the algorithm ends in a local maximum. On the other hand, utilizing a nonlinear optimization technique like simulated annealing, which avoids stagnation in local maxima quite effectively, is inappropriate because of the time consuming rigorous calculations. However, for some phase level distributions, we used simulated annealing, and obtained the same maximum diffraction efficiencies as with RSGO.

In order to obtain the focal plane intensities of the cylindrical lenses we propagated the fields using the first Rayleigh-Sommerfeld diffraction inte-

gral as given in Eq. (3.72).[103, 51] The scalar diffraction efficiencies for the DS and AQ encoded gratings were calculated via a Fourier transform, as described in Eq. (3.62). We analyzed DS encoded blazed gratings since any arbitrary lens function can locally be considered as a blazed grating. The local period of a blazed grating Λ_b and therefore the Λ_b/λ ratios are smallest in the binary region, where only 2 to 3 *mfs* are possible per grating period for a given diffractive lens with design wavelength λ. This means that differences between scalar and exact electromagnetic theory are most likely to appear there. We therefore concentrated our rigorous analysis on the binary region.

4.1.3 Results and discussion

Rigorous analysis of DS blazed gratings in the binary region

When a blazed grating with a certain grating period Λ_b is DS encoded into a multilevel surface profile, the formal period of the grating increases, because in general the 2π phase steps of the blazed grating do not coincide with the DS steps of 1 *mfs*. This has to be considered for the calculation of diffraction efficiencies, since here the periodicity of the structure is of fundamental importance. The grating period of the DS blazed grating Λ is determined through $\Lambda = m \cdot \Lambda_b$ with m obtained from the condition $m \cdot \Lambda_b = n \cdot mfs$, where m and n are smallest non-zero integers. As illustrated in Fig. 4.1(b), the blazed grating with period $\Lambda_b = 2.75\, mfs$ coincides with the DS steps of $1 mfs$ after $m = 4$ periods. The grating period of the DS encoded grating is therefore 11 *mfs*. For a standard blazed grating the first order diffraction efficiency is of concern. However, for the DS encoded blazed gratings the grating period is increased by the above mentioned factor m. As a consequence, the direction of the first order for the blazed grating corresponds to the m^{th} order of the DS encoded grating. Therefore, it is this order which has to be optimized in the calculations.

We applied exact electromagnetic diffraction theory to the DS encoding method in order to determine the limits of validity of the scalar-based method. The rigorous analysis of the DS blazed grating was done for eight different Λ_b/mfs ratios in the binary region, namely 2, 2.2, 2.25, 2.4, 2.5, 2.6, 2.75, 2.8, for both polarizations. First, we calculated the rigorous diffraction efficiencies for the various Λ_b/mfs ratios by varying λ while keeping the grating period Λ_b constant. Then the RSGO was executed for a Λ_b/λ range of 1 to 7, again for fixed Λ_b. A representative part of the results is shown in Figs. 4.2 and 4.3. The results for Λ_b/mfs values of 2.25 and 2.75 are shown in Fig. 4.2 for TE-polarization, and in Fig. 4.3 for TM-polarization. Each graph contains three diffraction efficiency curves: The DS encoded phase level

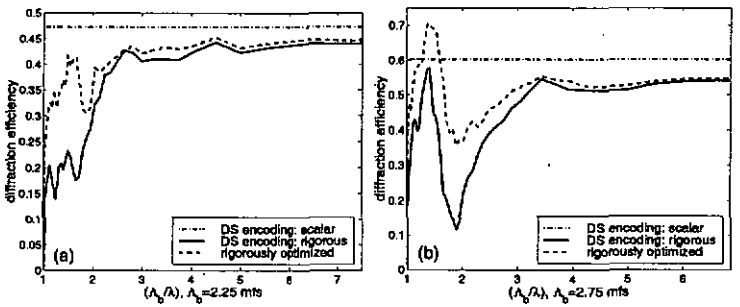

Figure 4.2: Calculated diffraction efficiencies for TE-polarization as a function of A_b/λ with constant A_b for blazed gratings with (a) $A_b/mfs = 2.25$, and (b) $A_b/mfs = 2.75$. For the phase depth of 2π, 8 equally spaced phase levels were available.

distribution, calculated with exact electromagnetic theory (solid lines) and simple scalar theory (dashed-dotted lines), and the RSGO optimized phase level distribution calculated with exact electromagnetic theory (dashed lines). For large A_b/λ ratios the diffraction efficiencies approached the scalar values (dash-dotted lines), as expected. However, the rigorous values are always a few percent below the scalar values, since in scalar diffraction theory no Fresnel losses and reflected orders are taken into account. For A_b/λ between 2 and 3, the diffraction efficiency exhibits a strong decrease followed by a peak, as can be seen for example in Fig. 4.2. This behaviour can be understood qualitatively as an occurrence of total internal reflection at the interface.[63]

The important criterion for the performance of the encoding method is the A_b/λ ratio until which the scalar-based encoding method DS produces phase level distributions which cannot significantly be improved when optimized using exact electromagnetic theory (RSGO). This ratio will be designated $(A_b/\lambda)_0$. We determined $(A_b/\lambda)_0$ for the eight different A_b/mfs ratios in the binary region for both polarizations. The $(A_b/\lambda)_0$ were determined by the condition that for all A_b/λ ratios larger than $(A_b/\lambda)_0$ the rigorously optimized solutions show an improvement in diffraction efficiency of less than 3% over the solutions obtained with DS. The $(A_b/\lambda)_0$ ratios are shown in Table 4.1 for TE- and TM-polarization. The most important result of the analysis in the binary region is, that the values for $(A_b/\lambda)_0$ are between 2 and 3.3, which is surprisingly small. This means, that the DS method can be reliably applied to wavelengths of up to $0.85\,mfs$ which corresponds to NA = 0.43. The rigorous diffraction efficiencies are somewhat smaller than the corresponding

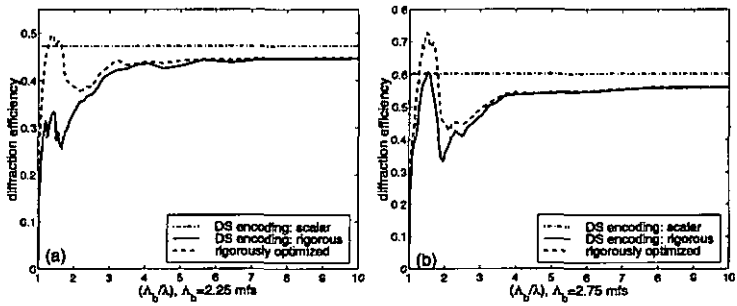

Figure 4.3: Calculated diffraction efficiencies for TM-polarization as a function of Λ_b/λ with constant Λ_b for blazed gratings with (a) $\Lambda_b/mfs = 2.25$, and (b) $\Lambda_b/mfs = 2.75$. For the phase depth of 2π, 8 equally spaced phase levels were available.

Table 4.1: $(\Lambda_b/\lambda)_0$ values for different Λ_b/mfs ratios of the DS blazed grating in the binary region (8 equally spaced levels were available for 2π phase).

Λ_b/mfs	$(\Lambda_b/\lambda)_0$, TE-pol.	$(\Lambda_b/\lambda)_0$, TM-pol.
2.0	2.0	1.8
2.2	2.2	2.0
2.25	2.3	2.1
2.4	2.8	2.1
2.5	2.3	2.0
2.6	2.9	2.2
2.75	3.3	2.5
2.8	3.3	2.3

Table 4.2: $(\Lambda_b/\lambda)_0$ values for different Λ_b/mfs ratios of the DS blazed grating in the binary region (8 equally spaced levels were available for 2π phase, TE-polarization). The propagation direction is reversed: air to substrate.

Λ_b/mfs	$(\Lambda_b/\lambda)_0$
2.25	2.3
2.5	3.2
2.75	3.6

scalar values, the phase level profiles are however, under the given fabrication constraints and the constant sampling of the lens function, the best possible. The values which were obtained for $(\Lambda_b/\lambda)_0$, between 2 and 3.3 for TE-polarization, and between 2 and 2.8 for TM-polarization, are very small compared to the normal validity range of scalar diffraction theory for grating structures ($(\Lambda_b/\lambda) >\approx 10$).[69] The values for TM-polarization are hereby even smaller than the values obtained for TE-polarization. The results show that simple DS encoding ensures optimum performance in the above sense over a very wide Λ_b/λ range for both polarizations, from the scalar regime to deep into the rigorous regime ($\Lambda_b/\lambda \approx 2-3$), whereas the validity is even more extended for TM- than for TE-polarization. In the regime $\Lambda_b/\lambda < (\Lambda_b/\lambda)_0$, where the DS quantized phase profiles have diffraction efficiencies as low as 11%, the rigorously optimized solutions show large improvements of up to 25% for TE-polarization, and up to 22% for TM-polarization. Therefore, the optimization potential is comparable for TE- and TM-polarization while the validity of DS is more extended for TM- than for TE-polarization.

The results shown so far were obtained for propagation direction substrate to air, which is the standard case for a diffractive microlens. In the following we present for TE-polarization results for the inversed propagation direction, air to substrate, for three selected Λ_b/mfs ratios, 2.25, 2.5 and 2.75, in the binary region. All the other parameters remained unchanged. The results of the calculations are given in Table 4.2. The diffraction efficiencies as a function of Λ_b/λ show for the propagation direction air to substrate no significantly different behaviour than for the inversed one. The $(\Lambda_b/\lambda)_0$ ratios, which were obtained in the same way as for the propagation direction substrate to air, are in a similar range, between 2.3 and 3.6.

Calculation of rigorous diffraction efficiencies for cylindrical lenses

For the calculation of rigorous diffraction efficiencies of cylindrical lenses which were DS encoded, we approximated the ideal lens function of a fo-

cusing diffractive lens [51] by a series of blazed gratings with piecewise constant, and towards the center of the lens increasing, grating periods. The basic principle of this method is illustrated in Fig. 4.4. In the binary region, the same discrete grating period to *mfs* ratios as given in Table 4.1 were used, namely 2, 2.2, 2.25, 2.4, 2.5, 2.6, 2.75, 2.8. For the larger grating periods, blazed gratings with the following grating periods to *mfs* ratios were used for the approximation: 3, 3.5, 4, 4.5, 5, 5.5, 6, 6.5, 7. We then computed the total first order lens diffraction efficiency for TE-polarization by adding up the various contributions from the different parts of the lens. The calculations were carried out for cylindrical lenses with $2\,mm$ diameter and 8-level DS encoding. The *mfs* was assumed to be $1\,\mu m$ and the focal length was chosen so that the lens had a local grating period of $2\,mfs$ at the edge. Efficiencies were computed for three wavelengths, $\lambda = 0.75$, 1.0 and $1.25\,\mu$m, corresponding to NA of 0.38, 0.5 and 0.63. Our analysis covered the outer part of the lens until a local grating period of $7\,mfs$ was reached. Since for larger grating periods, corresponding to the innermost part of the lens, the performance is in a good approximation scalar and the influence of the coding scheme on the performance of a lens becomes negligible. We would like to point out, that for the high aperture lenses studied here, the analyzed fraction was the dominating part of the lens, with 76% to 81% of the total lens area. The results are summarized in Table 4.3. The corresponding scalar values are also listed for comparison, where one has to keep in mind that the values for scalar diffraction efficiencies do not include Fresnel reflection losses. The important result is that the difference in diffraction efficiency between the rigorously optimized encoding and the simple DS encoding is quite small for all three lenses in spite of their quite high NA. For the lens with NA = 0.38 the difference amounts to only 1.7%. Furthermore, the absolute value is already quite close to the scalar one, when considering the additional Fresnel losses for the scalar calculation. As expected, with increasing NA the difference

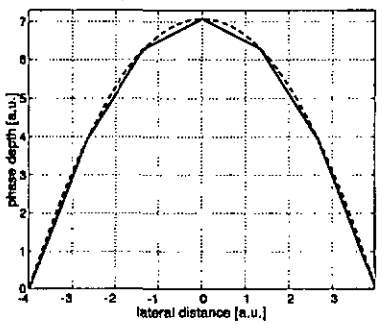

Figure 4.4: Phase profile of a high aperture cylindrical lens (dashed), and piecewise linear approximation (solid). For the calculations we used a finer approximation than shown in the figure.

Table 4.3: **Rigorous and scalar first order diffraction efficiencies η_1 of the outer area for cylindrical lenses. DS encoding with 8 phase levels (TE–polarization).**

	$\lambda = 0.75\ mfs$ NA = 0.38	$\lambda = 1.0\ mfs$ NA = 0.5	$\lambda = 1.25\ mfs$ NA = 0.63
analyzed fraction of total lens:	76.7 %	78.1 %	80.2 %
η_1: DS, scalar[1]	64.5 %	63.6 %	62.3 %
η_1: DS, rigorous	56.2 %	49.0 %	42.0 %
η_1: rigorously optimized	57.9 %	52.6 %	48.1 %

between DS encoding and rigorously optimized value gets larger, because the Λ_b/λ ratios are smaller and one is therefore deeper in the rigorous regime. The absolute differences of 3.6% and 6.1% are, however, still very small when considering the very high NA of 0.5 and 0.63, respectively.

Optimization potential of extended scalar depth correction using DS

It is known from extended scalar theory [90] that for perfectly blazed gratings the highest diffraction efficiency is obtained for a grating depth, d_{EST}, which is shallower than the depth corresponding to the 2π phase difference predicted by simple scalar theory,[72] namely

$$d_{EST} = \frac{\lambda}{n_1 - n_2 \cos(\arcsin(\lambda/\Lambda_b))}. \tag{4.1}$$

The incident wavelength is λ, n_1 and n_2 are the refractive indices of the two materials on the incident and transmitted side, respectively, and Λ_b denotes the grating period. This reduced depth can be explained geometrically by optical path considerations. The utility of this depth correction in order to increase the diffraction efficiency of a high aperture lens depends on the manufacturing process. If a direct writing technique is used, the correction of the depth leads always to an improvement, because the depth can be adjusted to the local grating period. For a mask based process this is different, because the phase levels for the element have to be chosen for the whole diffractive element independent of the grating period. This means that for a given wavelength the corrected depth is only correct for one specific grating period. For all other grating periods it is more or less inappropriate. The

[1] The scalar efficiencies are not accurate for this kind of high NA diffractive lenses, they are shown for comparison only.

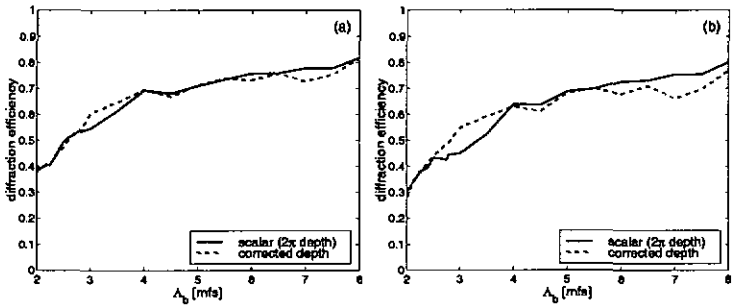

Figure 4.5: Rigorous diffraction efficiencies as a function of Λ_b for scalar 2π depth (solid line) and corrected depth, according to extended scalar theory (dashed line), for a DS blazed grating. The grating depth was corrected for the middle of the binary region, $\Lambda_b = 2.5\,mfs$. For the phase depth of 2π, 8 equally spaced phase levels were available. Figures (a) and (b) are calculated for $\lambda = 0.75\,mfs$ and $1\,mfs$, respectively.

question which now arises naturally is, whether one can achieve an improvement in total diffraction efficiency for the whole lens if this depth correction is applied. Consequently, in this section we investigate rigorously the optimization potential of grating depth correction according to extended scalar theory when applied to the DS method. Concerning the fabrication constraints, we again assumed 8 available phase levels and a mfs of $1\,\mu m$.

When comparing the rigorous optimum depths of blazed gratings with the optimum depths obtained from extended scalar theory, one finds a qualitative agreement for $\Lambda_b/\lambda \geq 2.8$. Till $\Lambda_b/\lambda \approx 2.2$ extended scalar theory gives at least the right tendency. On the other hand, a significant improvement of at least a few percent in diffraction efficiency is only possible for $\Lambda_b/\lambda \leq 4.5$. We therefore chose for the analysis a DS blazed grating with a corrected depth according to extended scalar theory and calculated rigorous diffraction efficiencies as a function of grating period for various wavelengths. The grating depth was corrected for the middle of the binary region, $\Lambda_b = 2.5\,mfs$. The results for wavelengths of $0.75\,mfs$ and $1\,mfs$ are given in Fig. 4.5(a) and (b), respectively. The results show, as already mentioned, that the gain in diffraction efficiency for the small grating periods is inevitably connected with a loss in diffraction efficiency for the larger ones. In order to study this effect for a practical example, we calculated the diffraction efficiencies for the three cylindrical high aperture lenses from the preceding section for TE-polarization. We included in the analysis the outer part of the lens until

Table 4.4: **Rigorous first order diffraction efficiencies η_1 of the outer area for cylindrical lenses. DS encoding with 8 phase levels for scalar 2π depth and a corrected depth according to extended scalar theory (TE–polarization).**

	$\lambda = 0.75\ mfs$ NA = 0.38	$\lambda = 1.0\ mfs$ NA = 0.5	$\lambda = 1.25\ mfs$ NA = 0.63
fraction of total lens:	78.0 %	79.4 %	81.4 %
η_1: scalar 2π depth	56.5 %	49.4 %	42.1 %
η_1: corrected depth	57.1 %	50.7 %	43.5 %

a local grating period of $8\ mfs$ was reached. The results are summarized in Table 4.4. The diffraction efficiencies for the cylindrical lenses with corrected depth, following extended scalar theory, Eq. (4.1), show only a marginal improvement between 0.6 and 1.4%. Hereby the innermost part of the lenses, which amounts to about 20% in the above cases, is not included in the calculations.

When considering the results displayed in Fig. 4.5, one has also to take into account the fact, that the design according to extended scalar theory introduces in the remaining center area additional diffraction efficiency losses. We therefore conclude that the design according to extended scalar theory has, in terms of total lens diffraction efficiency, no advantages over the design according to simple scalar theory for a mask based fabrication process. The simple design for the encoding of the diffractive lens results in a better performance.

Fabrication and characterization of DS encoded blazed gratings

We fabricated DS encoded linear blazed gratings with 8 phase levels in fused silica with $\Lambda_b = 2.25\ mfs$ and $2.75\ mfs$ for mfs of $1\,\mu m$, $1.5\,\mu m$, and $2\,\mu m$, and characterized the corresponding diffraction efficiencies for both polarizations. The characterization wavelengths were $632.8\,nm$ and $900\,nm$, which results in 6 measurement points per Λ_b/mfs ratio. The gratings were fabricated for the 2 design wavelengths by a three-step photolithographic process, where each lithographic step is followed by a RIE step in order to produce the 8–level surface profile (see Subsection 2.1.1). The fabrication process was carried out at CSEM in Neuchâtel. Figure 4.6 shows SEM pictures of the fabricated structures with $\Lambda_b = 2.25\ mfs$ and $\Lambda_b = 2.75\ mfs$, respectively, for a mfs of $2\,\mu m$. The numbers from 0 to 7 indicate the corresponding 8 phase levels. Subsequently, we compared the measured diffraction efficiencies to the values obtained by exact electromagnetic diffraction theory. The

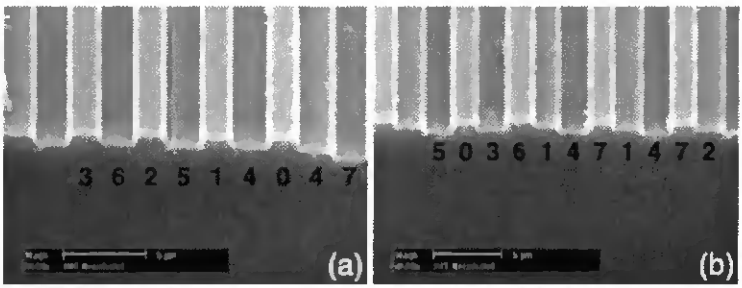

Figure 4.6: SEM pictures of the fabricated 8 level DS encoded blazed gratings in fused silica. (a) for a grating period of 2.25 *mfs*, (b) for a grating period of 2.75 *mfs*. The numbers from 0 to 7 indicate the 8 different phase levels.

results are shown in Fig. 4.7 for TE and TM polarization for $\Lambda_b = 2.25\ mfs$, and in Fig. 4.8 for $\Lambda_b = 2.75\ mfs$ for TE and TM polarization. We found good agreement between the experimental and theoretical values for both polarizations, wheras the measured efficiencies were slightly lower than the theoretical values, which is due to the alignment errors between the subsequent photolithographic steps during the fabrication process.

Encoding influence on the focal spot

In order to investigate the influence of the encoding method on the quality of the focal spot, we calculated the focal spot size (FWHM) and the Strehl ratio as a function of *mfs*, for DS and AQ encoded cylindrical lenses, as well as for the ideal case. We addressed especially high aperture lenses, since there the influence of the encoding method is most evident. The Strehl ratio for the DS and AQ encoded lenses was defined as the peak intensity in the focal plane divided by the peak intensity of the ideal lens. The focal plane was defined by the on axis point with the highest intensity. In Figure 4.9 the focal spot size and the Strehl ratio are shown for cylindrical microlenses with a radius of $r = 200\,\mu m$, 8 phase levels, a wavelength of $0.5\,\mu m$, and the minimum focal length, depending on *mfs*, which is determined by the smallest possible grating period of $2\ mfs$ at the edge of the lens. The phase function ϕ of the ideal lens is hereby given through

$$\phi(\rho) = (2\pi/\lambda)(f - \sqrt{f^2 + \rho^2}), \tag{4.2}$$

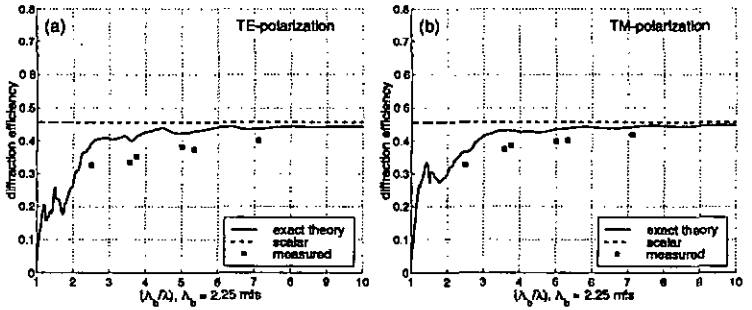

Figure 4.7: Experimental and theoretical diffraction efficiencies for (a) TE- and (b) TM-polarization. The gratings are 8-level DS encoded in fused silica with $\Lambda_b = 2.25 mfs$.

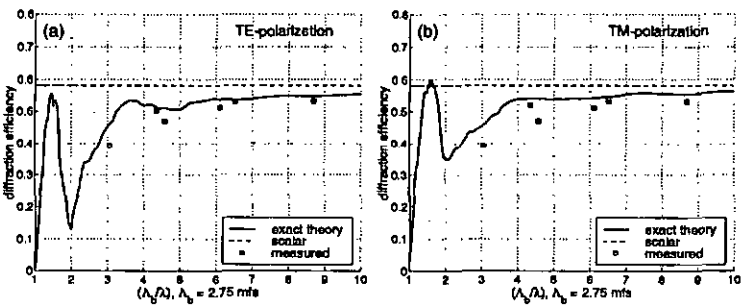

Figure 4.8: Experimental and theoretical diffraction efficiencies for (a) TE- and (b) TM-polarization. The gratings are 8-level DS encoded in fused silica with $\Lambda_b = 2.75\ mfs$.

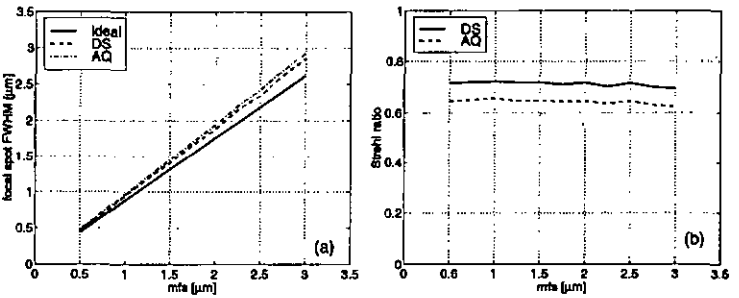

Figure 4.9: Focal spot sizes (FWHM) and Strehl ratios for DS and AQ encoded cylindrical lenses compared to the ideal case. (a) FWHM as a function *mfs*, (b) Strehl ratio as a function of *mfs*.

where f is the focal length, ρ the radial coordinate, and λ the wavelength. The focal spot sizes for DS, AQ, and the ideal case show all a nearly linear dependence on *mfs*. The three curves seem to originate with different slopes from one common point. The difference in the focal spot size between DS and AQ is quite small compared to the difference between DS and the ideal case. As expected, DS produces smaller focal spots than AQ for all *mfs*, and the difference between DS, AQ and the ideal case vanishes when the *mfs* approaches the wavelength ($0.5\,\mu m$). In our investigation, we characterized the focal spot by the FWHM. For other definitions like full width at $1/e^2$ intensity level or the width between the first two minima, we expect no significantly different results. The Strehl ratios for DS and AQ do not achieve the diffraction limited value of 0.8. The Strehl ratios are practically independent of the *mfs* for the maximum numerical aperture lenses studied here. The average value for DS is 0.71 and 0.64 for AQ. The formula of Marechal [7]

$$D_s = 1 - 4\pi^2 (W_{\rm rms}/\lambda)^2, \tag{4.3}$$

relates the Strehl ratio D_s with the wavefront aberrations (rms) $W_{\rm rms}$ for a given wavelength λ. Using this formula we find for the DS encoded lens $W_{\rm rms} = 0.086\,\lambda$ and for the AQ encoded lens $W_{\rm rms} = 0.095\,\lambda$. Therefore the wavefront aberrations caused by the encoding are about 10% smaller for DS than for AQ in the case of the investigated high aperture lenses.

Due to the enlarged period of the DS encoded blazed gratings, compared with the non-encoded blazed phase function, there are additional diffraction orders created between the main diffraction orders. This principal difference between the two encoding schemes is illustrated in Fig. 4.10 for DS and AQ

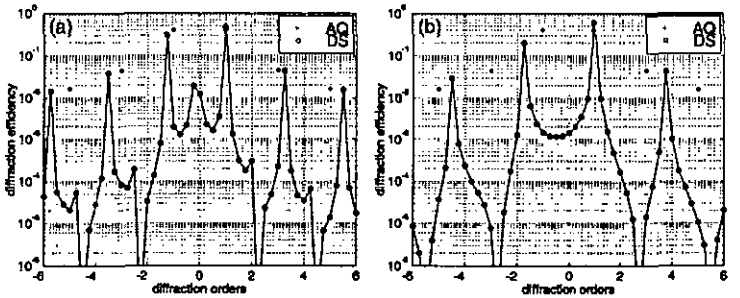

Figure 4.10: Efficiencies in the various diffraction orders for DS and AQ encoded blazed gratings. (a) for $\Lambda_b = 2.25\,mfs$, (b) for $\Lambda_b = 2.75\,mfs$. The even orders of the AQ encoded gratings are missing, since for this case they are simple binary gratings with a phase depth of π.

encoded blazed gratings with $\Lambda_b = 2.25\,mfs$ and $\Lambda_b = 2.75\,mfs$. It can be observed that there are additional diffraction orders generated in between the main diffraction orders, but that the absolute magnitude is very small, roughly one to two orders of magnitude smaller than the main orders. This is consistent with the results for the focal spot sizes and the Strehl ratios. The difference between the focal spot sizes is quite small for DS and AQ, since the intermediate diffraction orders have a very small influence because of the small magnitude, while the Strehl ratio differs significantly for DS and AQ, beause the first order efficiencies of DS are significantly higher than for AQ.

4.1.4 Conclusions

We have investigated the scalar based encoding method of Direct Sampling (DS) from the point of view of exact electromagnetic diffraction theory. In particular, we analyzed ideal blazed gratings in the binary region, that is the region, where the *mfs* allows only 2 to 3 phase levels within one grating period. We found that quantized phase profiles obtained with scalar DS are, under given fabrication constraints, close to the optimum solutions, even for grating period to wavelength ratios (Λ_b/λ) as small as about 2 to 3.3. The validity of the method is even more extended for TM- than for TE-polarization. This proves the usefulness of DS as an efficient encoding method that can be applied to a range of Λ_b/λ, which exceeds the validity of scalar diffraction theory. It has also been shown, that for even smaller Λ_b/λ

ratios the phase profiles obtained by DS can be improved by a straightforward "rigorous steepest gradient optimization". For certain Λ_0/λ ratios the improvement is as large as 11% to 36%.

We calculated rigorous lens diffraction efficiencies for high aperture focusing cylindrical lenses, encoded with DS, by approximating them as a series of linear blazed gratings with varying grating periods. We showed that the difference in diffraction efficiency between rigorously optimized encoding and simple DS encoding is quite small, even for large numerical apertures (NA = 0.63) of the lenses. Furthermore, the values were quite close to the expectations from scalar diffraction theory.

Additionally, we rigorously investigated the optimization potential of grating depth correction according to extended scalar theory when applied to the DS encoding. Here we found that for a mask based fabrication process the design according to extended scalar theory has no advantage over simple scalar theory.

We fabricated and characterized 8-level DS encoded blazed gratings in fused silica and found good agreement between the experimental and the theoretical diffraction efficiencies, which were calculated by exact electromagnetic diffraction theory. We compared the influence of the encoding schemes DS and AQ on the quality of the focal spot. Hereto, we compared the size (FWHM) of the focal spot and the Strehl ratio of the DS and AQ encoded, focusing, cylindrical lenses with the case of the ideal lens.

4.2 Spot compensation for laser direct writing

4.2.1 Introduction

Direct laser beam writing is a flexible and fast method to fabricate continuous relief diffractive grating structures. It is described in more detail in Section 2.2. A basic inherent problem hereby is that for small grating periods Λ relative to the width of the writing beam σ (FWHM) the ideal diffractive structure is distorted. In a simple but accurate model [39, 40] the resulting surface relief profile $z(x,y)_{real}$ can be described as a convolution of the ideal surface profile $z(x,y)_{ideal}$ with a Gaussian writing beam:

$$z(x,y)_{real} = z(x,y)_{ideal} \otimes g(x,y). \tag{4.4}$$

The symbol $\otimes$ stands for the convolution operation. The function

$$g(x,y) = c\exp\left(-\frac{x^2}{2\sigma_x^2} - \frac{y^2}{2\sigma_y^2}\right) \tag{4.5}$$

describes the Gaussian beam, where σ_x and σ_y are the FWHM of the Gaussian writing beam in the two orthogonal directions, and c is a normalization constant. The main distortions of the ideal profile occur at the 2π phase jumps of the surface profile.

4.2.2 Theoretical background

For 1-D grating structures the number of 2π phase jumps can be reduced by increasing the profile depth to multiples of 2π, and using the corresponding higher diffraction orders. Therefore the performance of 1-D diffracting grating structures can already be partially improved with respect to the finite size of the writing beam by simply reducing the number of 2π phase jumps that occur. The drawback of this approach are the more severe fabrication tolerances because of the increased profile depth. For 2-D structures the method of working in higher diffraction orders is in general not possible, except if the 2π phase steps form a closed line as for example for lens like structures.[8]

There are other methods based on pixelwise optimization of the diffractive structure [39, 40] to compensate for the writing beam convolution. They can principally be applied to 2-D diffractive grating structures, but have the disadvantage of being computationally heavy and therefore rather appropriate for simple 1-D structures, like blazed gratings. The work of Ebbets,[18] where an IFT algorithm was used to optimize writing spot compensated fan-out structures, was restricted to 1-D fan-out structures. The experimental results showed relatively large deviations from the theoretical results because of the limited accuracy of the moving stages.

We implemented an IFT algorithm including writing spot compensation which can be applied for the optimization of arbitrary 1-D and 2-D fan-out structures. The algorithm is fast and can handle large amounts of data. We show experimental results confirming the theoretical results for 1-D and 2-D fan-outs. The algorithm is an IFTA, as described in Subsection 3.4.1, where during the step with the fabrication constraints a convolution with the writing beam is performed. The characteristic parameter for the writing spot compensation is the ratio of the FWHM of the writing beam to the period of the fan-out grating.

4.2.3 Theoretical and experimental results

Using the IFTA we optimized two different 1-D fan-outs and one 2-D fan-out. Subsequently, we fabricated the fan-out gratings by direct laser writing and characterized the efficiencies and uniformities. Tables 4.5 and 4.6 show

Table 4.5: **Table with theoretical results for various compensated and non–compensated 1–D and 2–D fan–outs. Shown are the efficiencies and uniformities.**

	eff non-comp.	unif non-comp.	eff comp.	unif comp.
1x9 fan–out	87.1%	0.34	95.4%	< 0.001
1x15 fan–out	81.3%	0.73	96.9%	< 0.001
4x4 fan–out	84.0%	0.12	87.0%	< 0.001

Table 4.6: **Table with experimental results for various compensated and non–compensated 1–D and 2–D fan–outs. Shown are the efficiencies and uniformities.**

	eff non-comp.	unif non-comp.	eff comp.	unif comp.
1x9 fan–out	84.8%	0.54	94.5%	0.21
1x15 fan–out	80.6%	0.82	94.6%	0.17
4x4 fan–out	81.4%	0.44	84.7%	0.25

the theoretical and experimental results which were obtained for the compensated and non–compensated fan–outs, respectively. The efficiencies and uniformities of the non–compensated fan–outs in Tables 4.5 and 4.6 were obtained after convolution of the ideal phase profile with the writing beam. For the 1–D case we chose a 1x9 and a 1x15 fan–out, and for the 2–D case a 4x4 fan–out. They were characterized by their efficiencies and uniformities. The uniformity of a fan–out is defined by unif $= (I_{max} - I_{min})/(I_{max} + I_{min})$ where I_{max} and I_{min} is the maximum and the minimum intensity of the corresponding fan–out orders, respectively. The FWHM of the writing beam was $\sigma = 1.1\,\mu m$. For the 1–D fan–outs the grating period was $35.6\,\mu m$, and for the 2–D fan–outs the grating period was $37.6\,\mu m$. For the 1–D case we found that the efficiencies and the uniformities of the fan–outs could be improved considerably by the writing spot compensation algorithm. Concerning the improvements we found a very good agreement between the theoretical and experimental values for the efficiencies and uniformities. By comparing the absolute values of the uniformity, we observe an additional offset for the experimental values, which is caused by small deformations of the ideal structures due to stage instabilities occured during the writing procedure. This effect was observed for the compensated as well as for the non–compensated fan–outs. For the 1x9 fan–out the efficiencies improved by 8.3% (theoretically) and 9.7% (experimentally). The corresponding uniformities improved

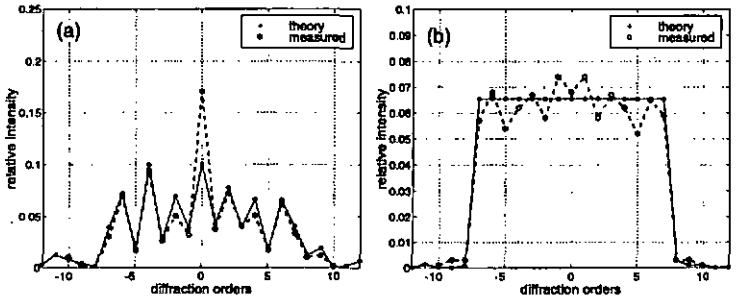

Figure 4.11: Comparison between the theoretical and experimental intensities in the various diffraction orders for the (a) non-compensated and (b) compensated 1x15 fan-out.

by 0.34 (theoretically) and 0.33 (experimentally). For the 1x15 fan-out the efficiencies improved by 15.6% (theoretically) and 14% (experimentally). The corresponding improvements of the uniformities amounted to 0.73 (theoretically) and 0.65 (experimentally). Figure 4.11 shows an intensity plot of the different diffraction orders for the 1x15-fan-out. We compare the theoretical and experimental values for (a) non-compensated and (b) compensated fan-outs. The comparison shows a very good aggreement between the theoretical and experimental values for both cases proving the accuracy of the applied model. We observed that the writing spot compensated surface profiles were less than 2π deep. A possible explanation of this effect is that the algorithm keeps the gradients smaller by sacrificing slightly profile depth and therefore efficiency.

For the 2-D case we observed that the efficiencies and the uniformities of the fan-outs could also be improved. The agreement of the improvement between the theoretical and experimental values for the efficiencies and uniformities of the compensated fan-outs is good. Similar as for the 1-D case, we observe an additional offset for the experimental values, which are caused by stage instabilities during the writing procedure. Experimentally we achieved for a 4x4 fan-out an improvement of 3.3% in efficiency compared to the theoretical value of 3.0%. The uniformity improvement was experimentally 0.19 compared to the theoretical value of 0.12.

4.2.4 Conclusions

We implemented an IFT algorithm for the optimization of arbitrary 1-D and 2-D diffractive fan-outs which are compensated for the convolution with the writing beam. Subsequently, we fabricated and characterized 1-D and 2-D fan-out test structures. We found for the 1-D fan-outs that the efficiencies and the uniformities could be improved considerably by the compensation algorithm. Experimentally we achieved up to 14% (80.6% to 94.6%) efficiency improvement and 0.65 (0.82 to 0.17) uniformity improvement for a 1x15-fan-out. We found a very good agreement with the theoretical predictions. For the 2-D case we observed that the uniformities of the fan-outs could be significantly improved, together with a slight efficiency improvement. Experimentally we achieved for a 4x4 fan-out experimentally an improvement of 3.3% (81.4% to 84.7%) in efficiency and 0.19 (0.44 to 0.25) in uniformity.

Chapter 5

Deep optical microstructures

Optical microstructures can principally be divided into two categories, refractive and diffractive. The transition between these two categories, however, is continuous and there is not always a common consensus whether an optical microstructure is diffractive or refractive. With refractive microstructures we mean structures which deviate light based on the law of refraction, while diffractive microstructures are characterized by a lateral periodicity, and are mainly governed by the laws of diffraction. It is remarkable that as little as a few grating periods are sufficient to make an optical microstructure diffractive.[36] The deep, optical microstructures in the first two sections of this chapter are refractive, while the last two sections deal with diffractive microstructures.

In this chapter we present results which are related to deep optical microstructures, i.e. elements having a phase depth of more than 2π. In Section 5.1 we introduce a method to calculate three-dimensional surface profiles of resist reflow microstructures with arbitrary border geometry, which takes into account surface tension and gravity. Reflow microstructures in micro-optical applications have typically dimensions of a few tenths up to a few hundred micrometers and are deep in the above sense. Micro-optical elements which combine the fan-out and focusing function are presented in Section 5.2. The monolithic elements were realized by using two different concepts: either the two functions are implemented on the opposite sides of one substrate, or the fan-out function is superimposed on the convex surface of the refractive microlens. In Section 5.3 we present color fan-out elements which are able to separate the different colors of the visible spectrum into the three central diffraction orders of a grating. To obtain this functionality the multilevel gratings need to be more than 2π deep. Theoretical results for diffractive optical elements which have a nearly constant, high diffraction efficiency for a large spectral bandwidth in the visible region are shown in

Section 5.4. These elements need to be very deep in order to achieve the desired functionality because of the given material constraints.

5.1 Surface profile modelling for reflow microstructures

5.1.1 Introduction

Refractive microlenses are used in various applications such as miniaturized, chemical detection systems,[65] Multiple Projection Lithography,[99] and confocal microscopy.[22] A common and well known method to fabricate such refractive microlenses is the melting resist technology as described in Section 2.4. The fabrication process, as illustrated in Fig. 2.5 of Section 2.4, is dominated by experimental experience. Little work so far has been dedicated to a theoretical investigation and analysis of the surface profiles in terms of the basic underlying physical quantities, especially for arbitrary microlens geometries. In the work of Sheridan et al. [83] the modelling of melted spherical microlens shapes is done with a heuristic approach, while in the work of Erdmann [23] the restrictions concerned either the geometry of the structures, approximations for small radii of curvature, or the exclusion of gravity. For spherical or elliptical microlenses without gravitational influence, the theoretical profile forms can be determined analytically, while for arbitrary microlens geometries the surface profiles have to be evaluated with numerical methods. Examples for this kind of more complicated profile forms are cylindrical microlenses intersecting under 90°, which results in a microlens corner structure. Such structures can possibly be used in smart mask lithography where micro-optical elements serve to print simple patterns into photoresist.[100]

Here we present a finite element method to calculate 3-D surface profiles of microlenses with arbitrary geometry under the influence of surface tension and gravity. We demonstrate that for certain parameter combinations gravity can have an advantageous influence on the surface profile form of microlenses compared to the surface profile without gravitational influence. We give a simple scaling law to estimate the influence of gravity on the surface profiles of melting resist microlenses. We compare theoretical profile forms with measured profiles of fabricated structures to demonstrate the applicability of this finite element method. For the example of cylindrical microlenses intersecting under 90°, we show how theoretical predictions for the surface profiles can be used to improve the design of smart mask structures.[76, 75]

5.1.2 The theoretical model

The model to calculate the surface profiles of melting resist microlenses is based on the assumption that at a certain point during the fabrication process the resist is a liquid with a defined surface tension and that a generalized minimum surface is formed under the additional influence of gravity. For a complete description of the problem one has to specify the geometry of the resist borders, the resist height, the surface tension and mass density of the liquid photoresist, and the gravity constant. Hereby we assume that, during the melting process, the borders of the resist structures remain fixed, which is experimentally well justified, at least for the fabrication process we used. If one further assumes that the volume is conserved during the melting process, the problem is specified and the solution is completely determined. In order to take into account resist solvent evaporation during the melting process, the fraction of evaporated solvent or the maximum microlens height after the melting process could be used as additional parameter.

In the following, we present the basic equations for the generalized minimum surface problem. The equation which describes the surface profile of a liquid with a surface tension σ and mass density ρ in an external potential U is given through [9]

$$\sigma\left(\frac{1}{R_1(x,y)} + \frac{1}{R_2(x,y)}\right) + \rho U(x,y,z) + \kappa = 0. \tag{5.1}$$

$R_1(x,y)$ and $R_2(x,y)$ are the two principal radii of curvature, κ is a constant and x and y are Cartesian coordinates. In terms of the surface profile $z(x,y)$ we get for the radii of curvature

$$\left(\frac{1}{R_1(x,y)} + \frac{1}{R_2(x,y)}\right) = div\left(\frac{1}{\sqrt{1+\mid grad\ z(x,y)\mid^2}} grad\ z(x,y)\right). \tag{5.2}$$

The influence of gravity is described by the external potential $U = -gz$ where g is the gravity constant. From Eq. (5.1) we get finally for the surface profile $z(x,y)$ the partial differential equation

$$div\left(\frac{1}{\sqrt{1+\mid grad\ z(x,y)\mid^2}} grad\ z(x,y)\right) - \frac{\rho g}{\sigma} z(x,y) + \frac{\kappa}{\sigma} = 0. \tag{5.3}$$

The geometry is illustrated in Fig. 5.1. The coefficient $\rho g/\sigma$ defines a typical length scale $L_c = \sqrt{\sigma/\rho g}$, which is called capillary length. In the following we replace the constant $\rho g/\sigma$ by a and κ/σ by b. Therefore, Eq. (5.3) takes the form

$$div\left(\frac{1}{\sqrt{1+\mid grad\ z(x,y)\mid^2}} grad\ z(x,y)\right) - a z(x,y) + b = 0. \tag{5.4}$$

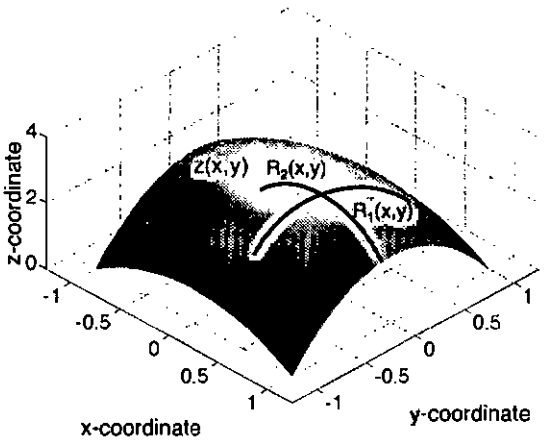

Figure 5.1: Arbitrary surface $z(x, y)$ with the two principal radii of curvature $R_1(x, y)$ and $R_2(x, y)$.

This elliptic partial differential equation was solved with a finite element method, as implemented in the partial differential equation toolbox in MATLAB™.[96] First, the boundary of the microlens has to be specified. This boundary corresponds to the boundary of the resist cylinders before the melting process. There are no restrictions concerning the geometry of the boundary. Afterwards a meshgrid with an appropriate resolution has to be defined over the area of interest, the interior of the microlens boundaries. An appropriate resolution of the grid can always be found by using a set of meshgrids with increasing resolution while controlling the convergence of the obtained solutions. Subsequently, the boundary conditions have to be defined. For the standard case it is rather obvious to use Dirichlet boundary conditions, where the value of the surface profile height z is specified on the boundary. After the melting process the surface profile height is zero on the boundary, therefore the Dirichlet boundary condition becomes

$$z(s(x, y)) \equiv 0, \tag{5.5}$$

where $s(x, y)$ describes the boundary of the microlens. It can be useful for certain special cases to use other boundary conditions, like Neumann boundary conditions, where the derivative of the profile height z is given on the boundary, or mixed boundary conditions, where a combination of z and the derivative of z is specified on the boundary. The parameters σ, ρ, and κ, or

equivalently a and b, have to be defined. σ and ρ are material constants which depend on the photoresist used for the fabrication of the microlenses, and the constant κ has to be determined with the help of an additional parameter, like volume or maximum height of the final surface profile. For the calculations in Subsection 5.1.3, we chose the parameter b so that the resist volume was conserved during the melting process. In Subsections 5.1.4 and 5.1.5 the parameter b was determined so that the experimental and theoretical maximum profile heights agreed. Typical values for mass density and surface tension of photoresist are $\rho = 1000\,kg/m^3$ and $\sigma = 2.5-5\cdot 10^{-2}\,N/m$, respectively.[23, 2] Therefore, a typical value for the parameter a is about $2\cdot 10^{-7}\,\mu m^{-2}$, which corresponds to a typical length scale of $L_c \approx 2\,mm$.

By rewriting Eq. (5.1) with the parameters a and b, we obtain

$$\left(\frac{1}{R_1(x,y)} + \frac{1}{R_2(x,y)}\right) - az(x,y) + b = 0. \tag{5.6}$$

If the linear dimensions and the surface profile height are scaled with an arbitrary dimensionless parameter β we get

$$x' = \beta x, \tag{5.7}$$

$$y' = \beta y, \tag{5.8}$$

$$z'(x',y') = \beta z(x,y), \tag{5.9}$$

and the radii of curvature scale accordingly as

$$R_i' = \beta R_i \quad , i = 1,2. \tag{5.10}$$

As a consequence, Eq. (5.6) remains invariant if at the same time the parameters a and b are scaled according to

$$a' = \frac{a}{\beta^2}, \tag{5.11}$$

$$b' = \frac{b}{\beta}. \tag{5.12}$$

The scaling property of Eq. (5.6) and the parameters a and b is useful for the estimation of the gravity influence on the surface profiles of melting resist microlenses. It will be employed in Subsection 5.1.3.

5.1.3 Influence of gravity on the surface profiles of reflow microlenses

We have investigated the influence of the direction and strength of gravity on the surface profile form of spherical microlenses. The parameters ρ, g,

and σ appear in Eq. (5.4) in the combined form of the parameter $a = \rho g/\sigma$. For fixed values of mass density ρ and surface tension σ, the variation of the parameter a corresponds to a variation of gravity. We have to distinguish between two different cases. In the first case, gravity points from the substrate to the microlens surface (hanging microlenses), corresponding to $a < 0$. In the other case, gravity points from the microlens surface to the substrate (lying microlenses), corresponding to $a > 0$. The two different configurations are displayed in Fig. 5.2. We have calculated for spherical microlenses with

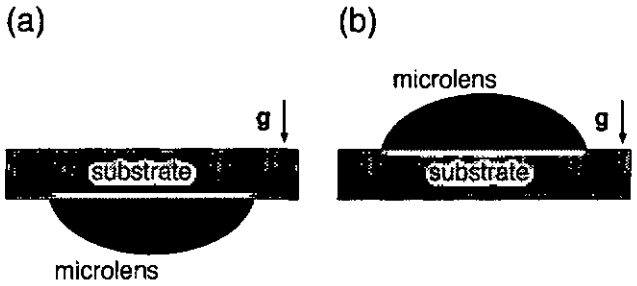

Figure 5.2: Gravity g acting on the melting photoresist during microlens formation: (a) hanging microlenses ($a < 0$), (b) lying microlenses ($a > 0$).

a diameter of $100\,\mu m$ and a typical resist cylinder height of $9\,\mu m$ the surface profile forms as a function of the parameter a. Subsequently, we have calculated the corresponding Zernike polynoms of the surface and analyzed the profile forms with a commercial raytrace program (Raytrace^{TM} 6.1). We have evaluated the focal spot size for the microlenses with a refractive index of $n = 1.5$, illuminated with a plane wave from the convex side. The focal spot was defined as the point of least confusion. The results of the simulations are shown in Fig. 5.3. A significant influence on the spot size can be observed for parameter values $|a| > 2 \cdot 10^{-5}\,\mu m^{-2}$ in both cases of the direction of gravity. This value of the parameter a corresponds to a capillary length of $L_c \approx 200\,\mu m$ which is on the order of the microlens diameter of $100\,\mu m$. For parameter values $|a| > 5 \cdot 10^{-4}\,\mu m^{-2}$ the spot size changes dramatically. The behaviour of the spot size is quite different for the two different directions of gravity. While for lying microlenses the focal spot increases continuously, for hanging microlenses a smaller focal spot size is possible. This is due to the reduction of spherical aberration by thickening the center of the lens. The smallest spot is achieved for $|a| \approx 3 \cdot 10^{-4}\,\mu m^{-2}$. The focal spot is 25%

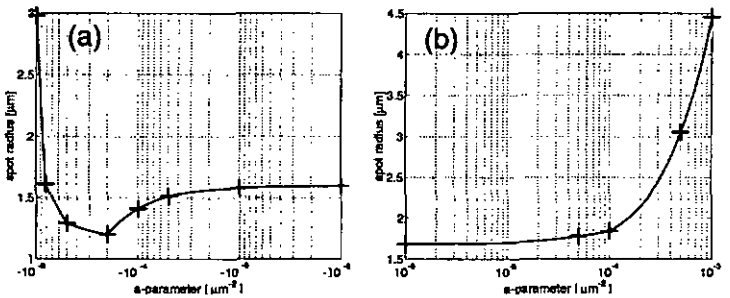

Figure 5.3: Focal spot size as a function of the parameter $a = \rho g/\sigma$. (a) hanging microlens ($a < 0$), (b) lying microlens ($a > 0$). (Note that, because of the logarithmic scale, the parameter a is not displayed for the case of zero gravity.)

smaller than the spot size of a comparable microlens without gravitational influence for this configuration.

The scaling law introduced in Subsection 5.1.2 predicts that if the length scales for a given microlens geometry are changed by one order of magnitude then the parameter $a = \rho g/\sigma$ has to be scaled by two orders of magnitude to reproduce an identical surface profile. As shown above, gravity starts to have an influence on the surface profile for $|a| > 2 \cdot 10^{-5}\,\mu m^{-2}$ for microlenses with diameters of $100\,\mu m$. Formulated as inequality the relationship

$$\phi_l > \sqrt{\frac{0.2}{|a|}} \tag{5.13}$$

specifies a lower limit ϕ_l for the microlens diameter where gravitation has a significant influence. Therefore, one can conclude that, assuming a typical parameter value of $a \approx 2 \cdot 10^{-7}\,\mu m^{-2}$ for standard photoresist, gravitation will start to have a significant influence on the profile form for microlenses with diameters larger than about $1000\,\mu m$. Equivalently, if the parameter a could be changed by two orders of magnitude, for example by using other materials or by increasing gravity with a centrifuge, the influence on the surface profile would become significant for diameters larger than about $100\,\mu m$. Since the scaling law is valid in general, the conclusion about the influence of gravity can be extended to arbitrary microlens structures, when typical radii of curvature are comparable with the radii of curvature of the investigated spherical microlenses. For microlens structures with other typical radii

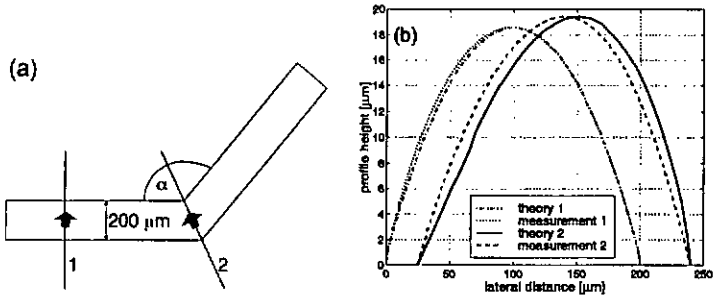

Figure 5.4: Two cylindrical microlenses intersecting under an angle of $\alpha = 135°$: (a) geometrical configuration, (b) theoretical and experimental profile curves for the cross sections 1 and 2 indicated in Fig. 5.4(a).

of curvature, the critical value of the parameter a for the onset of gravity influence can be determined by the scaling laws given in Eqs. (5.7) to (5.12).

5.1.4 Test of the theoretical model

We fabricated various test structures to verify the described finite element modelling for microlens surface profiles with arbitrary geometry. The different geometries and the comparison of the theoretical and the experimental results are shown in Figs. 5.4 to 5.6. The microlenses were fabricated following the process described in reference [65]. We used the photoresist AZ 4562 from Hoechst. We always calculated 3-D surface profiles and took cross sections for the comparison with the measured curves. For the investigated microlenses the influence of gravity was negligible, therefore all profile forms were calculated with $a = 0$. All experimental curves were measured with a profilometer (Tencor Instruments). The exact positions and directions of the measured curves were controlled with a microscope that allowed to view the profilometer tip and the microstructures to be measured.

Figure 5.4(a) shows a microlens structure with two cylindrical microlenses intersecting under an angle of 135°. The comparison of the theoretical and experimental surface profiles for the cross sections 1 and 2, as indicated in Fig. 5.4(a), is shown in Fig. 5.4(b). The agreement between calculated and measured profile forms is very good for the cross section 1. For cross section 2 the maximum height and the general profile form is well reproduced, while the lateral position of the maximum height is slightly displaced.

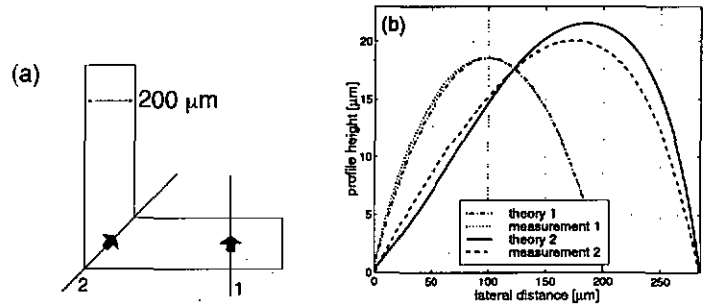

Figure 5.5: Two cylindrical microlenses intersecting under an angle of $\alpha = 90°$: (a) geometrical configuration, (b) theoretical and experimental profile curves for the cross sections 1 and 2 indicated in Fig. 5.5(a).

5.1.5 Application of the model to smart mask structures

It is desireable for certain smart mask applications to have connected, cylindrical microlenses which form a 90° angle. We fabricated two different structures of connected cylindrical microlenses under an angle of 90°, shown in Figs. 5.5 and 5.6. In the layout of Fig. 5.5, the microlenses are directly connected, forming a sharp corner. In the layout of Fig. 5.6, the 90° corner is rounded, so that the microlens has a constant width. For these two structures we calculated and measured the profile forms and found again an experimental verification of the theoretical results, as expected. The cross section 1 in Fig. 5.5 yields the same result as for the structure with $\alpha = 135°$, because it corresponds to the same cylindrical microlens. The agreement between calculated and measured data for cross sections 2 is satisfactory. However, the absolute profile height is slightly underestimated and the theoretical profile shows a slight deviation from the measured one. For the two cross sections displayed in Fig. 5.6, we found an excellent agreement between theoretical and experimental profiles for both cross sections. The "constant width" structure from Fig. 5.6, with a difference between interior and exterior radius of curvature equal to the width of the structure, has the expected property that the microlens height is constant and that the cross sectional profile is identical for the whole microlens. The focal line is therefore produced in the same plane along the whole structure, which was confirmed by intensity measurements. Consequently, this structure would be the most appropriate for smart mask applications, where patterns in the focal plane have

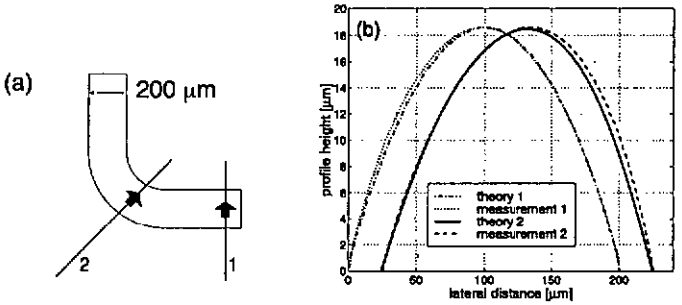

Figure 5.6: Improved corner structure for two microlenses with a constant width design: (a) geometrical configuration, (b) theoretical and experimental profile curves for the cross sections 1 and 2 indicated in Fig. 5.6(a).

to be printed into resist. The fact that the agreement between theoretical and experimental surface profiles was better for smooth structures than for structures having sharp corners was also confirmed by other experiments.

5.1.6 Conclusions

We have presented a finite element method to determine theoretically the 3-D surface profiles of microlenses fabricated by melting resist technology for arbitrary microlens border geometries. For spherical microlenses, the influence of gravity on the profile form was calculated and the optical properties of the resulting profile forms were analyzed with a commercial raytrace program. We found that for hanging microlenses a better focal spot can be achieved than for lying microlenses. With the help of a simple scaling law, we derived a rule of thumb to decide when gravity has a non-negligible influence on the surface profiles of microlenses. We compared theoretical and experimental results for the surface profiles of different structures and found good agreement. For cylindrical microlenses intersecting under 90°, we demonstrated the utility of this modelling method to design non-standard microlenses for smart mask applications.

5.2 Miniaturized, focusing fan–out elements

5.2.1 Introductiou

Fan–out phase gratings are micro-optical elements which split an incoming beam into an array of light beams with equal power. The diffracted beams are then focused by a Fourier transform lens. These elements are used, for example, in optical interconnects, in multidetector systems, and in parallel optical processing.[65, 5, 101] We present different concepts for the fabrication of hybrid elements which combine the fan–out and the focusing function. The fan–out function is diffractive and for the focusing function we use refractive microlenses. The combination of these two optical functions results in monolithic elements with miniaturized dimensions and therefore with a high potential for applications in optical microsystems. To achieve this functionality, we used two different designs and different fabrication technologies, namely injection moulding in polycarbonate, double-sided photolithography with subsequent etching in fused silica, and direct laser writing in photoresist. Single elements, as well as large arrays of elements, have been fabricated.[78, 77, 37]

5.2.2 Design considerations

The combination of the fan–out and the focusing function can be done in two conceptually different ways. Either the two functions are implemented on the two opposite sides of one substrate (see Fig. 5.7(a)), or the fan–out function is superimposed on the focusing function of a plano-convex microlens (see Fig. 5.7(b)). The first concept was used for the elements fabricated by injec-

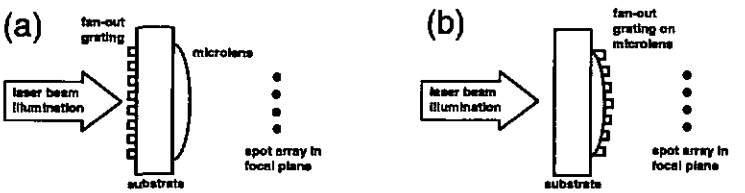

Figure 5.7: Schematic drawing of the two different concepts for hybrid elements: (a) the fan–out structure is on the backside of the microlens, (b) the fan–out structure is on top of the refractive surface.

tion moulding in polycarbonate and by double-sided photolithography with subsequent transfer into fused silica. The second possibility was used for

elements fabricated by direct laser writing in photoresist. In case (a), the diffraction orders are generated by the grating and propagate parallel to the optical axis after the lens, when the grating plane is in the back focal plane of the lens. For case (b), the diffraction orders are divergent after the element with respect to the optical axis, because the fan-out grating is on top of the curved surface of the lens. For an application, where the spots have to be aligned relative to a reference, for example a detector, the properties of the two concepts in terms of alignment tolerances are different. With concept (a), the longitudinal position of element and detector is uncritical. Concept (b) can be advantageous for a system with lateral alignment errors between spots and detector, because these errors can be compensated by longitudinal adjustment of the element relative to the detector.

5.2.3 Fabrication of the elements

For the fabrication of the hybrid elements, we used three different technologies. Injection moulding in polycarbonate, double-sided photolithography with subsequent transfer into fused silica, and direct laser writing in photoresist.

Injection moulding in polycarbonate: The plano-convex microlens originals in photoresist were fabricated by photolithography and a subsequent melting process, as described in Section 2.4. The diffractive fan-out gratings in photoresist were obtained by standard binary mask lithography on another substrate. Two masters were made from the photoresist originals by electroplating. One for the diffractive fan-out structures and the other for the refractive microlenses. With these masters, double-sided replications in polycarbonate were fabricated by injection moulding. The process was executed at the IMM in Mainz. This technology is well suited for low cost mass production.

Double-sided photolithography with subsequent transfer into fused silica: The diffractive fan-out structures and the refractive microlenses were fabricated by photolithography into photoresist on both sides of a fused silica wafer. Subsequently, these photoresist elements have been transferred into fused silica by reactive ion etching (RIE) in two independent etch steps. The photoresist microlenses with a height of about $60\,\mu m$ resulted in microlenses with a height of $40\,\mu m$ after the transfer into fused silica.

Direct laser writing in photoresist: Plano-convex photoresist microlenses, fabricated again by photolithography and subsequent melting, were spin-coated with an additional photoresist layer. Afterwards, a continuous relief fan-out phase grating was directly written in the resist with the laser writer at CSEM in Zurich.[30, 29] This technology can be used for rapid prototyp-

ing of photoresist elements. A possible replication of these elements would have the advantage that only one structured surface needs to be replicated.

5.2.4 Comparison of the fabrication methods

Each of the three different technologies which were used for the fabrication of the hybrid focusing fan-out elements has its advantages and limitations. The optimum technology depends on the specifications imposed by the application for which the element will be used later. Besides, the quality-cost compromise that can be tolerated is of importance. Double-sided photolithography with subsequent transfer into fused silica produced the elements with the best overall performance. However, compared to the other two fabrication technologies, it is relatively expensive, and the transfer of deep photoresist microlenses into fused silica is not yet a standard process. The injection moulding technology is well adapted for the production of a large number of elements at low cost with satisfactory quality. The double-sided photolithography provides an accurate alignment of the two optical functions of about 1 μm, whereas the injection moulding process allows an alignment with a tolerance of about 20 μm, limited by the mechanical positioning of the two masters during the process. The accuracy of the alignment was not critical for our periodic fan-out structures. However, for a non-periodic structure, for example a diffractive aspheric correction of the microlenses, the alignment accuracy will become important. An advantage of the laser writing technology compared to the other two technologies is that a prototyp in photoresist can be fabricated relatively fast. Subsequently, a Nickel shim can be fabricated by electroforming from the photoresist original and elements can be replicated by hot embossing.[28] The advantage of this approach is that the optical functions are on one single surface and therefore only one structured surface needs to be replicated. A disadvantage of the laser writing technique is, that for the performance of the element the homogenity of the additional photoresist layer is quite critical. The homogeneous deposition of this additional resist layer on the curved surfaces of the convex microlenses is not trivial.

5.2.5 Characterization

Injection moulding in polycarbonate

The original is a binary Dammann grating in photoresist, which generates 4x4 equal diffraction orders. The grating period is 64 μm with a minimum feature size of 1 μm. The calculated binary phase and a SEM micrograph

of an element fabricated by injection moulding is shown in Fig. 5.8. We measured a diffraction efficiency of 73% and a uniformity error ($[Imax - Imin]/[Imax + Imin]$) of 2.6% for the photoresist original. 1% of the incom-

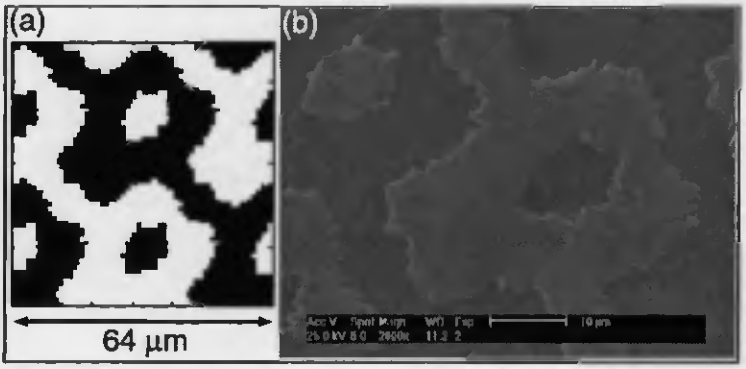

Figure 5.8: (a) calculated phase element, and (b) SEM image of fabricated binary fan-out structure, which generates a 4x4 equal intensity fan-out. The SEM micrograph shows an element which was fabricated by injection moulding in polycarbonate.

ing light was found in the zeroth order. The theoretical values are 76% for the efficiency, 0.7% for the uniformity and 0% in the zeroth order. The replicated fan-out elements had an efficiency of typically 62% with a uniformity error of 20%. 6% of the light was in the zeroth order. Figure 5.9 shows the measured intensity distribution in the focal plane of a focusing fan-out element in polycarbonate. The element has a diameter of 990 μm. The fan-out performance of the separate fan-out and the monolithic hybrid elements were comparable. The pitch of the replicated microlens arrays, measured with a knife edge, was reproduced to better than 1% between two neighbouring microlenses. The accumulated relative pitch error over 6 microlenses (990 μm diameter, gap 10 μm) and over 10 microlenses (350 μm diameter, gap 5 μm) was in both cases 0.4%. We characterized the surface profile of the replicated microlenses with a Twyman-Green interferometer. The surface deviation from a sphere was typically 0.2 λ (rms) for lenses with 610 μm diameter, and 0.35 λ (rms) for 990 μm diameter. The measured surface deviation of a microlens with 990 μm diameter is shown in Fig. 5.10. Subsequently, we performed a ray-trace analysis using the measured surface profile. The original photoresist microlenses with a diameter of 610 μm which were used for the fabrication

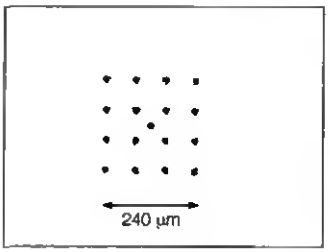

Figure 5.9: Intensity distribution of miniaturized focusing fan out element in the focal plane. The element was fabricated by injection moulding. The diameter of the microlens is 990 μm and the grating period of the fan-out is 64 μm (λ = 632.8 nm, NA = 0.12).

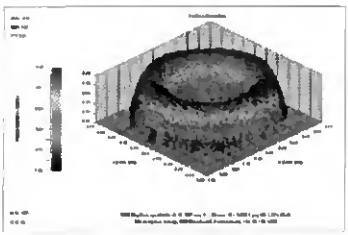

Figure 5.10: Surface deviation from a sphere for a replicated microlens (990 μm diameter), measured with a Twyman Green interferometer. The rms value is 0.3 λ.

of the master had a surface deviation of 0.11 λ (rms). The intensity distribution in the focal plane (4 mm behind the microlens) of a hybrid element with 990 μm diameter is shown in Fig. 5.9. The measured spot size is about 18 μm (NA=0.12), compared to about 17 μm obtained from raytrace simulation. The spot size is mainly determined by the spherical aberration of the microlens. Concerning unwanted straylight between the diffraction orders, the elements with larger diameters performed better.

Double sided photolithography and subsequent transfer in fused silica

We used a binary 4x4 fan out grating in photoresist, which had the same parameters as the photoresist originals for the injection moulding process: 64 μm grating period, a measured efficiency of 73%, and a uniformity error of 2.6%, with 1% in the zeroth order. The quality of the refractive photoresist microlenses was characterized with a Twyman Green interferometer. A typical surface deviation from a sphere of about 0.1 λ (rms) was found.

After the first etch step before the transfer of the microlenses, the fan out was characterized. The effciency was 75% (theoretically 76%), the uniformity error was 7% (theoretically 0.7%) and 0.5% of the light was in the zeroth order (theoretically 0%). For the combined elements with diameters of 990

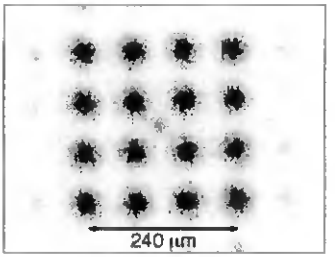

Figure 5.11: Intensity distribution in the focal plane of a miniaturized focusing fan out element. The element is in fused silica, the diameter of the microlens is $610\,\mu m$ and the grating period of the fan-out is $64\,\mu m$ ($\lambda = 632.8\,nm$, NA = 0.17).

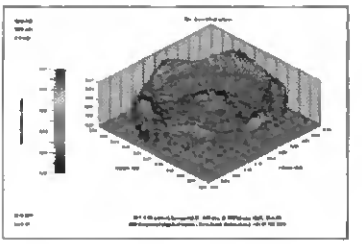

Figure 5.12: Surface deviation from a sphere for a microlens with $610\,\mu m$ diameter, etched in fused silica, measured with a Twyman Green interferometer. The rms value is $0.08\,\lambda$.

and $610\,\mu m$, the uniformity error was the same as for the separate fan out elements. For the elements with a diameter of $350\,\mu m$, the uniformity error and straylight between the diffraction orders increased. Figure 5.11 shows the measured intensity distribution in the focal plane of a focusing fan out element in fused silica with a diameter of $660\,\mu m$. The measured surface deviation from a sphere for a microlens with $660\,\mu m$ diameter is shown in Fig. 5.12. The rms value for the surface deviation is $0.08\,\lambda$.

A microscopic image of a fosusing fan out element, which was fabricated by double sided photolithography with subsequent transfer into fused silica as desribed in Subsection 5.2.3, is shown in Fig. 5.13. The image shows a hexagonally packed refractive microlens array on one side of the substrate, and a binary fan out structure on the other. This image was published as "After Image" in the November 1998 issue of *Optics and Photonics News*.

Direct laser writing in photoresist

An additional layer of photoresist was spincoated onto the photoresist microlenses. The additional layer had a thickness of about 2 to $3\,\mu m$. The photoresist microlenses were characterized with a Twyman Green interferometer before and after the deposition of the additional photoresist layer. Subsequently, a continuous relief 5x5 fan out phase grating was written in the photoresist with the laser writer. We used a reduced writing speed of

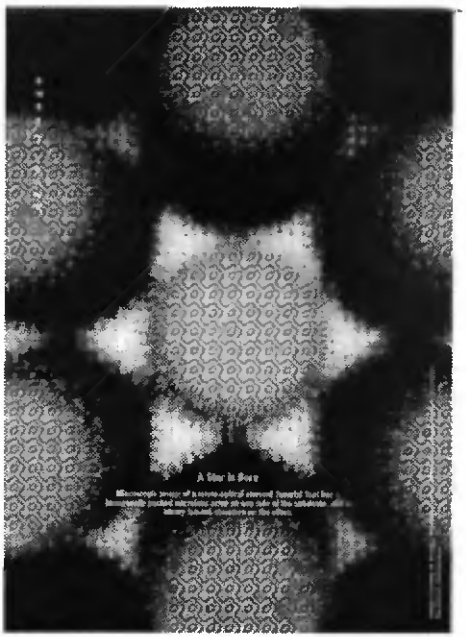

Figure 5.13: Microscopic image of a fosusing fan out element (fused silica) with a hexagonally packed refractive microlens array on one side of the substrate and a binary fan-out structure on the other. (Published as "After Image" in the November 1998 issue of *Optics and Photonics News.)*

$v = 10\,\mu m/s$ and a spot size of $1.3\,\mu m$ (FWHM). The grating period of the fan-out was $51.2\,\mu m$. Since it was difficult to achieve a homogeneous layer of photoresist on the microlenses with the spinning procedure, the fan outs showed a relatively large uniformity error. Figure 5.14 shows the measured intensity distribution in the focal plane of a focusing fan out element with a diameter of $990\,\mu m$ which generates 5x5 diffraction orders.

5.2.6 Conclusions

We have presented miniaturized focusing fan out elements. The new micro optical elements were fabricated by different technologies: double sided injection moulding in polycarbonate, double sided photolithography with sub-

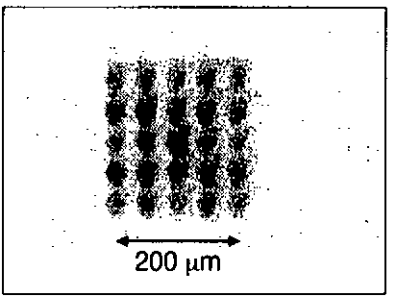

Figure 5.14: Intensity distribution of a focusing fan-out element in the focal plane. The element was fabricated by direct laser writing in photoresist on photoresist microlenses. The diameter of the microlens is 990 μm and the grating period of the fan-out is 51.2 μm ($\lambda = 632.8\,nm$, NA = 0.14).

sequent etching in fused silica, and direct laser writing in photoresist. Two different concepts were used for the fabrication: either the two optical functions are implemented on the opposite sides of one substrate, or the fan-out function is superimposed on the convex surface of the microlens. We have demonstrated that the three different technologies can be successfully employed for the fabrication of miniaturized focusing fan-out elements, while each technology has certain advantages and limitations. The small size of the combined elements makes it necessary to use fan-out gratings with small grating periods. This causes a relatively large uniformity error for the fan-out elements compared to values published in the literature, which are usually obtained for fan-outs with significantly larger grating periods. The characterization showed that the quality and overall performance of the elements fabricated by injection moulding is satisfactory. The advantage of this technology is the possibility of mass production at low cost. The focusing and the fan-out functions on the two opposite sides are aligned within about 20 μm. The fused silica elements showed the best optical performance. However, the transfer of deep photoresist microlenses into fused silica is not a standard process. The direct laser writing technique has the advantage that a prototype can be fabricated relatively fast. For a replication of the hybrid elements only one surface has to be replicated and therefore no alignment is necessary. Critical for the performance of the elements is the homogenity of the additional photoresist layer.

5.3 Color fan–out elements

DOEs can be used to discriminate the colors in the spectrum of incident light. The simplest approach is to use the dispersion inherent to diffraction gratings. However, it is also possible to utilize a design based on the idea of Dammann,[14, 15] which provides more degrees of freedom for the design of the intensity distributions of the colors. This design principle utilizes a deep multilevel grating, which can be thought of as three different blazed gratings, each blazed for a different diffraction order. There exist also other approaches to achieve color separation using arbitrary phase elements. The non–periodic phase distributions of these elements are optimized by a modified IFT–algorithm.[57] The algorithm optimizes the phase element until a best compromise is found to achieve the desired color separation and position for all the specified discrete wavelengths. This approach is adapted when a few discrete wavelengths have to be separated and placed in predefined locations, eventually with an additional focusing function. Applications like (de)multiplexer, router or couplers may be possible in WDM communication systems.[57] The deep multilevel approach, however, is rather to separate colors in a large band spectrum. A possible application for such multilevel gratings is color separated imaging, where the different colors have to be projected onto separate detectors. A particularity of the multilevel approach is that the spectral curves obtained with the 4–level gratings are very similar to the required sensitivity curves of pickup devices for color reproduction by TV.[14]

5.3.1 Principle and limitations

The color–fan–out element projects the different colors of the visible spectrum into the three central diffraction orders -1, 0, and +1. A possible configuration utilizing this color separating gratings, using an additional Fourier lens, is shown in Fig. 5.15(a). The element acts as a left blazed grating for the blue, as a right blazed grating for the red, and like a non–structured surface for the green color. That means that it has to fulfill for three different wavelengths seemingly controversial conditions. The three different optical functions for the three different wavelengths are schematically indicated in Fig. 5.15(b). The solution was proposed first by Dammann [14] and uses the so–called overphasing principle for periodic multilevel gratings. The overphasing priniciple is based on two facts. First, that for a given surface profile the added phase is proportional to $1/\lambda$ when dispersion of the material is neglected. Second, that a standard 2π multilevel grating, designed for a specific wavelength λ_1 shows the same scalar behaviour as a grating

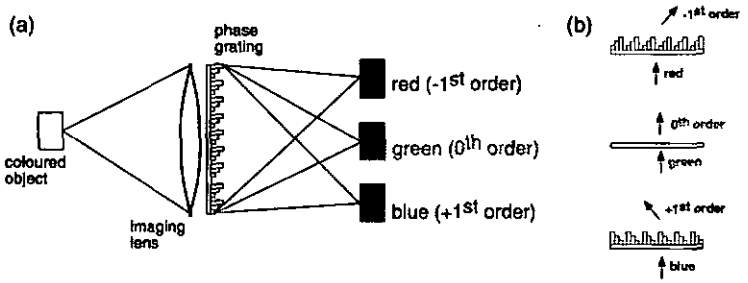

Figure 5.15: The principle of the periodic color separating fan-out elements: (a) color separation into the three central diffraction orders with periodic multilevel gratings based on the overphasing principle; (b) different optical functions for the three different colors of the incident spectrum.

where on each phase level, except the lowest one an, interger multiple of 2π phase for this wavelength is added. This overphased grating acts now for a certain wavelength λ_2 like a flat surface relief profile when the phase difference between two adjacent levels is a multiple of 2π for the wavelength λ_2. Correspondingly, for a third wavelength λ_3 the overphased grating acts as a blazed grating directed into the opposite direction compared to wavelength λ_1. Such multilevel color fan-out elements are an example where the multilevel profile has a real functionality rather than being just an approximation to an ideal continuous surface profile.

For the design of the multilevel color fan-out element one has basically three design freedoms: the number of phase levels for the grating, the overphasing factor in multiples of 2π per level, and one of the three peak wavelengths which appear in the central diffraction orders. The number of phase levels of the grating has two effects: with increasing number of phase levels the three peak wavelengths get closer and the efficiency in the blazed orders increases. The overphasing factor in multiples of 2π between different levels affects the spectral separation of the three peak wavelengths: a larger overphasing factor causes a narrower spectral separation. Fixing one wavelength determines the spectral location of the other two wavelengths. We designed color fan-out elements with 4 phase levels which operate in the visible spectrum with the three peak wavelengths of $411\,nm$, $514\,nm$, and $666\,nm$. The overphasing factor was 2π for the wavelength of $411\,nm$. In contrast to Dammann's work, where the diffraction gratings had rather large grating periods of around $60\,\mu m$, we focused on small grating periods and therefore large deflection angles. We fabricated 4-level color fan-out

elements with grating periods of 12 and 16μm. Farn et al. [24] published similar results as presented here.

5.3.2 Experimental and theoretical results

The 4-level color fan-out elements were fabricated in fused silica using two photolithographic steps, each followed by a RIE step, as described in Subsection 2.1.1 and Section 2.5. Figures 5.16(a) and (b) show SEM pictures of the fabricated elements. One can observe that the phase steps of the 4-level

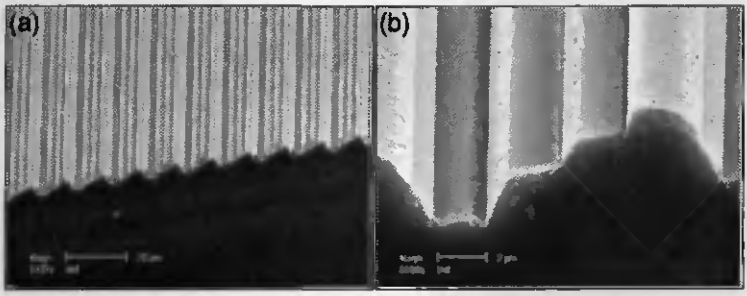

Figure 5.16: SEM pictures of the fabricated 4-level elements in fused silica: (a) displays an overview, (b) an enlarged section displaying one grating period.

grating are not ideal. First, the width of the 4 levels are not equal, because of alignment errors during the second photolithographic step. Second, the phase steps are not vertical because of nonideal illumination during the exposure steps. Because of the small grating period and the corresponding large aspect ratio of the profile, these imperfections have a quite large influence on the optical performance. The elements were characterized by measuring the efficiencies of the three central diffraction orders for TE-polarization at six discrete wavelengths. The theoretical efficiencies were obtained by using exact electromagnetic theory as presented in Subsection 3.2.1. The dispersion of the fused silica is taken into account. Because of the depth of the gratings there are significant differences, of up to 15%, between exact electromagnetic and simple scalar theory, despite the relatively large grating periods. The measured and calculated curves are displayed in Fig. 5.17. Experimentally we achieved about 60% of the theoretical values. The losses are related to the non-ideal grating profile discussed above.

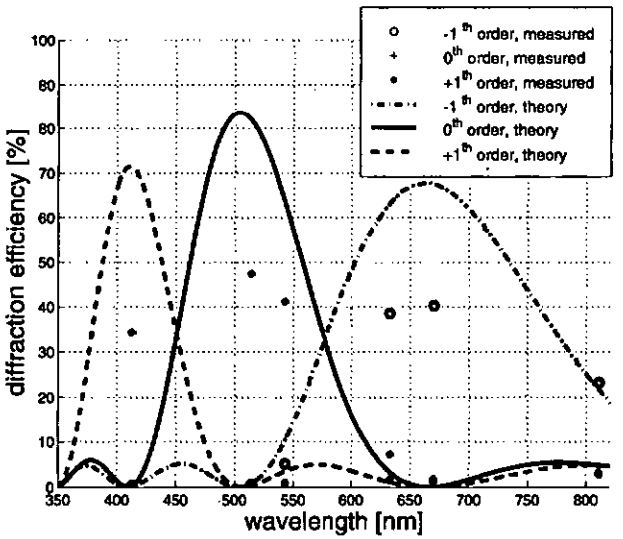

Figure 5.17: Theoretical and experimental efficiencies of the 4–level color fan–out elements (TE–polarization).

Color separating structures can also be used in a reversed manner to synthesize colors by combining different wavelengths. Hereby they are used in a configuration like in Fig. 5.15, but with the wavelengths to be combined incident from the right side from directions corresponding to the -1st, 0th, and +1st diffraction order. We investigated theoretically the possibility of combining wavelengths with overphased multilevel gratings in such a configuration. The diffraction efficiencies as a function of the grating period for a 4–level color separating element in fused silica is shown in Fig. 5.18 for TE– and TM–polarization. These efficiencies are calculated for an arrangement where the three discrete wavelengths 411 nm, 504 nm, and 666 nm are incident from air on the grating with angles corresponding to the -1st, 0th, and +1st diffraction order. Shown is the dependence on the grating period, which corresponds to an angular acceptance curve when the three colors are combined. The design principle of color fan–out elements is based on simple scalar theory. However, for small grating periods deviations from the scalar behaviour are observed, which are relatively large because of the depth of the elements compared to standard diffractive elements with a phase depth

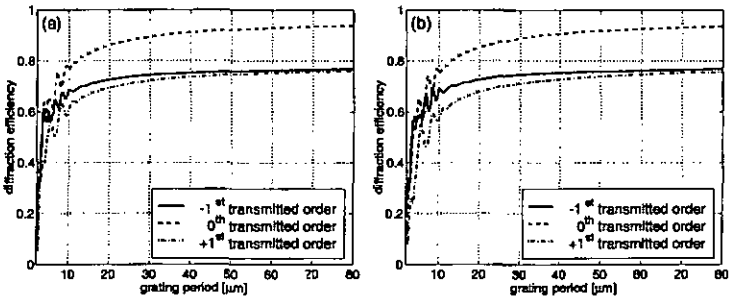

Figure 5.18: Angular acceptance curves for combining the three central wavelengths. (a) TE-polarization, (b) TM-polarization.

of only 2π. In order to quantify the angular acceptance for the combining of the three different wavelengths, we determined the grating period for which the efficiency averaged over the three central diffraction orders drops to 90% of its asymptotic value for a grating period of $50\,\mu m$. This limiting grating period was $14\,\mu m$ for TE-polarization and $15\,\mu m$ for TM-polarization. As expected, the difference between TE- and TM-polarization is quite small, except for very small grating periods.

5.3.3 Conclusions

We designed, fabricated, and characterized deep, color separating, 4-level gratings with relatively small grating periods of $16\,\mu m$. Experimentally we achieved about 60% of the theoretical efficiency predicted by exact electromagnetic theory. We determined theoretically the grating period range for which these color separating gratings show the behaviour as expected from scalar theory, when used for combining wavelengths to synthesize colors.

5.4 Gratings with wavelength independent diffraction efficiency

5.4.1 Introduction

Conventional DOEs reach their maximum efficiency only for the design wavelength while the efficiency is lower for other wavelengths. This is shown for example by the dash-dotted line in Fig. 5.21 for a standard 2π deep

blazed grating. This fundamental drawback limits the field of application for DOEs. A typical example is chromatic aberration correction in hybrid optical systems, where DOEs are used over a large spectral bandwidth, but the maximum efficiency is only achieved for the design wavelength. This basic drawback can be overcome. In order to compensate the wavelength dependence of the phase for a given spectrum, material combinations can be used, which take advantage of the dispersion,[17] or an additional interface can be introduced in the diffractive structure. Using common materials, deep diffractive structures are required. We concentrated on three concepts for such achromatized, diffractive optical elements (A-DOEs) and analyzed them with different models. We determined the range of use of these structures, evaluated the fabrication tolerances, and analyzed the accuracy of the applied models.[81, 102]

5.4.2 Concepts

We investigated three concepts for the realization of A-DOEs, which are displayed schematically in Fig. 5.19. Figure 5.19(a) shows the concept using two

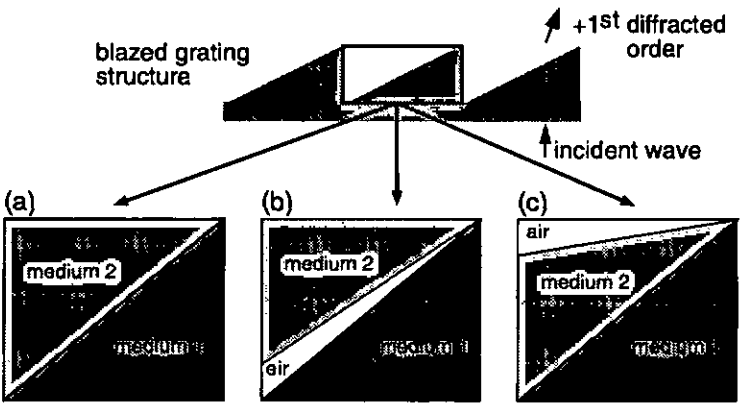

Figure 5.19: Concepts for A-DOEs: two media structure (a), structure with interior (b) and exterior (c) air gap: The parts (a) to (c) show one period of the grating enlarged.

materials with appropriate dispersion, e.g. polycarbonate (PC) and BaF52 glass, which fulfill in a good approximation the condition $\lambda/\Delta n(\lambda) = const.$ Such a configuration was first proposed by Ebstein.[17] The refractive indices

as a function of wavelength for PC and BaF52 are shown in Fig. 5.20. One can clearly observe the increasing difference between the two refractive indices as a function of wavelength. For a design wavelength of $\lambda_d = 740\,nm$ the resulting grating depth is $d = 28.3\,\mu m$.

Another approach, which uses a second surface, has an additional degree of freedom. It is therefore not limited by a special material combination, thus allowing a wider choice of fabrication technologies. It can be realized in two different configurations, as shown in Figs. 5.19(b) and (c). The configuration with an air gap between the two media was proposed by Arieli.[1] The consequences and advantages when this air gap is moved to the exterior are shown in Subsection 5.4.3. In order to treat a realistic case which can be fabricated, we used fused silica and PC with an air gap. The total grating depth and the size of the air gap are determined by the condition that for both design wavelengths, λ_1 and λ_2, the phase difference over one grating period is 2π, which leads to

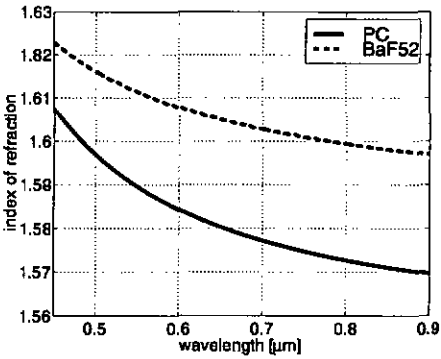

Figure 5.20: Refractive indices as a function of wavelength for PC and BaF52.

$$\lambda_1 = n_{\rm fs}(\lambda_1)d_1 - n_{\rm PC}(\lambda_1)d_2 - n_{\rm air}d_{\rm air} \qquad (5.14)$$

$$\lambda_2 = n_{\rm fs}(\lambda_2)d_1 - n_{\rm PC}(\lambda_2)d_2 - n_{\rm air}d_{\rm air}, \qquad (5.15)$$

where d_1 stands for the depth of the fused silica, d_2 for the PC, and $d_{\rm air}$ for the air gap. These depths are related by $d_1 = d_2 + d_{\rm air}$. $n_{\rm fs}$, $n_{\rm PC}$, and $n_{\rm air}$ stand for the refractive indices of fused silica, PC, and air, respectively. We used as design wavelengths $\lambda_1 = 410\,nm$ and $\lambda_2 = 700\,nm$, which leads to $d_1 = 16.9\,\mu m$ and $d_{\rm air} = 4.78\,\mu m$.

5.4.3 Results and discussion

We used three models for the description of the A-DOEs which are explained in more detail in Chapter 3: simple scalar theory with thin element approximation, an optical path model taking into account polarization dependent

Fresnel losses, and exact electromagnetic theory. All calculations with exact electromagnetic theory were made for TE-polarization. The diffraction efficiencies of the three different approaches as a function of wavelength, calculated with simple scalar theory, are shown in Fig. 5.21 together with the dependence for a conventional 2π deep blazed grating. The two different air gap approaches are equivalent from the point of view of simple scalar theory. However, because of the large depth of the structures, simple scalar theory is often not sufficient to describe these structures accurately. In order to determine the limits of the optical path model, we calculated the diffraction efficiencies for the three concepts as a function of grating period with exact electromagnetic theory and the optical path model. In Fig. 5.22 the diffraction efficiencies of the 2 media A-DOE are shown for various grating periods. Using the materials PC and BaF52, the grating depth of the structure is $28.3\,\mu m$. For the small grating periods ($6\,\mu m$, $8\,\mu m$, and $10\,\mu m$) relatively large differences are observed. For grating periods larger than $25\,\mu m$, we found an agreement of better than 9% when comparing the efficiencies averaged over the spectrum. In Figures 5.23 and 5.24 the diffraction efficiencies of the interior and exterior air gap A-DOEs are shown for various grating periods. The design wavelengths are chosen as $\lambda_1 = 410\,nm$ and $\lambda_2 = 700\,nm$, which yields, following Eqs. (5.14) and (5.15), a grating depth of $16.9\,\mu m$ and an air gap of $4.78\,\mu m$. For both structures, with exterior and interior air gap, we found, for periods larger than $50\,\mu m$, an agreement better than 4% for the averaged efficiencies. The light which is missing in the first order is found in the higher diffraction orders. This effect is significantly increased for the interior air gap structure, where the deflection angles are larger, because of the larger refractive index differences. The effect is illustrated in Fig. 5.25 where for the two air gap structures the phase of the E-field inside the grating structure is plotted for TE-polarization.

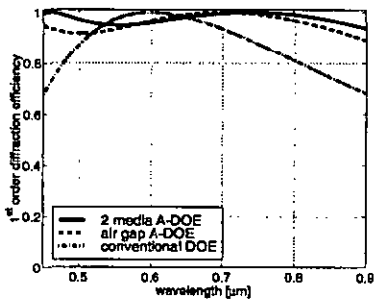

Figure 5.21: Performance of the different approaches for A-DOEs calculated with simple scalar theory. The efficiency of a conventional blazed grating is shown for comparison.

In order to determine the limits of simple scalar theory, we calculated the difference in average efficiency between simple scalar theory and the

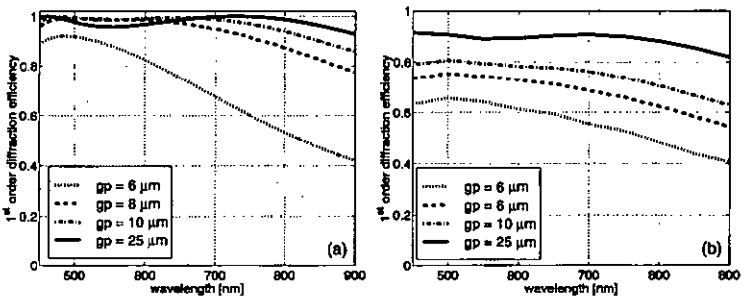

Figure 5.22: Diffraction efficiencies of the 2 media A-DOE for various grating periods. The optical path model (a) and exact electromagnetic theory (b) was applied.

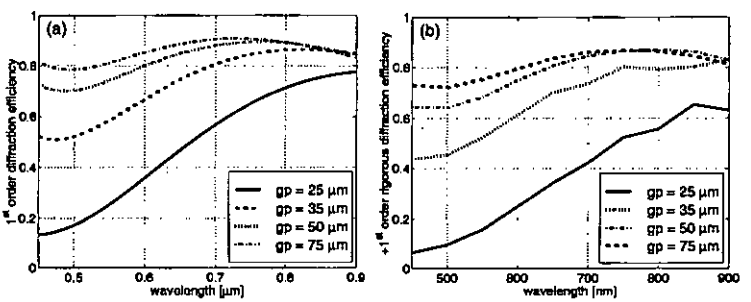

Figure 5.23: A-DOE with interior air gap: (a) diffraction efficiencies calculated with the optical path model, (b) efficiencies calculated with exact electromagnetic theory.

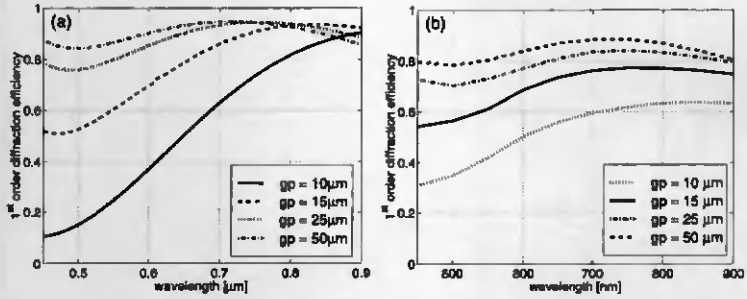

Figure 5.24: A–DOE with exterior air gap: (a) diffraction efficiencies calculated with the optical path model, (b) efficiencies calculated with exact electromagnetic theory.

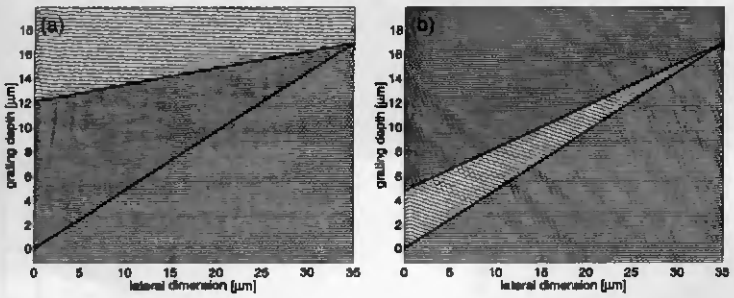

Figure 5.25: Phase of the E–field inside the A–DOE grating structure: (a) exterior air gap, (b) interior air gap. Shown is one grating period

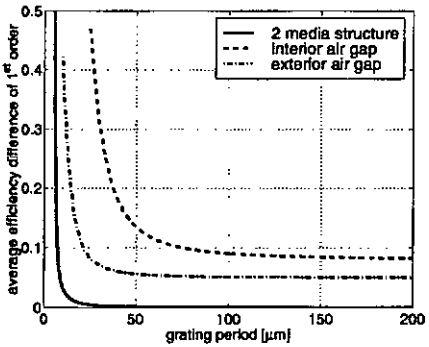

Figure 5.26: Efficiency difference between optical path model and simple scalar theory for the three concepts of A-DOEs.

optical path model for the three concepts as a function of the grating period. The results are summarized in Fig. 5.26. Taking into account Fresnel losses at the interfaces, we found an agreement between the optical path model and simple scalar theory of better than 1 % for grating periods larger than $15\,\mu m$ (2 media), $90\,\mu m$ (interior air gap), and $35\,\mu m$ (exterior air gap). In Figure 5.27 we show a graphical representation of the validity ranges for the different models.

For the realization of deep diffractive structures the fabrication tolerances are of great importance. Therefore, we compared the tolerances of the three concepts using the optical path model, assuming a grating period of $100\,\mu m$. The corresponding efficiencies as a function of height error factor (actual height divided by ideal height) are shown in Fig. 5.28. For the A-DOE, a fabrication would require to realize the two blazed grating structures independently. The fabrication errors are therefore related to the depth of the two blazed gratings. For the A-DOE with the exterior air gap however it would be possible to fabricate the structure with a combined injection/compression molding process, where the height error factor is related to the depth of the first structure and the depth of the air gap.

The 2 media A-DOE has very relaxed tolerances. Moreover, surface roughness is not an issue, since the difference of the refractive indices is relatively small. The main drawback remains the limited choice for the materials. The A-DOE with the interior air gap has the advantage of a wider choice of materials, while the fabrication tolerances are extremely stringent. Moreover, the Fresnel losses at the inclined interfaces are relatively large. The

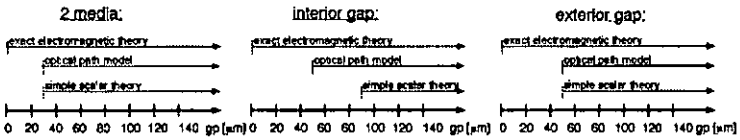

Figure 5.27: Graphical representation of the validity of the different models for the description of the concepts for A-DOEs.

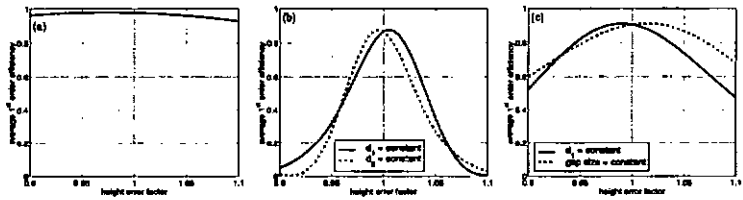

Figure 5.28: Fabrication tolerances for the three concepts for A-DOEs. (a) 2 media structure, (b) interior, and (c) exterior air gap.

A-DOE with the exterior air gap has clearly less critical fabrication tolerances and reduced Fresnel losses at the interfaces, compared to the interior air gap A-DOE.

5.4.4 Conclusions

We introduced different concepts for A-DOEs and showed the advantages and consequences for the structures with an interior air gap compared to the structures having an exterior air gap. We determined the limits of the simple scalar theory and the optical path model for the description of the different concepts. Up to relatively large grating periods the optical path model ($90\,\mu m$) or exact electromagnetic theory ($50\,\mu m$) has to be used for an accurate description of the A-DOEs because of the large depth of the structures. We determined the range of grating periods for which the different A-DOE concepts can be used, and we analyzed also the fabrication tolerances. The fabrication tolerances are most relaxed for the 2 media structure, more critical for the exterior air gap structure, and extremely critical for the A-DOE with the interior air gap.

5.5 Chapter summary

In this chapter we have presented diffractive and refractive optical microstructures which are related by their common property of being deep. A model has been developed to determine theoretically the 3-D surface profiles of optical reflow microstructures, fabricated by the melting resist technology. We used a finite element method where the border geometry of the microlens can be arbitrary. We analyzed the influence of gravity on optical properties of spherical microlenses and demonstrated the utility of this modelling method for the design of non-standard microlenses, e.g. for smart mask applications. We introduced focusing fan-out elements which combine fan-out and focusing function, resulting in a monolithic element with miniaturized dimensions. This type of elements has a high potential for applications in optical microsystems. We designed, fabricated, and characterized deep color separating 4-level gratings with small grating periods. We determined theoretically the range of grating periods for which these color separating gratings show the behaviour as expected from scalar theory when used for combining wavelengths to synthesize colors. We have presented different concepts for achromatized DOEs (A-DOEs), which are diffractive structures with high diffraction efficiency over a large spectral bandwidth in the visible region. We showed the advantages and consequences of an improved concept using two blazed gratings and an air gap. We determined the limits of different models for the description of these kind of structures, determined their range of use, and analyzed the fabrication tolerances.

Chapter 6

Specific applications of optical microstructures

In contrast to the more fundamental results related to optical microstructures presented in the previous chapters, we present in this chapter two concrete applications for diffractive and refractive optical microstructures. In Section 6.1 an incoherent micro-optical beamshaping device is presented for application in rangefinder distance measurement systems with extended measurement range. The optical microstructures used for this device were of diffractive and refractive nature. In Section 6.2 we present two different diffractive optical microstructures with potential for applications in diffractive optical security devices.

6.1 Beamshaping for high power diode–lasers

6.1.1 Introduction

High power, pulsed diode-lasers are used in rangefinder systems for distance measurements. For these rangefinders the achievable measurement range depends directly on available laser output power. The available laser output power per unit length is limited by the damage threshold of the material. Therefore, more output power results in a larger active region and the geometrical shape of the emitting surface is typically a line. Efficient collimation of such a partially coherent linearly extended light source with large divergence angles is a non-trivial problem and difficult to achieve with conventional optics. We designed, fabricated, and characterized a micro-optical device with two aligned, diffractive or refractive optical elements in combination with conventional optics.[27] The goal was to achieve a high coupling

efficiency of such a linear diode-laser into a multimode fiber, using a compact and low cost optical system that is suited for mass fabrication. The diode-laser was coupled into a multimode fiber to simplify the quantification of the performance. For a rangefinder application, the transformed light distribution is imaged onto the distant object. Leger and Goltsos [53] used a similar approach as described here to convert a mutually incoherent linear diode-laser array into a 2-dimensional source with maximum radiance and symmetrized shape and divergence. Their system was designed to optimize end pumping of solid-state lasers. In our work we used a partially coherent line source and an optical system designed for use in rangefinders.

6.1.2 Working principle

While the laser source is fully coherent perpendicular to the active region, the spatial coherence extends only to a fraction of the total length in the parallel direction. Therefore, a coherent beamshaping element, a so-called random phase plate, as for example designed by an iterative Fourier algorithm,[58, 50] is not an appropriate approach for the beamshaping problem which is addressed here. The special coherence properties of the source necessitate an incoherent beamshaping method.

The main characteristics of a linear diode-laser are the emitting wavelength λ, the lateral extensions of the active regions $d_\perp$ and $d_\parallel$, and the numerical apertures $NA_\perp = \sin(\theta_\perp)$ and $NA_\parallel = \sin(\theta_\parallel)$ perpendicular and parallel, respectively. $\theta_\perp$ and $\theta_\parallel$ are the corresponding divergence half angles. The employed diode-laser had a wavelength of $\lambda = 850\,nm$, lateral dimensions of $d_\perp = 1\,\mu m$ and $d_\parallel = 350\,\mu m$, and numerical apertures of $NA_\perp = 0.51$ and $NA_\parallel = 0.12$. The space bandwidth product (SBP) is defined as [34]

$$SBP = \frac{d}{2}\,NA \tag{6.1}$$

where d and NA are the lateral dimension and the numerical aperture, respectively. For a diffraction limited Gaussian beam the space bandwidth product is [98]

$$SBP = \lambda/\pi. \tag{6.2}$$

The SBP of the high power diode-laser is therefore nearly diffraction limited in the direction perpendicular to the emitting edge, and typically a factor of 50 larger than the diffraction limited case in the parallel direction. The main problem for the beamshaping of the linear edge emitting diode-laser lies in the fact, that with conventional optics the SBP in one direction stays constant at best. Only the ratio between the NA and d can be changed. The basic

principle of our beamshaping device is to symmetrize the lateral dimensions and the NA of the source such that $SBP_\perp = SBP_\parallel$ with $SBP_\perp \cdot SBP_\parallel = const.$ For that purpose, the line source is divided into three equal parts and redistributed on the fiber with the desired values for the NA and the lateral dimensions. Consequently, we increase the coupling efficiency into the fiber and correspondingly enlarge the range for rangefinder measurements, because of the increased intensity on the target. We described the linear diode-laser by an incoherent superposition of 75 independent Gaussian sources with beam waists corresponding to the measured divergence angles. The division of the source is achieved with the first micro-optical element. This has to be done before the various incoherent Gaussian beams begin to overlap in the direction parallel to the emitting edge. Otherwise an efficiency loss will occur which is approximately proportional to the overlap and therefore to the distance between the emitting source and the first diffractive element.

The concept of dividing and reassembling an incoherent source is not restricted to the special configuration presented here. Using this principle, it is possible to transform virtually any distribution of light into any other. The second element only has to be adjusted with respect to the shapes and directions of the various parts of the source created by the first element.

6.1.3 The optical setup

The complet optical setup is schematically displayed in Fig. 6.1. The fast and

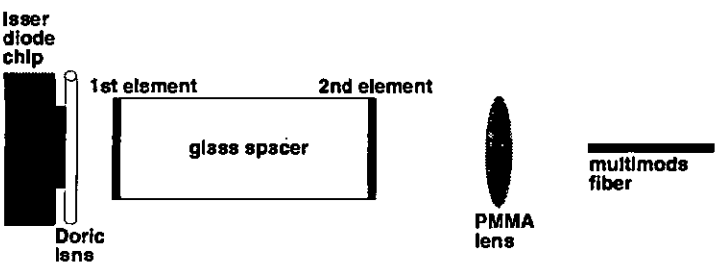

Figure 6.1: Schematic optical setup with the diode-laser chip (emitting surface: $1\,\mu m$ x $350\,\mu m$), the combined diffractive optical element, an additional Polymethyl-Methacrylate (PMMA) imaging lens, and the optical multimode fiber ($\phi = 100\,\mu m$, NA = 0.2).

slow NA of the laser diode were measured to be $NA_\perp = 0.51$ and $NA_\parallel = 0.12$, respectively. A gradient-index cylindrical lens (Doric Lenses Inc., Canada),

which had a specified effective numerical aperture of NA = 0.5 and a diameter of 60 μm, was mounted directly after the active region in order to collimate the fast axis. Since the tolerances for mounting the gradient–index lens are very tight, it was aligned manually by measuring the far field intensity distribution, and finally glued onto the laser chip. The theoretical NA after the Doric lens was $NA_{\perp} = 0.0083$. Subsequently, the beamshaping device follows, which is composed of two diffractive elements with a glass spacer in between. The first diffractive element, with a size of 370 μm x 370 μm, divides the line source into three equal parts along the parallel direction and directs the corresponding light emission into three different directions. The working principle is schematically shown in Fig. 6.2. In parts 1 and

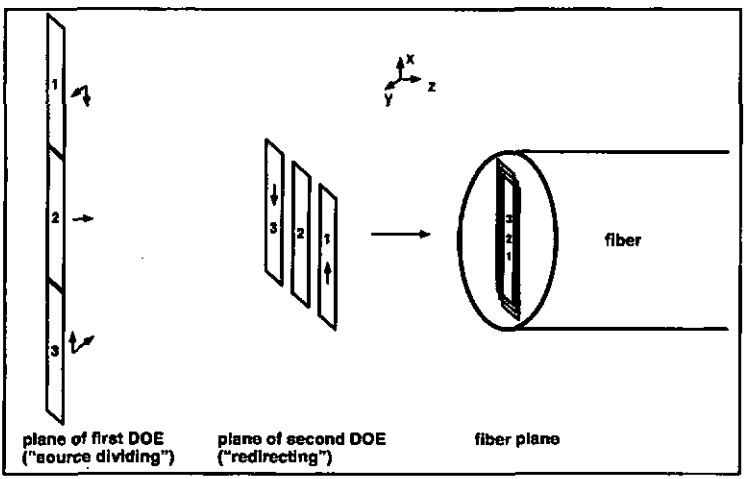

Figure 6.2: Schematic working principle of the beamshaping device (the Doric and the PMMA lens are omitted for clarity). The different parts of the source are denoted by the numbers 1, 2, and 3. The arrows mark the prism functions in the planes of the two DOEs.

3 of the first diffractive element there are three different optical functions implemented: a prism function perpendicular, a prism function parallel, and a focusing function parallel to the emitting edge of the diode-laser. The central part 2 has only the focusing function, which collimates the beam parallel to the active region. A typical measured intensity distribution in the plane of the second diffractive element is shown in Fig. 6.3. The second

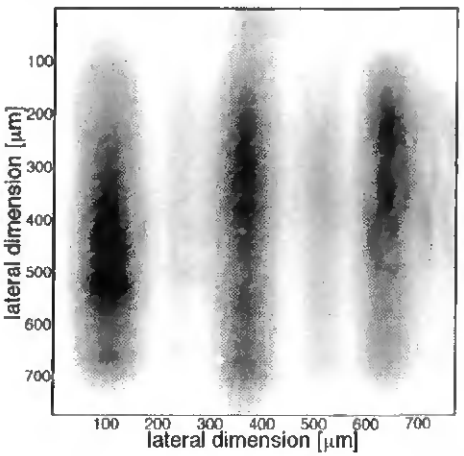

Figure 6.3: Typical measured 2 D intensity distribution in the plane of the second diffractive element with the three separated lobes ($NA_{\perp} = 0.066$, $NA_{\parallel} = 0.069$).

diffractive element, with a size of $800\mu m$ x $800\mu m$, redirects the parts 1 and 3 of the intensity distribution in the direction parallel to the emitting edge. The final conventional Polymethyl-Methacrylate (PMMA) lens after the second diffractive element has two functions. It creates a reduced image of the transformed source at the fiber plane, and at the same time serves to superpose the three parts of the source. The multimode fiber has a diameter of $100\mu m$ with a numerical aperture of NA = 0.2.

6.1.4 Results and discussion

The two diffractive elements were fabricated by direct laser writing [30, 29] in photoresist with the laser writer at CSEM in Zurich, Switzerland. Figures 6.4(a) and (b) show microscope pictures of the first and second element, respectively. Since the elements are quite small, a large number of elements can be written on one wafer in a single fabrication step. Subsequent replication and mounting procedure are also wafer compatible, so that parallel fabrication technology can be used until the dicing of the combined diffrac-

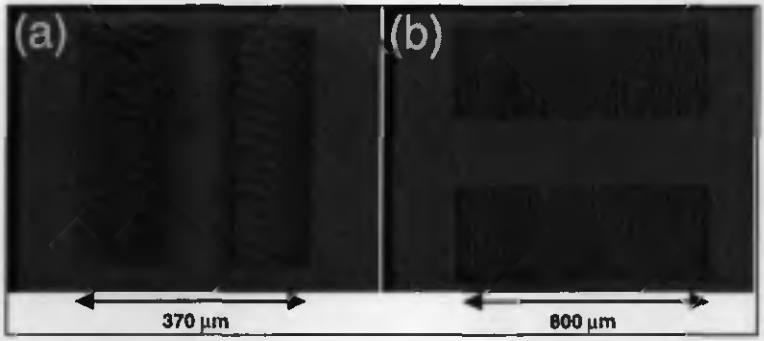

Figure 6.4: Microscope photographs of the two diffractive elements. (a) is the first element close to the diode laser, (b) shows the second element. The elements were fabricated by direct laser writing in photoresist.

Table 6.1: **Experimental efficiencies of the single, diffractive elements. Efficiencies are normalized with respect to transmitted intensity through unstructured substrate.**

part of element	measured efficiency
1^{st} element, left	70%
1^{st} element, center	84%
1^{st} element, right	68%
2^{nd} element, up	79%
2^{nd} element, center	98%
2^{nd} element, bottom	81%

tive elements. Therefore, the fabrication, alignment and mounting process is suited for mass fabrication at low cost.

The diffraction efficiency of the two diffractive elements were characterized before mounting, using focused light from a VCSEL with a wavelength of $850\,nm$. The measured efficiencies for the different sections of the two elements are summarized in Table 6.1. The first element had an averaged efficiency of 74%, the second element of 87%. The two diffractive elements and the borofloat glass spacer with a thickness of $600\,\mu m$ were then aligned and glued together with UV curable lens bond optical cement, using a Karl Suess maskaligner MA/BA6. The alignment marks were written by the laser writer at the same time as the diffractive structures. The alignment of the two diffractive elements with respect to each other was better than $5\,\mu m$.

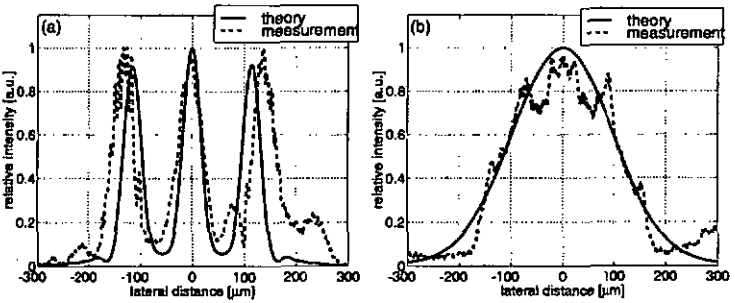

Figure 6.5: Calculated and measured intensity distributions in the plane of the second diffractive element: (a) cross section perpendicular to the slow axis of the diode-laser, (b) cross section parallel to the slow axis of the diode-laser.

The total thickness of the combined diffractive element after mounting was $3\,mm$.

For the theoretical optimization of the system design we used the commercially available raytrace program Code V^{TM}. The performance of the setup was then analyzed quantitatively with a wave propagation model,[98] using different propagation methods as described in Subsection 3.3.1. Diffraction at apertures is fully taken into acount, while Fresnel losses at the optical surfaces are not considered. For the comparison of theoretical and experimental intensity distributions we used the wave propagation model, where we modeled the linear diode-laser by an incoherent superposition of 75 independent Gaussian sources with beam waists corresponding to the measured divergence angles (Eqs. (6.1) and (6.2)). Calculated and measured intensity cross sections in the plane of the second diffractive element and in the fiber plane are shown in Figs. 6.5 and 6.6, respectively. The agreement between the theoretical and experimental intensity distributions is very satisfying. A possible cause for the observed small differences could be the non-uniformity of the emitted intensity at the active region of the diode-laser. This experimental non-uniformity can also be seen in Fig. 6.3.

For the collimating efficiency of the gradient-index lens, we measured a value of about 80%. With the wave propagation model we obtained a value of about 88%, taking into acount Fresnel losses. Concerning the theoretical value, a 4% loss originates from diffraction effects at the aperture; while another 8% are Fresnel losses. The overall efficiency of the beamshaping device is given by the ratio of the light power coupled into the fiber divided by

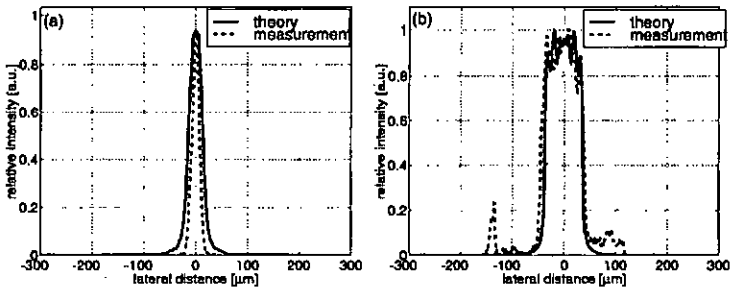

Figure 6.6: Calculated and measured intensity distributions in the plane of the fiber: (a) cross section perpendicular to the slow axis of the diode-laser, (b) cross section parallel to the slow axis of the diode-laser.

emitted laser power. For the overall efficiency we obtained experimentally 28%. The theoretical value is 80%, assuming ideal diffractive elements and no Fresnel losses. The difference between theoretical and experimental values has two main reasons. First, there are Fresnel losses which acount in total to about 14%. These losses can be eliminated by antireflective coatings on all optical surfaces. Second, the non-ideal diffractive elements result in an overall efficiency loss of about 27%. The diffractive elements, especially the first element with the smaller grating periods, can be replaced by refractive elements with increased efficiency fabricated by HEBS glass graytone technology. A comparison of different technologies for the fabrication of the two micro-optical elements is given in Subsection 6.1.5. As shown below, an efficiency increase of about 10% for the first element is realistic, so that we would expect about 50% overall efficiency for an optimized device. The reason for the theoretical losses are mainly twofold: coupling losses for the collimation of the fast angle by the gradient-index lens, which amount to about 4%, and overlap losses of about 5% which originate from the fact that one coherent source point hits two different parts of the first diffractive element. The second loss is limited by the minimum distance of the first micro-optical element from the diode-laser, about $100\,\mu m$, and is mainly determined by the gradient-index lens with the smallest available diameter which was $60\,\mu m$. The other 11% are due to diffraction effects at the apertures of the system. Table 6.2 summarizes the experimental efficiencies together with the estimated optimization potential.

Since the NA of the impinging light at the fiber plane is important for the coupling efficiency, we measured the NA for the fast and the slow axis

Table 6.2: **Experimental efficiencies and estimated optimization potential considering antireflective coatings and micro-optical elements fabricated by graytone technology. The efficiency and the optimization potential refer to the overall efficiency.**

position	experimental efficiency	optimization potential between subsequent positions
laser output	100%	n. a.
after GRIN lens	80%	5%
after 1st DOE	48%	8%
after 2nd DOE	38%	2%
fiber	28%	7%

at the fiber plane and calculated the corresponding values with the wave propagation model. We obtained for the slow axis an experimental value of NA = 0.12 compared to a theoretical value of NA = 0.16. For the fast axis we obtained experimentally NA = 0.09 and theoretically NA = 0.11. The experimental and theoretical values for the fast axis agree reasonably well while for the slow axis the experimental value is significantly smaller. A possible reason for the observed difference between the experimental and theoretical values for the slow axis could lie in the simplified description of the partially coherent diode-laser as an incoherent superposition of Gaussian sources within the wave propagation model.

6.1.5 Comparison of different fabrication technologies

Fabrication methods

Besides direct laser beam writing in photoresist, we also used two other technologies for the fabrication of the two micro-optical elements of the beamshaping device: binary mask photolithography in combination with reactive ion etching, resulting in 8-level fused silica elements, and High-Energy-Beam-Sensitive (HEBS) glass graytone lithography in photoresist, resulting in continuous surface relief structures. These fabrication methods are described in Chapter 2. We compare the performance of the different fabrication technologies with respect to the two micro-optical elements which were used for the beamshaping device. We discuss the different fabrication tolerances and sources of loss, as well as the diffractive/refractive behaviour of the elements.[79, 80]

Results and discussion

Both micro-optical elements were fabricated by the three technologies. The laser written elements are in photoresist and have a continuous diffractive surface relief profile with a depth of $2.8\,\mu m$ (Fig. 6.4). The HEBS glass graytone elements have a continuous refractive surface profile with a depth of $18\,\mu m$. The elements fabricated by graytone lithography in photoresist are shown in Figs. 6.7 and 6.8. The 8-level fused silica elements have a diffractive surface profile with a depth of $1.65\,\mu m$. As a consequence of the relatively small grating periods of the first element compared with the minimum feature size of $1.25\,\mu m$, the effective number of phase levels was partially smaller than 8. The first element fabricated by binary mask technology as 8-level element in fused silica is shown in Fig. 6.9. One can clearly see the three different

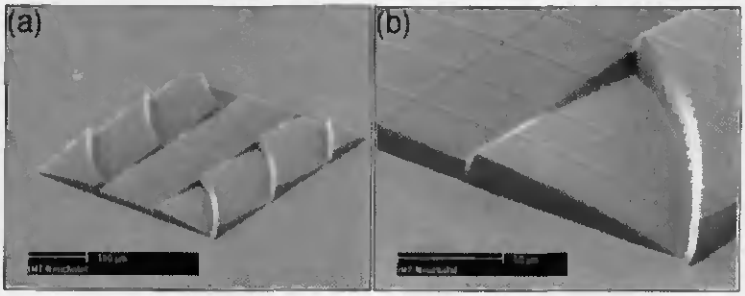

Figure 6.7: SEM image of the first element fabricated by HEBS glass graytone lithography in photoresist. (a) overview, (b) enlarged detail.

parts of each of the elements with the different optical functions implemented.

For the performance of the two diffractive elements in the beamshaping device two main characteristics are of importance: the accuracy of the deflection angles under which the light is deviated and the efficiency of the deflection into this direction. Therefore, we analyzed the efficiency and the deflection angles of the elements fabricated by the three technologies. Table 6.3 shows a comparison of the measured diffraction efficiencies which were achieved with the different technologies. The efficiencies were measured with the focused light from a VCSEL diode at $\lambda = 850\,nm$. The spot size (full width at $1/e^2$ intensity level) in the plane of the element was measured with a knife edge to be $50\,\mu m$. For the graytone elements the effective efficiency includes the losses at the non-ideal profile steps whereas the maximum efficiency is measured when the beam does not hit such a step. We found

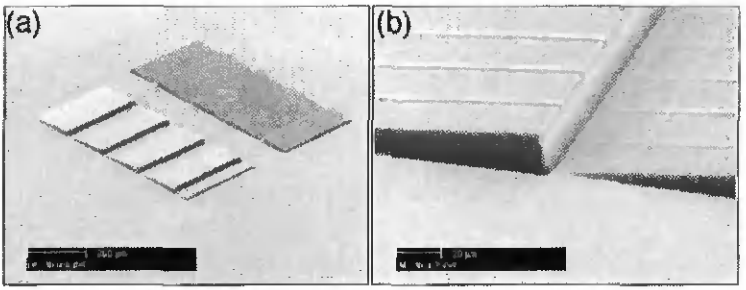

Figure 6.8: SEM image of the second element fabricated by HEBS glass graytone lithography in photoresist. (a) overview, (b) enlarged detail.

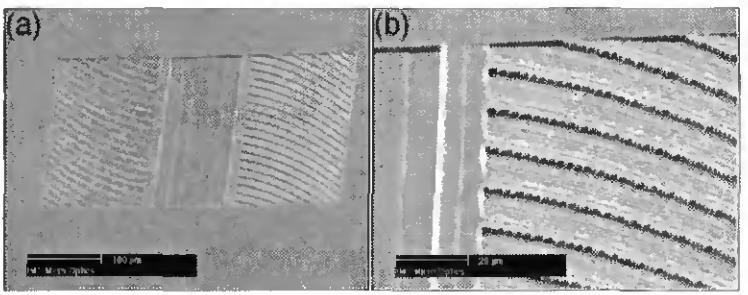

Figure 6.9: SEM image of the first element fabricated as multilevel structure (8 levels) in fused silica. (a) overview, (b) enlarged detail.

that the efficiencies of the second element achieved with the three different technologies were nearly equal, slightly above 80%. For the first element, which has steeper slopes and correspondingly smaller grating periods, the graytone element had a higher efficiency, while the laser written elements and the multilevel elements performed nearly equal. The sources of the loss for the different elements are quite different. For the multilevel elements the losses are mainly due to the approximation of the ideal profile by the multilevel structure and the alignment errors between the different lithographic steps. For the laser written elements, the main losses are caused by the finite width of the writing beam and the surface roughness. The main losses of the graytone elements are due to the surface roughness and the non ideal profile steps.

Table 6.3: **Measured diffraction efficiencies, normalized with respect to transmitted intensity through unstructured substrate.**

	1^{st} element left part	1^{st} element right part	2^{nd} element
efficiency multilevel	70%	70%	82%
efficiency laser writer	70%	68%	81%
efficiency graytone	78% (effective)	81% (effective)	78% (eff.)
	84% (maximum)	84% (maximum)	88% (max.)

Table 6.4: **Comparison between measured and designed deflection angles for the two diffractive elements.**

	1^{st} element deflection angle, vertical	2^{nd} element deflection angle
design value [degree]	4.01	3.38
multilevel [degree]	3.97	3.36
laser written [degree]	4.11	3.47
graytone [degree]	4.45	3.67

Table 6.4 shows a comparison of the measured and designed deflection angles of the two elements which were fabricated by the different technologies. The multilevel elements reproduced nearly exactly the designed deflection angles, the laser written elements showed slight deviations from the design values, while the differences were largest for the graytone elements. For the multilevel elements the directions are determined by the grating periods, which are intrinsically well defined. For the refractive graytone elements the directions are determined by the surface profile, which is more difficult to control.

6.1.6 Conclusions

We designed, fabricated and characterized a micro-optical beamshaping device, intended to optimize the coupling of a incoherent linear high power diode-laser into a multimode fiber. With a first prototype we achieved an overall efficiency of 28%, which corresponds well to the theoretical values obtained with a wave propagation model. Straightforward improvements, like antireflective coatings and the use of graytone elements, should lead to an efficiency of about 50%. The beamshaping device is compact and the fabrication is well suited for mass production at low cost. Used in a rangefinder measurement system, this micro-optical device will extend the measurement

range because of the symmetrized intensity distribution obtained on a distant target.

We compared three different technologies for the fabrication of the two micro-optical elements of the beamshaping device. With the graytone elements we achieved for the small grating periods the highest efficiency, while the deviations of the deflection angles from the designed values were largest. The multilevel elements reproduced best the designed deflection angles, but with moderate efficiency for small grating periods. The efficiency of the laser written structures were comparable to the multilevel elements, while the accuracy of the deflection angles was better than for the graytone elements, nearly as good as with the multilevel elements. Refractive type elements (graytone) yield better efficiency for large deflection angles, while diffractive elements (multilevel or laser written) give intrinsically accurate deflection angles.

6.2 Diffractive optical security devices

6.2.1 Introduction

Diffractive optical security devices are widespread nowadays and can be found on valuable documents like passports or banknotes. A good example is the Kinegram™, which can be found on the banknotes of Switzerland, Germany, and Austria. A photograph of a Kinegram™, taken from a 50 Swiss francs banknote, is shown in Fig. 6.10. Such diffractive optical security devices incorporate high resolution diffraction gratings which produce unique visual effects. In the following, we present diffractive optical microstructures with specially designed optical properties which can be exploited as optically variable devices for document security applications. Diffractive optical security devices have to fulfill special requirements in order to be useful. The diffractive structures need to be suf-

Figure 6.10: Diffractive optical security device, the Kinegram™, as on a 50 Swiss francs banknote.

ficiently thin, so that they add no additional thickness. A typical upper bound for the thickness is about $25\,\mu m$, including protective layers and adhesives. Additionally, for non-expert users it has to be easy to verify visually the security device. Machine readibility is often also a necessity, or at least desired for certain applications. Probably the most natural feature of this optical microstructures is the resilience against fraud. Gratings with continuously varying depth have been shown to be very resistant against standard holographic copy techniques, since these techniques lead to a loss of fidelity in profile form and depth.[87] In order to be competetive as a product on the market, these diffractive structures have to be fabricated by cheap mass production replication, like roll embossing.

6.2.2 Fabrication of the elements

In this section we present elements which consist of two superposed gratings with varying phase shift.[91, 92] Two different fabrication methods are applied. The basic concept is to synthesize more complicated grating structures by superposition of simple basis functions with varying phase shift β between them.

The first type of elements is a superposition of two sinusoidal gratings, where the amplitude and the period of the second grating was half as large as for the first one. For zero phase shift, they represent the first two Fourier coefficients of a blazed grating. In principal, arbitrary surface profiles can be synthesized by superposing a larger number of sinusoidal functions, corresponding to higher Fourier terms. The technical constraints for more than two exposures are however prohibitive. The sine-sine combination gratings were fabricated by holographic recording, as described in Section 2.3, with a single-frequency krypton-ion laser at $\lambda = 413\,nm$. The details of the holographic recording process are described in reference [93]. The grating period of the second basis grating was slightly detuned with respect to half of the grating period of the first grating. Therefore, the two basis functions were superposed with varying phase shift as a function of position on the sample, and consequently, the resulting surface profile was varying accordingly. Over a distance of $2.5\,mm$ the phase shift was $\beta = 2\pi$. The double exposure method with a slightly detuned grating period for one basis grating has several advantages. First, with one fabrication step a complete series of elements is obtained. Second, the series is continuous so that no information is missed like in the case of a discrete set of samples.

The second type of elements was a superposition of two rectangular gratings, where the second grating had again half the depth and half the period of the first one. The rect-rect combination gratings were fabricated as 4-level

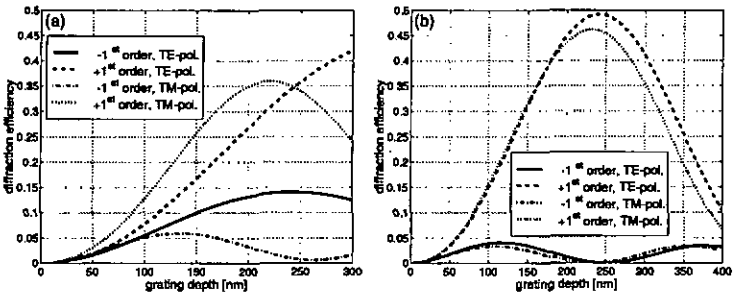

Figure 6.11: Efficiency of the $\pm 1^{st}$ reflected diffraction orders as a function of grating depth for the two types of combination gratings ($\beta = 0$). The grating material was Nickel (n = 1.8 + 3.3 i) against air with an illuminating wavelength of $\lambda = 632.8\,nm$: (a) sine-sine combination gratings, $\Lambda = 1\,\mu m$, (b) rect-rect combination gratings, $\Lambda = 7\,\mu m$.

surface relief gratings, as described in Subsection 2.1.1 and Section 2.5, where the second exposure step was executed with a maskaligner and a slightly rotated second mask. The rotation was controlled by using the alignment marks on the mask. Depending on the position on the substrate, the two rectangular gratings are superposed with a different phase shift, resulting in a moiré like pattern.

In order to determine the optimum grating depth for the combination gratings we calculated the theoretical efficiencies of the $\pm 1^{st}$ diffraction orders in reflection as a function of grating depth for the combined gratings with zero phase shift (Fig. 6.11). The efficiencies were calculated using exact electromagnetic diffraction theory (Subsection 3.2.1), with Nickel (n = 1.8 + 3.3i) as grating material, illuminated from air with a wavelength of $\lambda = 632.8\,nm$. The grating periods for the sine-sine and rect-rect combination gratings were $\Lambda = 1\,\mu m$ and $\Lambda = 7\,\mu m$, respectively. From the curves in Fig. 6.11 the assymmetry in the $\pm 1^{st}$ diffraction orders as a function of total grating depth can be extracted. The optimum choice of the grating depth is based on a maximum asymmetry between light diffracted in the $+1^{st}$ and -1^{st} order for both polarizations. The optimum theoretical value for the high frequency sine-sine grating is about $270\,nm$. However, we chose a smaller grating depth of about $145\,nm$, because it was experimentally difficult to maintain the sinusoidal surface profile of the basis functions while increasing the grating depth further. The optimum value of the rect-rect grating for a

maximum asymmetry is about $240\,nm$ whereas experimentally we achieved $270\,nm$.

6.2.3 Experimental and theoretical results

Sine–sine combination gratings

From the combination gratings recorded in photoresist, Nickel shims were fabricated by electroforming. AFM pictures of the surface profiles of the Nickel shims are shown in Figs. 6.12(a), (b), (c), and (d), for phase shifts of 0, $\pi/2$, π, and $3\pi/2$ between the basis functions, respectively. Using these

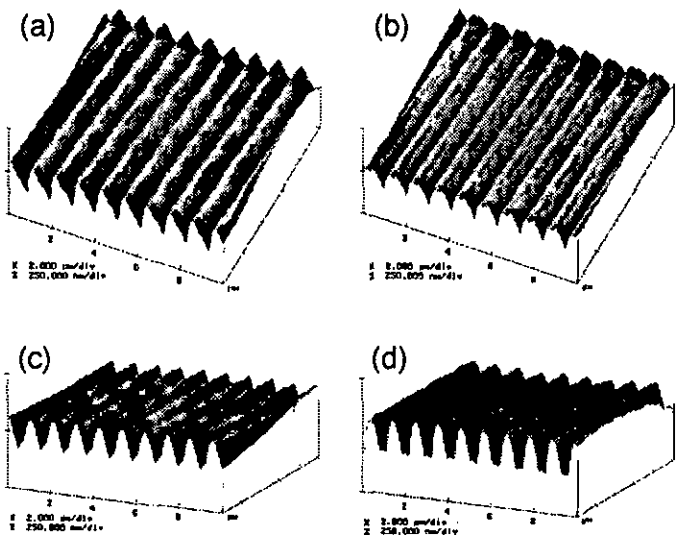

Figure 6.12: AFM pictures of the fabricated sine–sine combination gratings gratings with different phase shifts between the basis functions.(a) phase shift of 0, (b) phase shift of $\pi/2$, (c) phase shift of π, (d) phase shift of $3\pi/2$. The gratings were fabricated at OVD Kinegram Corp., Zug, Switzerland

measured surface profiles, we found for the depths of the two basis sine functions $112\,nm$ and $56\,nm$ for the low and high frequency grating, respectively. One can clearly see the left blazed and right blazed gratings in Figs. 6.12(a)

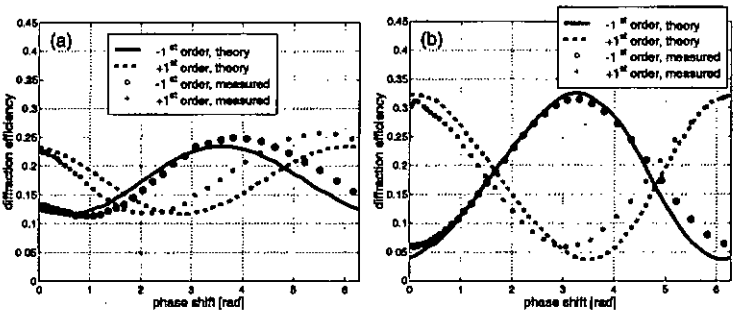

Figure 6.13: Calculated and measured diffraction efficiencies of the sine–sine combination gratings: (a) TE–polarization, (b) TM–polarization.

and (c), respectively, and the two symmetric surface profiles in Figs. 6.12(b) and (d). The Nickel gratings were characterized in reflection with slightly focused light from a He–Ne laser at $632.8\,nm$ under normal incidence. The spot size on the sample was about $50\,\mu m$ to assure that the surface profile of the grating did not vary significantly within the illuminated area. The calculated and measured diffraction efficiencies of the sine–sine combination gratings are shown in Figs. 6.13(a) and (b) for the polarizations TE and TM. In the calculations we used for the amplitudes of the high frequency grating $70\,nm$ determined by a best fit of the measured and calculated efficiencies. The agreement between the experimental and theoretical efficiencies is quite satisfactory. The small deviations can be explained by slight variations in the height of the grating structure. The desired asymmetry in the $\pm 1^{st}$ diffraction orders as a function of phase shift is clearly observed, more pronounced for the TM- than for the TE-polarization. The superposition of the two basis functions with the slightly different k-vectors which caused the surface profile and therefore the diffraction efficiency to vary on a mm-scale, revealed under ambient light illumination a visually interesting moiré like effect.

Comparing the two polarizations in Fig. 6.13, it is remarkable that the diffraction efficiencies for a phase shift of $\beta = \pi/2$ and $\beta = 3\pi/2$, which should be equal according to scalar diffraction theory, are equal for TM–polarization, but differ significantly for TE–polarization. In order to investigate this effect, we performed nearfield calculations for the sine–sine combination gratings for both polarizations. The time averaged intensities of the y–components of the electric, E_y, and magnetic field, H_y, are displayed in Figs. 6.14 and 6.15 for TE–polarization and TM–polarization, respectively.

The nearfield images of the time averaged intensity show that for TM–

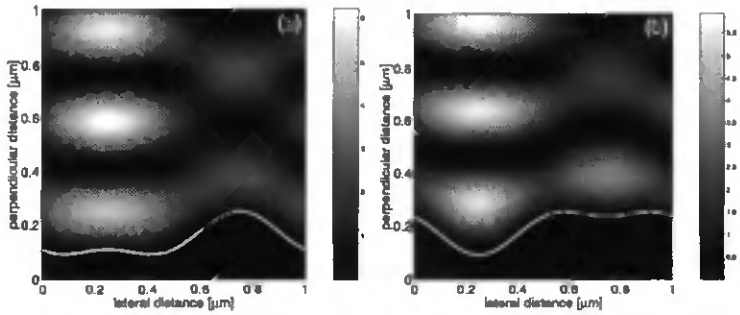

Figure 6.14: Time averaged intensity of the E_y field component for TE-polarization: (a) $\beta = \pi/2$, (b) $\beta = 3\pi/2$.

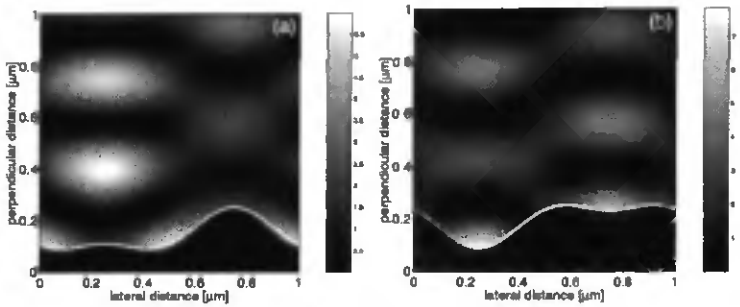

Figure 6.15: Time averaged intensity of the H_y field component for TM-polarization: (a) $\beta = \pi/2$. (b) $\beta = 3\pi/2$.

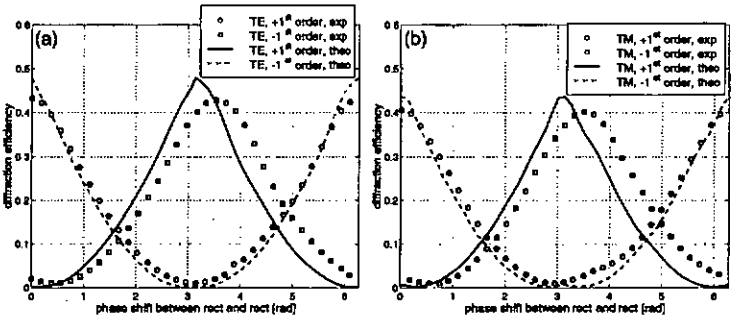

Figure 6.16: Calculated and measured diffraction efficiencies of the rect–rect combination gratings: (a) TE–polarization, (b) TM–polarization.

polarization the intensity maxima are in the local valleys of the surface profile for both phase shifts. For TE–polarization however, the intensity is strongly localized in the valley for a phase shift of $3\pi/2$, but concentrated in front of the small bumps for a phase shift of $\pi/2$. The larger asymmetry in the case of TE–polarization is consistent with the observed diffraction efficiencies (Fig. 6.13).

Rect–rect combination gratings

From the original fused silica rect–rect combination gratings, Nickel shims were produced by electroforming. These elements were characterized in reflection with a slightly focused light from a He–Ne laser at $632.8\,nm$ under normal incidence with a spot size on the sample of again about $50\,\mu m$. The total depth of the combination gratings was about $270\,nm$, as determined by profilometer measurements. The calculated and measured diffraction efficiencies of the rect–rect combination gratings are shown in Fig. 6.16 for the two polarizations TE and TM. Because of the larger grating period compared to the sine–sine combination gratings, a more scalar behaviour is observed with only slight differences between the two polarizations. Again, we found good agreement between the theoretical and measured diffraction efficiencies. For both polarizations a clearly varying asymmetry between the $\pm 1^{st}$ diffraction orders as a function of phase shift can be observed. The resulting moiré like effect can be exploited for diffractive optical security devices.

6.2.4 Conclusious

Two types of combination gratings, sine–sine and rect–rect, with continuously varying profile form have been designed, fabricated, and characterized. Good agreement has been found between the experimental and the theoretical diffraction efficiencies obtained from exact electromagnetic diffraction theory. Both types of combination gratings clearly show a varying asymmetry in the $\pm 1^{st}$ diffraction orders as a function of phase shift between the two basis functions. The two types of combination gratings are potentially useful for optical security devices because of the moiré pattern easily observed in the diffraction efficiency and the polarization properties.

Chapter 7

Summary and conclusions

In this thesis we have presented theoretical and experimental results related to refractive and diffractive optical microstructures.

We have addressed the fundamental problem of how to translate an ideal designed phase function of a DOE into a surface relief profile of a real element with given fabrication constraints. First, we considered the fabrication of a DOE by the multilevel approach, and analyzed the scalar-based method Direct Sampling (DS) for phase function encoding with exact electromagnetic diffraction theory. We found that quantized phase profiles obtained with scalar DS are, under given fabrication constraints, close to the optimum solutions, even for grating period to wavelength ratios (Λ_0/λ) as small as approximately 2 to 3.3. We fabricated and characterized 8-level DS encoded blazed gratings in fused silica and found good agreement between the experimental and the theoretical diffraction efficiencies obtained by exact electromagnetic diffraction theory. We also compared the influence of the encoding schemes DS and analytical quantization (AQ) on the quality of the focal spot. Secondly, we show how the influence of the finite width of the writing beam can be significantly reduced when continuous-relief DOEs are fabricated by direct laser writing. We implemented an IFT algorithm for the optimization of arbitrary 1-D and 2-D diffractive fan-outs which are compensated for the convolution with the writing beam. Subsequently, we fabricated and characterized test structures, and found that the efficiencies and the uniformities could be improved considerably by the compensation algorithm and demonstrated a very good agreement between the theoretical and experimental values for the efficiencies and uniformities.

We present results which are related to deep, optical microstructures. A method is introduced to calculate the 3-D surface profiles of refractive optical microstructures fabricated by the resist reflow technique. The border geometry of the structures can be arbitrary, and surface tension and grav-

ity are fully taken into account. We analyzed the influence of gravity on the optical properties of spherical microlenses and demonstrated the utility of this modelling method for the design of non-standard microlenses, e.g. for smart mask applications. Micro-optical elements are presented which combine the fan-out and focusing function, resulting in compact monolithic elements with miniaturized dimensions and with a high potential for applications in optical microsystems. We designed, fabricated, and characterized deep, color separating 4-level gratings with small grating periods. We also determined theoretically the grating period range for which these color separating gratings show the behaviour as expected from scalar theory when used for combining wavelengths to synthesize colors. We discussed the advantages and consequences of an improved concept for achromatized DOEs (A-DOEs), diffractive structures which show for a large spectral bandwidth in the visible region a nearly constant high efficiency. We determined the limits of different models, determined the range of use of the structures, and analyzed the fabrication tolerances.

We designed, fabricated and characterized a new incoherent diode-laser collimator for application in rangefinder systems with extended measurement range. With a first prototype we achieved an overall efficiency of 28%. The overall efficiency corresponds well with the calculated values which were obtained with a wave propagation model. Straightforward improvements like antireflective coatings and the use of graytone elements should lead to an efficiency of about 50%. The beamshaping device is quite compact and fabrication is suited for mass production at low cost. Additionally, we compared three different technologies for the fabrication of the two micro-optical elements of the beamshaping device. We found that with refractive type elements, better efficiencies can be achieved for large deflection angles, while with diffractive elements accurate deflection angles can be obtained more easily.

Theoretical and experimental results are presented for diffractive structures with continuously varying profile form for visual security applications. Two types of combination gratings, sine-sine and rect-rect, with continuously varying profile form have been designed, fabricated, and characterized. Good agreement has been found between the experimental and the theoretical diffraction efficiencies obtained by exact electromagnetic diffraction theory. Both types of combination gratings have clearly shown a varying asymmetry in the $\pm 1^{st}$ diffraction order as a function of phase shift between the two basis functions. The two types of combination gratings are potentially useful for optical security devices due to their assymmetry and polarization properties of the moiré pattern caused by the slowly varying surface profile form and therefore diffraction efficiency.

Acknowledgements

There were many people involved in the work presented in this thesis. I would like to thank

- Prof. René Dändliker for being my thesis adviser, who gave me the opportunity to work towards a Ph.D. in the Applied Optics Group in the fascinating field of Micro-Optics during the last four years. I very much appreciated his scientific competence in optics during many discussions and also his personality.
- Prof. Hans Peter Herzig for being the one who introduced me in the field of Micro-Optics, followed my thesis work most closely, and contributed the most to it. He was always available for discussions and an unexhaustible source of new ideas.
- Prof. Theo Tschudi (TU Darmstadt, Germany) for his function as member of the jury and for the time he invested into the review of the manuscript.
- Dr. Wayne Tompkin (OVD Kinegram Corp., Zug) as member of the jury, and for the interesting discussions we had in this four years. I would also like to thank him for the work he did in the projects within the Priority Program OPTIQUE II.
- the Priority Program OPTIQUE II for financial support.
- Dr. Peter Blattner who introduced me into the world of MATLAB™ and exact electromagnetic diffraction theory. He was always a valuable partner in discussions touching any field of optics.
- Dr. Urs Vokinger and Laurent Stauffer (Leica Geosystems AG, Heerbrugg) for the work and help within the beamshaper project.
- Dr. Markus Rossi (Heptagon, Zurich) and Thomas Ammer (CSEM, Zurich) for the laser direct writing of several diffractive structures.

- Irene Philipoussis for doing a lot of photolithography work, and for sharing the office from the first day on.
- Dr. Kenneth Weible for introducing me into mask data generation, the work in connection with the A-DOEs, and for many other times where he helped me.
- Dr. E.-B. Kley (Friedrich Schiller Universität Jena) and his co-workers for the electron beam writing of the HEBS glass mask.
- René Staub (OVD Kinegram Corp. AG, Zug) for the work in the common projects within the OPTIQUE II program.
- Philippe Nussbaum for the reactive ion etching of the color fan-out structures and the transfer of the refractive microlenses.
- The CSEM in Neuchâtel for the batch fabrication of the MPW DOEs.
- Christian Ossmann and Dr. Rheinhard Völkel (Karl Suess KG, Neuchâtel) for the discussions and help within the "smart mask" work.
- Roman Merz for the work which he did during his semester project for the profile modeling of reflow microstructures.
- Omar Manzardo for sharing the office since the first days and for the many interesting discussions we had at IMT and "au chauffage".
- Dr. Peter Kipfer for the "Schweine- und Rinderbraten" events which he organized, and the "chauffage" and "Garbo" nights we spent.
- Kharim Haroud for his help during the measurements in the fiber lab and for many discussions.
- Dr. Toralf Scharf for interesting discussions about liquid crystals and polarization.
- Dr. Manuel Teijido, Dr. Christoph Berger, Marcel Groccia and Frédéric Gonté for their competent IT support.
- Yves-Alain Peter, Dr. Manuel Bouvier, Antonello Nesci, Olivier Ripoll, and Dr. Martin Salt for all the lunches "à la cité" which we spent together.
- all other former and existing members of the Applied Optics Group for the nice and stimulating atmosphere in the group.

- I would also like to express many thanks to the secretaries Mary-Claude Gauteault, Senta Jacot, Sandrine Piffaretti, Caroline Huguenin, and Joëlle Banjac, who always did an excellent job.
- My girl friend Susi for her patience and understanding during the often turbulent times.
- My parents for everything they have done for me during my years of study.

Bibliography

[1] Y. Arieli, S. Ozeri, and N. Eisenberg. Design of a diffractive optical element for wide spectral bandwidth. *Opt. Lett.*, 23:823–824, 1998.

[2] J. Bauer, G. Drescher, and M. Illig. Surface tension, adhesion and wetting of materials for photolithographic process. *J. Vac. Sci Technol. B*, 14:2485–2492, 1996.

[3] M.J. Beesely and J.G. Castledine. The use of photoresist as a holographic medium. *Appl. Opt.*, 9:2720–2724, 1970.

[4] G.P. Behrmann and J.N. Mait. *Micro-Optics: Elements, Systems, and Applications*, chapter Hybrid (Refractive/Diffractive) Optics, pages 259–292. H.P. Herzig, ed. (Taylor & Francis), 1997.

[5] Ch. Berger, N. Collings, R. Völkel, M. T. Gale, and T. Hessler. A microlens–array–based optical neural network application. *Pure Appl. Opt.*, 6:683–689, 1997.

[6] P. Blattner, H.P. Herzig, K.J. Weible, J.M. Teijido, H.J. Heimbeck, E. Langenbach, and J. Rogers. Diffractive optics for compact space communication terminals. *J. Mod. Opt.*, 43:1473–1484, 1996.

[7] M. Born and E. Wolf. *Principles of Optics*. Cambridge University Press, Cambridge, USA, 1977.

[8] K.H. Brenner. Method for designing arbitrary two–dimensional continuous phase elements. *Opt. Lett.*, 25:31–33, 2000.

[9] A. Budo. *Theoretische Mechanik*. VEB Deutscher Verlag der Wissenschaften, Berlin, Germany, 1987.

[10] D.A. Buralli and G.M. Morris. Optical performance of holographic kinoforms. *Appl. Opt.*, 28:976–983, 1989.

[11] C.B. Burckhardt. Diffraction of a plane wave at a sinusoidally stratified dielectric grating. *J. Opt. Soc. Am.*, 56:1502–1509, 1966.

[12] J. Chandezon, D. Maystre, and G. Raoult. A new theoretical method for diffraction gratings and its numerical application. *J. Optics (Paris)*, 11:235–241, 1980.

[13] D. Daly, R.F. Stevens, M.C. Hutley, and N. Davies. The manufacture of microlens by melting photoresist. *J. Meas. Sci. Technol.*, 1:759–766, 1990.

[14] H. Dammann. Color separation gratings. *Appl. Opt.*, 17:2273–2279, 1978.

[15] H. Dammann. Spectral characteristics of stepped-phase gratings. *Optik*, 53:409ff, 1979.

[16] W. Däschner, C. Wu, and S.H. Lee. General aspheric refractive micro-optics fabricated by optical lithography using a high energy beam sensitive glass gray-level mask. *J. Vac. Sci. Technol. B*, 14:135–138, 1996.

[17] S. M. Ebstein. Nearly index-matched optics for aspherical, diffractive, and achromatic-phase diffractive elements. *Opt. Lett.*, 21:1454–1456, 1996.

[18] P. Ehbets. *Efficient phase gratings for beam splitting and beam shaping.* PhD thesis, Université de Neuchâtel, 1995.

[19] P. Ehbets, H.P. Herzig, P. Nussbaum, P. Blattner, and R. Dändliker. Interferometric fabrication of modulated submicrometer gratings in photoresist. *Appl. Opt.*, 34:2540–2547, 1995.

[20] M.T. Eismann, A.M.Tai, and J.N. Cederquist. Iterative design of a holographic beamformer. *Appl. Opt.*, 28:2641–2650, 1989.

[21] M. Eisner. *Untersuchungen zum Einsatz eines Refraktiven Mikrolinsen-Blenden Arrays in einem Konfokalen Auflichtmikroskop.* PhD thesis, Friedrich-Alexander-Universität Erlangen-Nürnberg, Germany, 1999.

[22] M. Eisner, N. Lindlein, and J. Schwider. Confocal microscopy with a refractive microlens-pinhole array. *Opt. Lett.*, 23:748–749, 1998.

[23] L. Erdmann. *Experimentelle und theoretische Untersuchungen zur Herstellung und Charakterisierung refraktiver Mikrolinsen*. PhD thesis, Universität Jena, Germany, 1998.

[24] M.W. Farn, R.W. Knowlden, M.B. Stern, and W.B. Veldkamp. *Conference on Binary Optics*, chapter Color separation gratings. H.J. Cole and W.C. Pittman, eds., 3227, NASA Conference Publication, 1993.

[25] M. Ferstl, R. Steingrüber, W. Fürst, S. Krüger, and S. Teiwes. High-efficiency computer-generated holograms. *Proc. SPIE*, 3879:147–156, 1999.

[26] J.R. Fienup. Iterative method applied to image reconstruction and to computer-generated holograms. *Opt. Eng.*, 19:297–305, 1980.

[27] B. Gächter, A. Schilling, L. Stauffer, and U. Vokinger. Optischer Entfernungsmesser; European patent application 00108836.8, 2000. Patent pending.

[28] M.T. Gale. *Micro-Optics: Elements, Systems, and Applications*, chapter Replication, pages 153–177. H.P. Herzig, ed. (Taylor & Francis), 1997.

[29] M.T. Gale, Th. Hessler, R.E. Kunz, and H. Teichmann. Fabrication of continuous-relief micro-optics: progress in laser writing and replication technology. *OSA Technical Digest Series*, 5:335ff, 1996.

[30] M.T. Gale and M. Rossi. *Diffractive Optics for Industrial and Commercial Applications*, chapter 4 Continuous-relief diffractive lenses and microlens arrays. J. Turunen and F. Wyrowsky, eds. (Akademie Verlag Berlin), 1997.

[31] J.D. Gaskill. *Linear Systems, Fourier Transforms, and Optics*. Wiley, New York, USA, 1978.

[32] R.W. Gerchberg and W.O. Saxton. A practical algorithm for the determination of phase from image and diffraction plane pictures. *Optik*, 35:227–246, 1972.

[33] Ch. Gimkiewicz, D. Hagedorn, J. Jahns, E.-B. Kley, and F. Thoma. Fabrication of microprisms for planar optical interconnections by use of analog gray-scale lithography with high-energy-beam-sensitive glass. *Appl. Opt.*, 38:2986–2990, 1999.

[34] J.W. Goodmann. *Introduction to Fourier Optics*. McGraw-Hill International, 1996.

[35] B. Gu and G. Yang. On the phase retrieval problem in optical and electronic microscopy. *Acta Opt. Sin.*, 1:517–522, 1981.

[36] H.P. Herzig. *Micro-Optics: Elements, Systems, and Applications*, chapter Design of Diffractive and Refractive Micro-Optics, pages 1–30. H.P. Herzig, ed. (Taylor & Francis), 1997.

[37] H.P. Herzig, Ph. Nussbaum, A.Schilling, S. Trant, I. Philipoussis, C. Ossmann, R. Völkel, M. Rossi, and H. Schift. Different concepts for the fabrication of hybrid (refractive/diffractive) elements. *OSA Technical Digest Series*, 10:279–281, 1998.

[38] H.P. Herzig, D. Prongué, and R. Dändliker. Design and fabrication of highly efficient fan-out elements. *Jap. J. Appl. Phys.*, 29:1307–1309, 1990.

[39] T. Hessler. *Continuous-Relief Diffractive Optical Elements: Design, Fabrication and Applications*. PhD thesis, Université de Neuchâtel, Switzerland, 1997.

[40] T. Hessler, M. Rossi, R.E. Kunz, and M.T. Gale. Analysis and optimization of fabrication of continuous-relief diffractive optical elements. *Appl. Opt.*, 37:4069–4079, 1998.

[41] R. Hutchins, H. Yang, J.E. Morris, and M.R. Feldman. Comparison of encoding methods for computer-generated diffractive optical elements. *Appl. Opt.*, 36:2313–2318, 1997.

[42] M.C. Hutley. The manufacture and testing of microlens arrays. *Proc. SPIE*, 1319:492–493, 1990.

[43] F.G. Kaspar. Diffraction by thick, periodically stratified gratings with complex dielectric constant. *J. Opt . Soc. Am.*, 63:37–45, 1973.

[44] G. Kirchhoff. Zur Theorie der Lichtstrahlen. *Weidemann Ann.*, 18:663ff. 1883.

[45] A.G. Kirk and T.J. Hall. Design of binary computer generated holograms by simulated annealing: coding density and reconstruction error. *Opt. Comm.*, 94:491–496, 1992.

[46] S. Kirkpatrick. Optimization by simulated annealing: Quantitative studies. *J. Stat. Phys.*, 34:975–986, 1984.

[47] S. Kirkpatrick, C.D. Gelatt, and M.P. Vecchi Jr. Optimization by simulated annealing. *Science*, 220:671–680, 1983.

[48] E.-B. Kley and W. Dorl. Einsatz von Elektronenstrahllithographie zur Herstellung mikrooptischer Bauelemente. *VDI Ber. Ver. Dtsch.Ing.*, 960:531–541, 1992.

[49] K. Knop. Rigorous diffraction theory for transmission phase gratings with deep rectangular grooves. *J. Opt. Soc. Am.*, 68:1206–1210, 1978.

[50] C. Kopp, L. Ravel, and P. Meyrueis. Efficient beamshaper homogenizer design combining diffractive optical elements, microlens array and random phase plate. *J. Opt. A: Pure Appl. Opt.*, 1:398–403, 1999.

[51] M. Kuittinen and H.P. Herzig. Encoding of efficient diffractive microlenses. *Opt. Lett.*, 20:2156–2158, 1995.

[52] P. Lalanne and G.M. Morris. Highly improved convergence of the coupled–wave method for TM–polarization. *J. Opt. Soc. Am. A*, 13:779–784, 1996.

[53] J. R. Leger and W. C. Goltsos. Geometrical transformation of linear diode–laser arrays for longitudinal pumping of solid state lasers. *IEEE J. Quantum Electron.*, 28:1088–1100, 1992.

[54] J.R. Leger, M.L. Scott, P. Bundmann, and M.P. Griswold. Computer Generated Holography II. S.H. Lee, ed. In *Proc. Soc. Photo-Opt. Instrum. Eng.*, page 82ff, 1988.

[55] U. Levy, N. Cohen, and D. Mendlovic. Analytic approach for optimal quantization of diffractive optical elements. *Appl. Opt.*, 38:5527–5532, 1999.

[56] L. Li. Use of Fourier series in the analysis of discontinuous periodic structures. *J. Opt. Soc. Am. A*, 13:1870–1876, 1996.

[57] M. Lo, B. Dong, B. Gu, and P. Meyrueis. Non–periodic diffractive phase element for wavelength–division (de)multiplexing. *Opt. Comm.*, 173:217–221, 2000.

[58] J.N. Mait. Understanding diffractive optic design in the scalar domain. *J. Opt. Soc. Am. A*, 12:2145–2158, 1995.

[59] L. Mandel and E. Wolf. *Optical Coherence and Quantum Optics*. Cambridge University Press, Cambridge, 1995.

[60] D. Maystre and R. Petit. Diffraction par un réseau lamellaire infinement conducteur. *Opt. Comm.*, 28:413–428, 1971.

[61] M.G. Moharam and T.K. Gaylord. Rigorous coupled-wave analysis of planar-grating diffraction. *J. Opt. Soc. Am.*, 71:811–818, 1981.

[62] M.G. Moharam, D.A. Pommet, E.B. Grann, and T.K. Gaylord. Stable implementation of the rigorous-coupled-wave analysis for surface relief gratings: enhanced transmittance matrix approach. *J. Opt. Soc. Am. A*, 12:1077–1086, 1995.

[63] E. Noponen, J. Turunen, and A. Vasara. Electromagnetic theory and design of diffractive-lens arrays. *J. Opt. Soc. Am. A*, 10:434–443, 1993.

[64] Ph. Nusshaum, R. Völkel, H.P. Herzig, and R. Dändliker. Micro-optics for sensor applications. *Proc. SPIE*, 2783:55–63, 1996.

[65] Ph. Nussbaum, R. Völkel, H.P. Herzig, M. Eisner, and S. Haselbeck. Design, fabrication and testing of microlens arrays for sensors and microsystems. *Pure Appl. Opt.*, 6:617–636, 1997.

[66] Ph. Nussbaum, K.J. Weible, M. Rossi, and H.P. Herzig. Potential of dry etching for the fabrication of fused silica micro-optical elements. *Proc. SPIE*, 3879:63–70, 1999.

[67] S.T. Peng, T. Tamir, and H.L. Bertoni. Theory of periodic dielectric waveguides. *IEEE Trans. Microwave Theory Tech.*, 23:123–133, 1975.

[68] R. Petit. *Electromagnetic Theory of Gratings*, chapter 3, pages 85–88. Springer-Verlag, Berlin, 1980.

[69] D. A. Pommet, M.G. Moharam, and E.B. Grann. Limits of scalar diffraction theory for diffractive phase elements. *J. Opt. Soc. Am. A*, 11:1827–1834, 1994.

[70] D. Prongué, H.P. Herzig, R. Dändliker, and M.T. Gale. Optimized kinoform structures for highly efficient fan-out elements. *Appl. Opt.*, 31:5706–5711, 1992.

[71] M. Rossi. *Phase-matched optical Fresnel elements*. PhD thesis, Université de Neuchâtel, Switzerland, 1995.

[72] M. Rossi, C.G. Blough, D.H. Raguin, E.K. Popov, and D. Maystre. Diffraction efficiency of high-NA continuous-relief diffractive lenses. *OSA Tech. Digest Series*, 5:233–236, 1996.

[73] A. Schilling, P. Blattner, and H.P. Herzig. Direct sampling for diffractive microlens encoding from a rigorous point of view. *Pure Appl. Opt.*, 7:565–574, 1998.

[74] A. Schilling and H.P. Herzig. Phase function encoding of diffractive structures. *Appl. Opt.*, 39:5273–5279, 2000.

[75] A. Schilling, R. Merz, Ch. Ossmann, and H.P. Herzig. Surface profiles of reflow microlenses under the influence of surface tension and gravity. *Tech. Digest of the 7th Microoptics Conference*, 7:132–135, 1999.

[76] A. Schilling, R. Merz, Ch. Ossmann, and H.P. Herzig. Surface profiles of reflow microlenses under the influence of surface tension and gravity. *Opt. Eng.*, 39:2171–2176, 2000.

[77] A. Schilling, Ph. Nussbaum, Ch. Ossmann, S. Traut, M. Rossi, H. Schift, and H.P. Herzig. Miniaturized, focusing fan-out elements: Design, fabrication, and characterization. *Proc. SPIE*, 3490:386–388, 1998.

[78] A. Schilling, Ph. Nussbaum, Ch. Ossmann, S. Traut, M. Rossi, H. Schift, and H.P. Herzig. Miniaturized, focusing fan-out elements: Design, fabrication, and characterization. *J. Opt. A, Pure Appl. Opt.*, 1:244–248, 1999.

[79] A. Schilling, Ph. Nussbaum, I. Philipoussis, H.P. Herzig, L. Stauffer, M. Rossi, and E.-B. Kley. Micro-optical elements with arbitrary surfaces. *Technical Digest of Diffractive Optics and Micro-Optics 2000*, pages 234–236, 2000.

[80] A. Schilling, Ph. Nussbaum, I. Philipoussis, H.P. Herzig, L. Stauffer, M. Rossi, and E.-B. Kley. Fabrication technologies for micro-optical elements with arbitrary surfaces. *Proc. SPIE*, 4179:65–72, 2000.

[81] A. Schilling, K.J. Weible, and H.P. Herzig. Diffractive structures with high, wavelength independent efficiency. *EOS Topical Meetings Digest Series*, 22:16–17, 1999.

[82] C.V. Shank and R.V. Schmidt. Optical technique for producing 0.1 μm periodic surface structures. *Appl. Phys. Lett.*, 23:154–155, 1973.

[83] J.T. Sheridan, J. Schwider, N. Streibl, S. Haselbeck, M. Eisner, M. Heissmeier, and O. Falkenstörfer. Modelling and measurement of melted microlens shapes. *Optik*, 97:174–180, 1994.

[84] N.K. Sheridon. Production of blazed holograms. *Appl. Phys. Lett*, 12:316–318, 1968.

[85] W. Singer, H.P. Herzig, M. Knittinen, E. Piper, and J. Wangler. Diffractive beamshaping elements at the fabrication limit. *Opt. Eng.*, 35:2779–2787, 1996.

[86] A. Sommerfeld. Die Greensche Funktion der Schwingungsgleichung. *Jahresber. Deut. Math. Ver.*, 21:309ff, 1912.

[87] R. Staub, W.R. Tompkin, and A. Schilling. Gratings of constantly varying depth for visual security devices. *Opt. Eng.*, 38:89–98, 1999.

[88] M.B. Stern. *Micro-Optics: Elements, Systems, and Applications*, chapter Binary Optics Fabrication, pages 53–85. H.P. Herzig, ed. (Taylor & Francis), 1997.

[89] G.J. Swanson. Binary optics technology: The theory and design of multi-level diffractive optical elements; Lab. Tech. Rep. 854, DTIC \#AD-213404. Technical report, MIT Lincoln Laboratory, Lexington, Mass., 1989.

[90] G.J. Swanson. Binary optics technology: theoretical limits on the diffraction efficiency of multilevel diffractive optical elements; Lab. Tech. Rep. 914. Technical report, MIT Lincoln Laboratory, Lexington, Mass., 1991.

[91] W. Tompkin, R. Staub, A. Schilling, and H.P. Herzig. Metallic gratings with locally varying profile. *EOS Topical Meetings Digest Series*, 22:72–73, 1999.

[92] W. Tompkin, R. Staub, Ch. Weitenedor, A. Schilling, and H.P. Herzig. High-frequency gratings with locally varying profile depth for visual security applications. *EOS Topical Meetings Digest Series*, 25:72–73, 2000.

[93] W.R. Tompkin, R. Staub, A. Schilling, and H.P. Herzig. Diffraction from metallic gratings with locally varying profile forms. *Opt. Lett.*, 24:71–73, 1999.

[94] W.T. Tsang and S. Wang. Simultaneous exposure and development technique for making gratings on positive photoresist. *Appl. Phys. Lett.*, 24:196–199, 1974.

[95] J. Turunen. *Micro-Optics: Elements, Systems, and Applications*, chapter Diffraction Theory of Microrelief Gratings, pages 31–52. H.P. Herzig, ed. (Taylor & Francis), 1997.

[96] The MathWorks Inc. USA. MATLAB™ version 5.2, 1998.

[97] W.B. Veldkamp and G.J. Swanson. Developments in fabrication of binary optical elements. *Proc. SPIE*, 437:54ff, 1983.

[98] U. Vokinger. *Propagation, Modification and Analysis of Partial Coherent Light Fields*. PhD thesis, Université de Neuchâtel, Switzerland, 1999.

[99] R. Völkel, H.P. Herzig, Ph. Nussbaum, , and R. Dändliker. Microlens array imaging system for photolithography. *Opt. Eng.*, 35:3323–3330, 1996.

[100] R. Völkel, H.P. Herzig, Ph. Nussbaum, P. Blattner, R. Dändliker, and E. Cullmann andW.B. Hugle. Microlens lithography and smart masks. *Microelectronic Eng.*, 35:513–516, 1997.

[101] M.R. Wang, G.J. Sonek, R.T. Chen, and T. Jannson. Large fan-out optical interconnects using thick holographic gratings and substrate wave propagation. *Appl. Opt.*, 31:236–249, 1992.

[102] K.J. Weible, A. Schilling, H.P. Herzig, and D. Lobb. Achromitization of the diffraction efficiency of diffractive optical elements. *Proc. SPIE*, 3749:378–379, 1999.

[103] W.H. Welch, J.E. Morris, and M.R. Feldmann. Iterative discrete on-axis encoding of radially symmetric computer-generated holograms. *J. Opt. Soc. Am. A*, 10:1729–1738, 1993.

[104] C. Wu. Method of making high energy beam sensitive glass; U.S. patent 5,078,771, 7 January 1992.

[105] F. Wyrowski and O. Bryngdahl. Iterative Fourier-transform algorithm applied to computer holography. *J. Opt. Soc. Am. A*, 5:1058–1065, 1988.

[106] G. Yang and B. Gu. On the amplitude-phase retrieval problem in the optical system. *Acta Phys. Sin.*, 30:410–413, 1981.

[107] P. Yeh, A. Yariv, and C. Hong. Electromagnetic propagation in periodic stratified media. I General theory. *J. Opt. Soc. Am.*, 67:423–438, 1977.

Abstracts of publications

Publication I

Direct sampling for diffractive microlens encoding from a rigorous point of view

A. Schilling, P. Blattner, and H.P. Herzig

Rigorous diffraction theory is applied to analyze the Direct Sampling (DS) encoding method, which is based on scalar diffraction theory. For given fabrication constraints and constant sampling width of the lens function, the quantized phase profiles obtained with scalar DS are close to the optimum solutions, even for grating period to wavelength ratios (Λ_b/λ) as small as about 3. For smaller ratios, the phase profiles obtained by DS can be improved by up to 25%, using a straightforward rigorous steepest gradient optimization. Applied to cylindrical lenses with NA = 0.5 and 0.63, coding with DS and with rigorous improved DS give quite similar results for the total diffraction efficiency.

Publication II

Miniaturized, Focusing Fan-out Elements: Design, Fabrication and Characterization

A. Schilling, Ph. Nussbaum, Ch. Ossmann, S. Traut, M. Rossi, H. Schift, H.P. Herzig

We present miniaturized, focusing fan-out elements. The new micro-optical elements were fabricated by different technologies: double-sided injection moulding in polycarbonate, double-sided photolithography with subsequent transfer in quartz, and direct laser writing in photoresist. The fan-out elements were characterized by measuring their efficiency and uniformity,

the surface profiles of the microlenses were measured with a Twyman–Green interferometer. The overall performance of the combined, hybrid elements is demonstrated with intensity distributions recorded in the focal planes.

Publication III

Diffraction from metallic gratings with locally varying profile forms

W.R. Tompkin, R. Staub, A. Schilling, H.P. Herzig

Measurements of the diffraction characteristics of one-dimensional surface-relief gratings of locally varying profile are compared to rigorous diffraction theory. The studied gratings result from the superposition of two linear sinusoidal gratings of uniform depth where the relative phase between the two gratings varies with position. If the relative phase varies slowly, then the resulting surface profile can exhibit a relatively large-period variation in profile form. The resulting periodic variation in diffraction efficiency yields a moiré pattern, having interesting asymmetry and polarization properties, which alters as the viewing conditions are changed; the gratings can be exploited by diffractive optically variable devices for document security.

Publication IV

Gratings of constantly varying depth for visual security devices

R. Staub, W.R. Tompkin, A. Schilling

The diffraction characteristics of sinusoidal gratings of locally varying profile depth are studied in order to assess the value of these surface-relief profiles as optically variable devices (OVDs) for securing documents.The diffractive characteristics of these gratings are shown to depend very sensitively on the profile form and depth. OVDs with visual effects have been developed which exploit this sensitive dependence; the security of these OVDs is inherent to the diffractive structures in so far as the exact reconstruction of the original profile is required for the realization of the visual effects. Sinusoidal gratings of locally varying profile depth are very resilient against copying by standard holographic techniques since these techniques are shown to lead to a loss of fidelity in profile form or depth.

Publication V

Surface profiles of reflow microlenses under the influence of surface tension and gravity

A. Schilling, R. Merz, Ch. Ossmann, and H.P. Herzig

We present a finite element method to calculate 3-D surface profiles of refractive microlenses fabricated by melting resist technology (reflow technique). The geometry of the microlenses can be arbitrary. Surface tension and gravity are taken into acount. Gravity can have an advantageous influence on the profile form, so that smaller focal spots can be achieved. A simple scaling law is given to estimate the influence of gravity on the profile form for given microlens parameters. We compared various theoretical and measured surface profiles of microlenses fabricated by melting resist technology and found good agreement. Finally, the usefulness of this method for the design of refractive microstructures for smart masks is shown.

Publication VI

Phase function encoding of diffractive structures

A. Schilling and H.P. Herzig

We analyzed the Direct Sampling (DS) method for diffractive lens encoding using exact electromagnetic diffraction theory. In addition to previously published work [A. Schilling, P. Blattner, H.P. Herzig, Pure Appl. Opt., 7, 565 (1998)] we present new results for TM-polarization. We found that the validity of the scalar-based DS method is even more extended for TM than TE-polarization. Additionally, we fabricated and characterized DS encoded blazed gratings and found good agreement between the experimental and theoretical diffraction efficiencies. We analyzed quantitatively the influence of the encoding schemes DS and Analytic Quantization (AQ) on the quality of the focal spot. Herefor, we investigated the focal spot sizes (FWHM) and the Strehl ratios of the DS and AQ encoded, cylindrical lenses.

Publication VII

Efficient beamshaping of linear, high–power diode–lasers using micro–optics

A. Schilling, H.P. Herzig, L. Stauffer, U. Vokinger, and M. Rossi

We designed, fabricated and characterized a micro-optical beamshaping device, intended to optimize the coupling of a incoherent, linear, high power diode-laser into a multimode fiber. The device uses two aligned diffractive optical elements (DOEs) in combination with conventional optics. With a first prototype we achieved an overall efficiency of 28%. Straightforward improvements, like antireflective coatings and the use of graytone elements, should lead to an efficiency of about 50%. The device is compact and the fabrication is suited for mass production at low cost. Used in a rangefinder measurement system, this micro-optical device will extend the measurement range. In addition to the direct laser writing technique, which was used for the fabrication of the DOEs of the prototype, we used two other technologies for the fabrication of the micro-optical elements and compared the performance. The technologies were: Multiple projection photolithography in combination with reactive ion etching (RIE) in fused silica, and high-energy-beam-sensitive (HEBS) glass graytone lithography in photoresist. We found that refractive type elements (graytone) yield better efficiency for large deflection angles, while diffractive elements (multilevel or laser written) give intrinsically accurate deflection angles.